Active Stabilization of Mechanical Quadrupole Vibrations in a Linear Collider Test Facility

Dissertation
zur Erlangung des Doktorgrades
des Fachbereichs Physik
der Universität Hamburg

Vorgelegt von
Christoph Montag
aus Paderborn

Hamburg 1996

Gutachter der Dissertation:	Dr. habil. J. Rossbach Prof. Dr. P. Schmüser
Gutachter der Disputation:	Dr. habil. J. Rossbach Prof. Dr.-Ing. Dr. h. c. G. A. Voss
Datum der Disputation:	3.2.1997
Sprecher des Fachbereichs Physik und Vorsitzender des Promotionsausschusses:	Prof. Dr. B. Kramer

Abstract

To achieve high luminosities of approximately $10^{34}\,\mathrm{cm}^{-2}\mathrm{sec}^{-1}$, future linear colliders require very low emittance beams focused to spot sizes of about 100 nm rms horizontally and about 10 nm rms vertically at the interaction point. To keep the beams in collision, high mechanical stability of the accelerator components, especially the focusing magnets, is necessary. In the case of the S-band Linear Collider SBLC, quadrupole position jitter tolerances can be estimated at 85 nm rms vertically and 380 nm horizontally.

While slowly varying misalignments can be compensated using beam-based correction schemes, the compensation of fast beam jitter requires a different approach.

Ground motion measurements at DESY are presented and discussed. Fast vertical quadrupole motion amplitudes are likely to exceed the tolerances in the frequency regime where the beam based correction systems are ineffective. Therefore, an inexpensive active stabilization system has been developed. It consists of a geophone mounted on top of each quadrupole and a piezo actuator to counteract the measured motion. This system is capable of suppressing quadrupole jitter in the frequency band 2 to 30 Hz by up to -14 dB, resulting in an rms quadrupole motion of approximately 25 nm for frequencies above 2 Hz even in noisy environments where the corresponding ground motion rms value is about 100 nm.

To investigate the effect of active stabilization on beam motion two ground motion simulation algorithms based on different models have been developed. Both algorithms can be adapted to any measured ground motion spectra and coherence.

As a specific application, ground motion data taken at DESY have been used to simulate beam motion at the end of the SBLC main linac. Using active stabilization, the rms beam jitter is reduced by a factor of up to 2.8, thus keeping the luminosity degradation below 1 %.

Übersicht

Um eine hohe Luminosität von etwa $10^{34}\,\mathrm{cm}^{-2}\mathrm{sec}^{-1}$ zu erreichen, ist es bei zukünftigen Linear Collidern notwendig, Strahlen extrem kleiner Emittanz am Wechselwirkungspunkt auf Abmessungen von etwa 100 nm horizontal und etwa 10 nm vertikal zu fokussieren. Um die Strahlen in Kollision zu halten, ist eine hohe mechanische Stabilität der Beschleunigerkomponenten, insbesondere der Fokussiermagnete, erforderlich. Im Fall des S-Band Linear Colliders SBLC können die Aufstelltoleranzen der Quadrupole zu 85 nm vertikal und 380 nm horizontal abgeschätzt werden. Während langsam veränderliche Fehlaufstellungen mit Hilfe strahlbasierter Korrekturschemata kompensiert werden können, erfordert die Kompensation schneller Strahlschwingungen einen anderen Ansatz.
Messungen der Bodenbewegung bei DESY werden vorgestellt und diskutiert. Die zu erwartenden vertikalen Quadrupolbewegungen werden vermutlich die geforderten Toleranzen in einem Frequenzbereich überschreiten, in dem strahlbasierte Korrektursysteme ineffizient sind. Aus diesem Grunde wurde ein preiswertes aktives Stabilisierungssystem entwickelt. Dieses besteht aus je einem Geophon, welches auf jeden Magneten montiert ist, und einem Piezo-Stellelement, um der gemessenen Bewegung entgegenzuwirken. Dieses System ist in der Lage, Vibrationen der Quadrupol-Magnete im Frequenzband von 2 bis 30 Hz um bis zu $-14\,\mathrm{dB}$ zu unterdrücken, was einem rms-Wert von etwa 25 nm bei 2 Hz selbst in einer unruhigen Umgebung mit einer entsprechenden Bodenbewegungsamplitude von ungefähr 100 nm entspricht.
Um den Effekt der aktiven Stabilisierung auf die Strahlbewegung zu untersuchen, wurden zwei Algorithmen zur Simulation der Bodenbewegung entwickelt, die auf verschiedenen Modellen beruhen. Beide Algorithmen können an beliebige gemessene Spektren und Kohärenzeigenschaften der Bodenbewegung angepaßt werden.
Als eine spezifische Anwendung wurden die bei DESY gemessenen Bodenbewegungsdaten benutzt, um die Strahlbewegung am Ende des SBLC Hauptlinacs zu simulieren. Der rms-Wert der Strahlbewegung wird durch aktive Stabilisierung um einen Faktor bis zu 2.8 reduziert, wodurch der Luminositätsverlust kleiner als 1 % gehalten werden kann.

Contents

1 Introduction **1**

2 Ground motion measurements **8**
2.1 Instrumentation 14
2.2 Results of ground motion measurements 17

3 Support concept **30**

4 Vibration sensors **35**

5 Design of the active stabilization system **42**

6 Experimental results on active stabilization **48**

7 Ground motion simulation models **52**
7.1 The filter-based model 52
7.2 The FFT-based model 54

8 Beam dynamics under the influence of ground motion **60**
8.1 The lattice 60
8.2 Simulation results 61

9 Conclusion **70**

Acknowledgements **71**

A The Shannon theorem **72**

B Description of linear systems in the frequency domain **73**
B.1 The Laplace transformation 73
B.2 The $\mathcal{Z}$ transformation 74

C Feedback systems **76**

D Stability of feedback loops **77**

E Digital filters **80**

F Magnet optics effect of a tilted quadrupole **84**

References **85**

1 Introduction

In the last several decades, electron accelerators have become powerful instruments for the investigation of the subatomic world. In the early years electron beams were accelerated in synchrotrons, extracted and guided onto external fixed targets to investigate the structure of the atomic nuclei in the target material. Later colliding beams in storage rings invented in 1960 by B. Touschek et. al. became state-of-the-art technology in particle physics. The aim of particle physics is to find the basic constituents of matter which have turned out to have rest masses much higher than those of the beam particles, therefore the beam energy E of these machines has increased from 250 MeV at ADA (Annello di Accumulatione) [Ber 61] to nearly 100 GeV at LEP 200 (Large Electron Positron) [Kei 81, Sch 86], the most powerful e^+e^- storage ring ever built. The highest beam energy so far achieved for protons is approximately 1 TeV at the TEVATRON at Fermilab, but this will be exceeded in the next decade at the Large Hadron Collider LHC currently being built in the LEP tunnel at CERN. At the same time the circumference of these machines has grown from a few meters to 27 km.
While the maximum energy of hadron machines is limited by the achievable strength of the magnetic fields used to bend the beam, the energy of e^+e^- storage rings is limited by a different effect. Due to the continuous transverse acceleration by dipole magnets defining the closed orbit of a circular machine, beam particles emit a characteristic electromagnetic radiation, the so-called synchrotron radiation.
The power loss ΔP due to synchrotron radiation of a charged particle following a curved trajectory of radius ρ is given by (MKSA-units) [Jac 75]:

$$\Delta P = \frac{e^2 c}{6\pi\epsilon_0} \cdot \frac{1}{(m_0 c^2)^4} \cdot \frac{E^4}{\rho^2}. \tag{1.1}$$

Here e and m_0 are the charge and the rest mass of the particle, respectively, while c denotes the velocity of light. $\epsilon_0 = 8.8542 \cdot 10^{-12}\,\mathrm{F\,m^{-1}}$ is the electric field constant. Due to the m_0^{-4} dependence of the power loss by synchrotron radiation the loss is significant mainly for light particles, namely electrons or positrons, while for protons or heavy ions it can be neglected in most cases. The particles travel at a velocity very close to c along a trajectory determined by the magnetic fields which guide and focus the beam. In a typical circular accelerator, the design orbit consists of straight sections and bends with constant bending radius ρ. Therefore the total pathlength per revolution over which the particle emits synchrotron radiation is $2\pi\rho$, while the corresponding time during which the particle follows a curved trajectory is $2\pi\rho/c$. Hence the energy loss per turn of a beam consisting of N identical particles circulating in an accelerator with constant bending radius ρ can be calculated as

$$\Delta E = N \cdot \frac{2\pi\rho}{c} \cdot \Delta P. \tag{1.2}$$

This energy loss has to be compensated by the rf-system. Therefore one has two different options to increase the beam energy of an e^+e^- collider beyond 100 GeV:
Firstly a more powerful rf-system could be installed, providing higher accelerating fields. Though this is a technically feasible possible solution it turns out to be economically unreasonable due to the E^4 dependence of the beam power loss.
The other alternative is a totally different approach which avoids power loss by synchrotron radiation – the so-called linear collider.
In contrast to the existing e^+e^- storage rings, a linear collider basically consists of two high

energy linear accelerators (linacs) providing high energy electron and positron beams travelling in opposite directions which interact with each other in the detector. Of course, the beams in such a machine are no longer recirculating; therefore the beam energy has to be provided during a single pass of the beam through the accelerator.
High energy physics laboratories all over the world are considering different approaches for the design of such a linear collider. The main difference between the various designs is the chosen rf-frequency which ranges from 1.3 GHz (L-band) at TESLA, a superconducting linear collider designed by an international collaboration coordinated at DESY, to 30 GHz for CLIC (CERN). Between these two extremes the normal-conducting machines SBLC (3 GHz, S-band), NLC and JLC (both 11.4 GHz, X-band) are being considered at DESY, SLAC and KEK, respectively. Since this thesis is addressed mainly to the S-band Linear Collider SBLC, this machine is described in more detail here.
The electron beam is generated in an electron gun where 2 μsec pulses of electron current are emitted from a cathode, longitudinally bunched and accelerated to 3.15 GeV in a pre-accelerator.
In order to decrease the emittance of this beam to the small value required by the linear collider, the beam is injected into a damping ring where its transverse phase space volume is reduced due to synchrotron radiation effects. To further decrease the length of the bunches leaving the damping ring, a bunch compressor, which provides different non-isochronous trajectories for particles of different energies, is inserted into the beam-line between the damping ring and the main linac. In this way, the length of a bunch with a systematic longitudinal energy profile can be shortened.
The positron beam has to be created in a different manner. The spent electron beam will be captured after the interaction point and sent through a long wiggler in order to produce high energy intense synchrotron radiation photons. These are directed onto a target to produce electron-positron pairs, while the electrons will be deflected into a beam dump. The produced positrons will be transported to a damping ring and experience the same procedure as the electrons.
In order to inject the beam into the main linac on axis a feedforward system, consisting of a high resolution beam position monitor and a fast kicker magnet, is foreseen. The position of each bunch is measured at the entrance of the bunch compressor, and this signal is used to correct the orbit of the same bunch after the bunch compressor. This is possible because the particles follow a curved trajectory inside the bunch compressor, as shown schematically in figure 1.1.
The main linac consists of constant-gradient travelling wave accelerating structures operated at 3 GHz (the so-called S-band) and quadrupole magnets which focus the beam. Additional space is foreseen for diagnostics devices, correction dipoles and other equipment which is necessary for the operation of the machine. Assuming a filling factor of 90 % and a loaded gradient of 17.3 MeV, i. e. the accelerating gradient when the accelerating structures are loaded by the beam, the length of a 250 GeV machine would be 16 km.
After acceleration, the high energy beam is transported through the final focus system, a system essentially consisting of quadrupole and sextupole magnets which focus the beams at the interaction point (IP). To preserve head-on collisions a beam based feedback system consisting of a beam position monitor and a kicker to correct the orbit is foreseen. Figure 1.1 shows a schematic view of the S-band Linear Collider SBLC.
The luminosity of such a machine can be expressed as

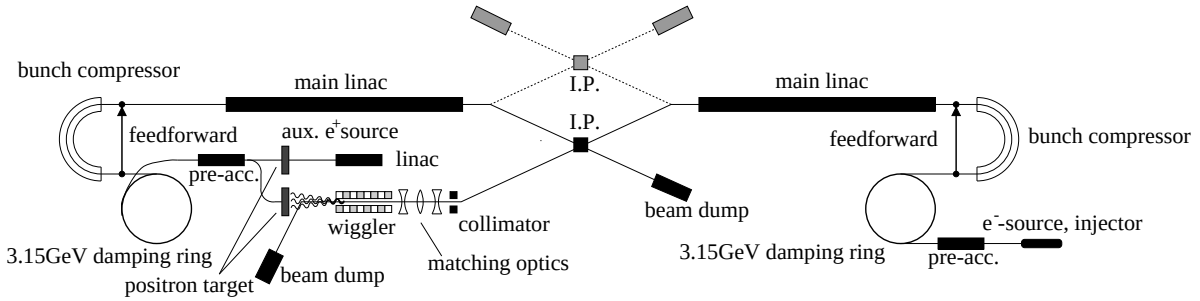

Figure 1.1: Schematic view of the S-band Linear Collider SBLC.

$$\mathcal{L}_0 = \frac{1}{4\pi}\frac{f_{\rm rep} n_{\rm b} N^2}{\sigma_x \sigma_y}, \tag{1.3}$$

with $f_{\rm rep}$, N and $n_{\rm b}$ being the repetition rate of the accelerator, i. e. the number of pulses per second, the number of particles per bunch and the number of bunches per pulse, respectively. σ_x and σ_y are the horizontal and vertical rms beam size at the interaction point. To achieve a luminosity $\mathcal{L}_0$ of approximately $10^{34}\,\mathrm{cm}^{-2}\mathrm{sec}^{-1}$ all linear collider schemes currently under study require very low emittance beams focused to extremely small spot sizes of some 10 nm vertically and some 100 nm horizontally. For example, the S-band Linear Collider SBLC with $f_{\rm rep} = 50\,\mathrm{Hz}$, $n_{\rm b} = 333$ and $N = 1.1 \cdot 10^{10}$ is being designed for a beam size of 335 nm horizontally and 16 nm vertically. These tiny beam dimensions require very low normalized beam emittances of $\gamma \cdot \epsilon_x = 5 \cdot 10^{-6}$ m horizontally and $\gamma \cdot \epsilon_y = 0.25 \cdot 10^{-6}$ m vertically (SBLC). To avoid luminosity loss due to beam jitter at the interaction point (e. g. caused by mechanical quadrupole vibrations) beam jitter amplitudes should be sufficiently smaller than the rms beam sizes.
The quadrupole vibration tolerances in the main linac can be derived as follows. Assuming a FODO lattice with the average β-function $\overline{\beta}$ scaling with the beam energy, i. e. with the relativistic γ-factor, as

$$\overline{\beta}(s) = \left(\frac{\gamma(s)}{\gamma_{\rm end}}\right)^n \overline{\beta}_{\rm end}, \tag{1.4}$$

with s denoting the longitudinal coordinate, the beam displacement $\Delta y_{\rm end}$ at the end of the linac caused by a single misaligned quadrupole with displacement δy and focal length f can be calculated as [Cou 58]

$$\Delta y_{\rm end} = \sqrt{\frac{\gamma}{\gamma_{\rm end}}}\sqrt{\beta_{\rm end}\beta}\sin(\Phi_{\rm end} - \Phi)\frac{\delta y}{f}. \tag{1.5}$$

Here Φ and β are the phase of the betatron oscillation and the β-function at the location of the misaligned quadrupole, respectively. The factor $\gamma/\gamma_{\rm end}$ reflects the fact that the transverse phase space of the beam shrinks as the beam is accelerated. Though this is not a real damping process in the common sense this effect is often referred to as adiabatic damping. This is the reason that the quantity preserved under acceleration is the so-called normalized emittance $\gamma \cdot \epsilon$ rather than the geometrical emittance. The rms beam displacement resulting from uncorrelated alignment errors of all N_q quadrupoles with rms displacement σ_q can accordingly be computed

as

$$\sigma_y^2 = \sum_{N_q} \frac{\gamma}{\gamma_{\text{end}}} \overline{\beta}\,\overline{\beta}_{\text{end}} \cdot \frac{1}{2}\frac{\sigma_q^2}{f^2}. \tag{1.6}$$

Here the factor $\gamma/\gamma_{\text{end}}$ results from adiabatic shrinking, while the factor $1/2$ accounts for the randomness of betatron phases.
Using the abbreviation $\xi = \gamma/\gamma_{\text{end}}$ and replacing the sum by an integral yields, together with eqn. (1.4),

$$\sigma_y^2 = \sigma_q^2\,\overline{\beta}_{\text{end}}^2 \int \frac{1}{f^2}\xi^{n+1}\,\frac{\mathrm{d}s}{L}, \tag{1.7}$$

with $2/L$ being the average "line density" of quadrupoles in a FODO cell of length L, consisting of two quadrupoles.
Under the assumptions of a constant acceleration and a small injection energy, i. e. $\gamma(0) \ll \gamma_{\text{end}}$, we have

$$\begin{aligned} \mathrm{d}s &= \frac{\gamma_{\text{end}}}{\mathrm{d}\gamma/\mathrm{d}s}\,\mathrm{d}\xi \\ &= \frac{\gamma_{\text{end}}}{\gamma_{\text{end}}/L_{\text{tot}}}\,\mathrm{d}\xi \\ &= L_{\text{tot}}\,\mathrm{d}\xi. \end{aligned} \tag{1.8}$$

Here L_{tot} denotes the total length of the linac.
With $1/f = (4/L)\sin(\mu/2)$ and $\overline{\beta} = (\gamma/\gamma_{\text{end}})^n\overline{\beta}_{\text{end}} = L/\sin\mu$ we get under the assumption of a constant phase advance μ per FODO cell

$$\begin{aligned} \sigma_y^2 &= \frac{4\sigma_q^2 L_{\text{tot}}}{\overline{\beta}_{\text{end}}\sin\mu\,\cos^2\frac{\mu}{2}} \int_{\xi_{\min}}^1 \xi^{1-2n}\,\mathrm{d}\xi \\ &\approx \frac{4\sigma_q^2 L_{\text{tot}}}{\overline{\beta}_{\text{end}}\sin\mu\,\cos^2\frac{\mu}{2}} \cdot \frac{1}{2-2n} \end{aligned} \tag{1.9}$$

as long as $\xi_{\min} \ll 1$ and $n < 0.8$.
The average length of a FODO cell can be calculated from the density function of FODO cells, $\rho(\gamma) = 1/L$, as

$$\begin{aligned} \langle L_{\text{FODO}} \rangle &= \frac{\int \rho(\gamma) L\,\mathrm{d}\gamma}{\int \rho(\gamma)\,\mathrm{d}\gamma} \\ &= \frac{\int \mathrm{d}\gamma}{\int \frac{\mathrm{d}\gamma}{\xi^n \overline{\beta}_{\text{end}}\sin\mu}} \\ &\approx (1-n)\overline{\beta}_{\text{end}}\sin\mu, \end{aligned} \tag{1.10}$$

so that the total number of quadrupoles is given by

$$\begin{aligned} N_q &= \frac{2L_{\text{tot}}}{\langle L_{\text{FODO}} \rangle} \\ &= \frac{2L_{\text{tot}}}{(1-n)\overline{\beta}_{\text{tot}}\sin\mu}. \end{aligned} \tag{1.11}$$

Thus the rms beam jitter at the end of the main linac is [Ros 93]

$$\sigma_y^2 = \frac{\sigma_q^2 N_q}{\cos^2 \frac{\mu}{2}}. \tag{1.12}$$

The resulting luminosity of two Gaussian beams with rms beam size $\sigma_{\rm beam}$ colliding with an rms offset σ_y from the ideal trajectory is given by

$$\mathcal{L} = \mathcal{L}_0 \cdot \exp\left(-2\frac{\sigma_y^2}{4\sigma_{\rm beam}^2}\right). \tag{1.13}$$

Allowing for a luminosity degradation of 3% due to beam separation at the IP the tolerable rms quadrupole misalignment can be estimated as [Rau 91, Ros 93]

$$\begin{aligned}
\sigma_{\rm q} &= \sqrt{\frac{\sigma_y^2}{N_q}} \cos\frac{\mu}{2} \\
&= 0.25\sqrt{\frac{\sigma_{\rm beam}^2}{N_q}} \cos\frac{\mu}{2} \\
&= 0.25 \cdot \sqrt{\frac{\epsilon_{\rm end} \cdot \overline{\beta}_{\rm end}}{N_{\rm q}}} \cdot \cos\frac{\mu}{2} \\
&= 0.25 \cdot \overline{\beta}_{\rm end} \cdot \sqrt{\frac{\epsilon_{\rm end} \cdot (1-n) \cdot \sin\mu}{2 \cdot L_{\rm tot}}} \cdot \cos\frac{\mu}{2},
\end{aligned} \tag{1.14}$$

where $\epsilon_{\rm end}$ is the geometric emittance at the end of the linac.
Using the parameters given in table 1.1 the tolerance level for vertical oscillations is found to be 85 nm for the 500 GeV and 43 nm for the 1 TeV S-band Linear Collider SBLC design [Hol 93], while in the horizontal plane these numbers relax to 380 nm and 430 nm, respectively. In the final focus system these tolerances are tighter by a factor of about 5 to 10 but cannot be expressed by eqn. (1.14) [Oid 89, Nap 94].

Ground motion measurements (fig. 1.2) at DESY [Shi 95] indicate that these vertical vibra-

	SBLC	
E [GeV]	500	1000
$\overline{\beta}_{\rm v,end}$ [m]	165	233
$\overline{\beta}_{\rm h,end}$ [m]	165	233
$\gamma \cdot \epsilon_{\rm v,end}$ [m · rad]	$2.5 \cdot 10^{-7}$	$0.5 \cdot 10^{-7}$
$\gamma \cdot \epsilon_{\rm h,end}$ [m · rad]	$5 \cdot 10^{-6}$	$5 \cdot 10^{-6}$
k	0.5	0.5
μ	$\pi/2$	$\pi/2\sqrt{2}$
$2 \cdot L$ [km]	29.4	29.4

Table 1.1: Parameters of the S-band Linear Collider SBLC relevant for the estimation of quadrupole jitter tolerances.

tion tolerances are exceeded in an active accelerator environment at frequencies higher than

those that can be compensated using beam-based feedback systems. Therefore one needs to implement either direct vibration measurement and compensation techniques, or it is necessary to guarantee a more quiet environment than that present at DESY and at many other active accelerators. Due to the large number of quadrupoles in the main linac the cost of each system should not exceed a limit of about DM 15000, while much more effort can be spent in the final focus system with its much smaller number of quadrupoles. With this goal an inexpensive ac-

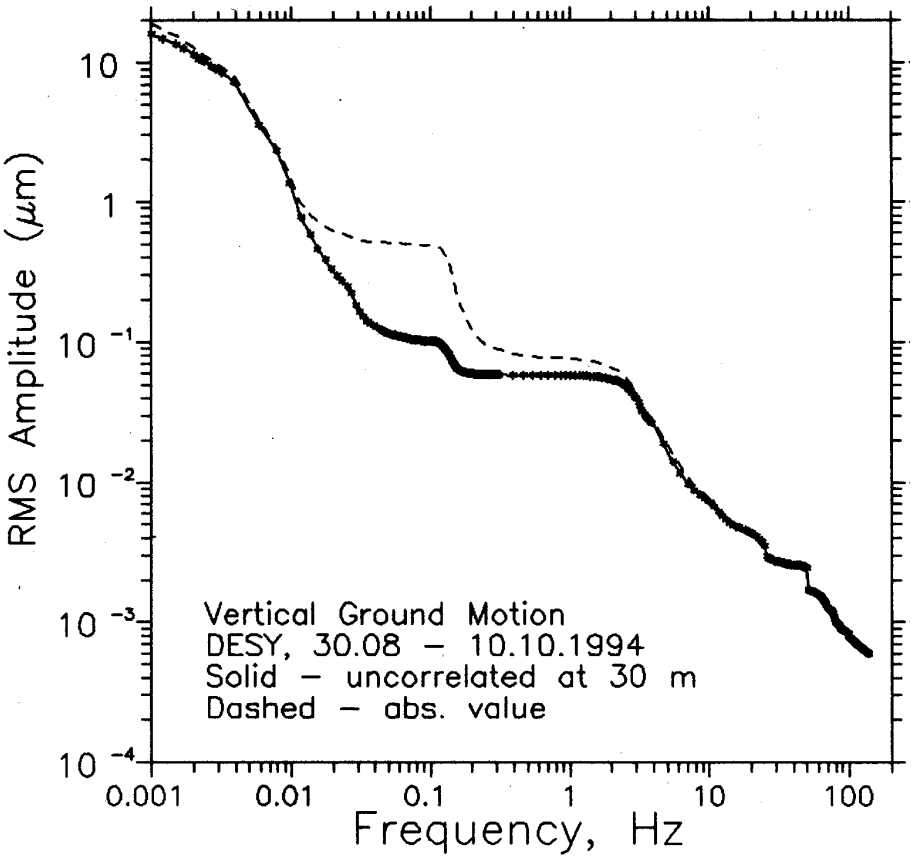

Figure 1.2: rms values of ground motion measured in HERA hall West, calculated by integrating the corresponding spectrum from f_0 to infinity. The obtained rms value is shown as a function of this lower frequency f_0 (see eqn. (6.1)). For example, the rms ground motion for frequencies higher than 2 Hz is about 70 nm.

tive mechanical stabilization system has been developed. It is based on geophones as vibration sensors and piezoelectric actuators to decouple the linac magnets from ground motion. The aim of this thesis is to demonstrate the viability of active quadrupole stabilization in a typical accelerator environment.

This system is installed in the S-band test facility at DESY, a 450 MeV linac where new techniques required for the future linear collider will be installed and tested. The test facility basically consists of two modular units similar to those to be installed in the future machine. Each unit consists of a 150 MW klystron providing the rf-power for two 6 m long accelerating structures, as shown in fig. 1.3. Between the accelerating structures quadrupole triplets are installed to focus the beam. Figure 1.4 shows a sketch of the S-band test facility.

The first part of this thesis describes ground motion measurements performed in HERA hall West which indicate that ground motion might cause significant luminosity degradation in the S-band Linear Collider SBLC. These measurements led to the proposal for active stabilization

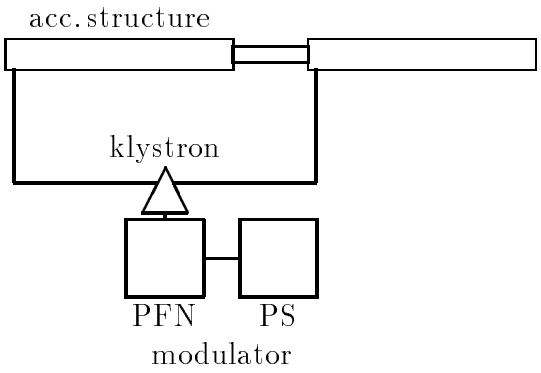

Figure 1.3: Schematic drawing of one S-band rf-module, consisting of two 6 m long accelerating structures powered by one 150 MW klystron with corresponding modulator, consisting of a power supply (PS) and a pulse forming network (PFN).

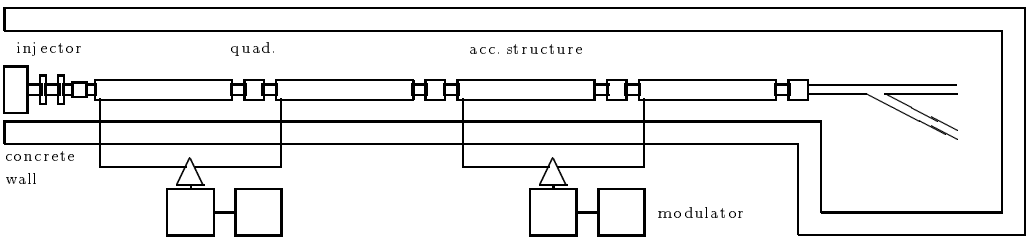

Figure 1.4: Sketch of the S-band test facility at DESY, consisting of the injector and two rf-modules with quadrupole triplets between the accelerating sections.

of mechanical quadrupole vibrations. The second part describes the active stabilization system and the considerations that led to the present design. In the third part simulation results of SBLC beam dynamics under the influence of realistic ground motion conditions with and without active stabilization are presented.

2 Ground motion measurements

In recent years ground motion measurements have been performed at many high energy physics laboratories as it was realized that they could be potentially harmful to the operation of future accelerators including e^+e^- linear colliders [Bak 91b, Oga 92, Bak 93, Tak 93, Jou 93], synchrotron radiation sources [Jen 91, Leb 92, Sug 92, Shi 94] and the proton storage rings LHC and SSC [Fis 92, Bak 91a, Par 93]. In contrast to most existing colliders where both beams share the same magnetic fields the latter facilities as well as linear colliders make use of separated beam optics.

In e^+e^-storage rings like LEP or $p\overline{p}$ machines like the TEVATRON both beams travel through the same magnets in opposite directions. The closed orbit in any arrangement of magnetic optics does not change if both charge and direction of the beam are reversed. The revolution frequencies are very high compared to typical ground motion frequencies, therefore such disturbances are quasi-static and both beams are deflected by the same amount. Therefore the beams will always collide head-on. This is no longer the case in an accelerator with separated beam optics, like a linear collider.

The investigation of quadrupole jitter effects on the beam dynamics in a linear collider requires a detailed understanding of ground motion properties, since they are a main source for magnet motion. Therefore different kinds of measurements have been performed in order to determine the correlation of ground motion at two points separated by several meters as well as the uncorrelated long-term drift which is considered to be described by the *ATL* rule [Bak 93] (see below).

The sensitivity of beam orbits depends strongly on the correlation lengths of magnet vibrations. Quadrupole motion which is correlated over distances exceeding the betatron wavelength (see Section 8.1) has only little influence on the beam jitter [Ros 88, Rau 91]. Therefore it is necessary to measure not only the spectrum of ground motion but also its correlation properties. A large effort was made in order to determine vibration sources and correlation properties of ground motion using different techniques including seismometers, wire alignment systems, tiltmeters etc. as well as the beam itself [Bri 94].

The determination of correlation properties requires measurement of motion at two points with respect to an inertial frame of reference ("absolute" motion), while a relative motion measurement is sufficient for the investigation of uncorrelated drift.

Therefore low-noise, long-period seismometers were employed in the first case while the latter was based on the wire alignment system installed in the Final Focus Test Beam (FFTB) tunnel at SLAC.

The ground motion spectrum can be divided into two main regions, the high frequency region above approximately 5 Hz dominated by so-called cultural noise, e. g. traffic, industry, large transformers etc., and the low frequency region caused by natural motion sources like earth tides and ocean waves [Fis 85].

As measurements show, many of these vibrations have well-defined sources with characteristic spectra which can in principle be identified, for example the very sharp peak at 50 Hz caused by large transformers and other electrical equipment powered at this frequency. In practice this identification is not trivial in most cases.

In the case of high frequency cultural noise it has been observed that vibration amplitudes are significantly higher in the vicinity of main roads, railways, and industrial areas. This might lead to the proposal of building future accelerators in regions with low population and correspondingly low cultural noise level, but on the other hand the vibration level caused by the

accelerator environment itself is not negligible. It has been observed that vibration amplitudes decrease significantly when accelerators with their associated cooling water, high power transformers, etc. are switched off [Huk 86, Jou 93, Tur 95b]. Long-term measurements also show characteristic variations in ground motion amplitudes depending on the time of the day (amplitudes during working hours are much higher than during night time) as well as on the day of the week, with weekends significantly more quiet than working days [Dec 90]. This is also an indication for the man-made nature of these motions.
In contrast to this, low frequency vibrations are mainly of natural origin, the dominant one occuring due to the tidal motion at a period of about 12 hours. The effect of tidal motion on beam behaviour can be neglected in most cases due to its enormous correlation length, even though the corresponding amplitudes are very large compared to typical beam sizes.
Ground motion is also influenced by meteorological conditions. For example, air pressure fluctuations lead to a typical ground motion power spectrum of

$$p(\omega) = \frac{C}{\omega^{\frac{7}{3}}} \tag{2.1}$$

with $C \approx 5.5 \cdot 10^{-15}\,\mathrm{m^2 sec^{-\frac{4}{3}}}$ [Shi 95, Bak 91a, Bak 91b].
Another meteorological effect which influences ground motion is rainfall, since the additional weight of the water presses on deeper layers of the ground. On the other hand the increasing ground water level lifts the ground surface, due to buoyancy, as the water level rises.
A significant peak occurs at frequencies of typically 1/7 Hz, usually called the microseismic peak. This phenomenon is caused by ocean waves hitting coasts, resulting in well-correlated ground motion waves with wavelengths of some 20 km, hardly attenuated even over distances of hundreds of kilometers [Hau 63]. Therefore, this peak is observable practically all over the world, even in the central region of continents. A directional analysis of the microseismic motion at DESY clearly shows two major directions, one pointing to the Norwegian west coast of the North Sea, the other to the German coast of the Baltic Sea [Shi 95], clearly indicating waves on these two nearby seas as origins of ground motion at these frequencies. The amplitude as well as the frequency of the microseismic peak depend slightly on the weather conditions above the corresponding ocean, resulting in different heights and period lengths of sea waves and therefore in varying ground motion signals. The wavelengths of the microseismic motion are very large compared to the betatron wavelength of any accelerator planned or in operation, thus its effect on the beam dynamics can be neglected in spite of its quite large typical amplitude of 1 μm.
A second clearly visible broad peak around 2.5 Hz reflects some bandpass behaviour of the upper earth's crust [Tak 93], with typical wavelengths of some 200 m [Ser 95]. This length is comparable to the betatron wavelength or the FODO cell length in the high energy part of typical linear collider designs (see Section 8.1), thus considered potentially harmful in terms of orbit stability and emittance growth. Therefore its effect on the beam dynamics in a linear collider must be carefully investigated.
In addition to the quasi-stationary ground motion signals mentioned above, rare events like earthquakes should also be taken into account. Though Hamburg is a rather quiet seismic site remote seismic events occuring around the world are clearly detectable and identifiable [Shi 95] due to their typical signature.
At the beginning of an earthquake primary compression waves with amplitudes of some 50 to 100 μm can be detected at periods of 20 ... 30 sec, followed by secondary transverse waves of about three times larger amplitude and periods of 30 ... 50 sec. The propagation velocity of these waves ranges from about $5\,\mathrm{km \cdot sec^{-1}}$ (secondary transverse waves) to $8\,\mathrm{km \cdot sec^{-1}}$, the

corresponding wavelength thus exceeding 100 km. Therefore the effect of earthquakes at large distances from the accelerator is negligible. Additionally, earthquakes are rather rare seismic events, as can be estimated from the Gutenberg-Richter law used to predict the number of earthquakes N per year with magnitudes M in a certain interval. The resulting numbers are given in table 2.1 [Ker 85].

In contrast to these ground motion events with their known origins some ambient diffusion

M	events/year
≥ 9.0	0
$8.0 \ldots 8.9$	2
$7.0 \ldots 7.9$	18
$6.0 \ldots 6.9$	150
$5.0 \ldots 5.9$	800
$4.0 \ldots 4.9$	6200
$3.0 \ldots 3.9$	49000

Table 2.1: Predicted number of earthquakes with magnitude M per year [Ker 85].

processes are always present, resulting in unpredictable uncorrelated low frequency drift. It has been observed that the variance of uncorrelated relative motion of two points is proportional to their distance L and the time interval T of observation. This observation is summarized in the empiric so-called ATL rule [Bak 93],

$$\sigma^2 = A \cdot T \cdot L, \tag{2.2}$$

where A is a proportionality constant in the range [Bak 93, Par 94, Bri 94]

$$A \approx 10^{-8} \ldots 10^{-4} \, \frac{\mu\mathrm{m}}{\mathrm{m} \cdot \mathrm{sec}}. \tag{2.3}$$

The ATL rule describes a random walk process in time as well as in space. It can be understood by assuming a fractal model of the ground motion [Shi 92]. The magnitude of the proportionality constant A is influenced by the number of "cracks" in the ground between the two points and by the number of excitations during the measurement time. Therefore the constant A depends on the composition of the ground, resulting in significantly larger values on sand (with a large number of "cracks" per meter), e. g. the DESY site, than in rocky environments, e. g. the Swiss Jura at CERN. Additionally, excitation effects including variations in ground water level lead to a larger A, thus this proportionality "constant" is site-dependent.

Methods of data treatment useful in the analysis of ground motion are introduced here. The variance σ^2 of a time signal $x(t)$ with mean value zero can be calculated from the time signal as

$$\sigma^2 = \lim_{T \to \infty} \frac{1}{T} \int_{-\frac{T}{2}}^{\frac{T}{2}} x^2(t) \, \mathrm{d}t \tag{2.4}$$

and from its power spectrum (or power spectrum density, PSD)

$$p(\omega) = \lim_{T \to \infty} \frac{2}{T} \left| \int_{-\frac{T}{2}}^{\frac{T}{2}} x(t) \exp(-i\omega t) \, \mathrm{d}t \right|^2 \tag{2.5}$$

as

$$\sigma^2 = \int_0^\infty p(\omega)\,\frac{\mathrm{d}\omega}{2\pi}. \tag{2.6}$$

As usual, $\omega = 2\pi f$ here. The factor of 2 in the definition of the power spectrum ensures the validity of eqn. (2.6). In some textbooks a different convention without this factor 2 is used. In this case the integral in eqn. (2.6) extends from $-\infty$ to ∞, which for some theoretical calculations is more convenient.
For this reason, we use this alternative definition of the power spectrum in this subsection (equations (2.7) to (2.29)):

$$p(\omega) = \lim_{T\to\infty} \frac{1}{T} \left| \int_{-\frac{T}{2}}^{\frac{T}{2}} x(t) \exp(-i\omega t)\,\mathrm{d}t \right|^2, \tag{2.7}$$

with

$$\sigma^2 = \int_{-\infty}^\infty p(\omega)\,\frac{\mathrm{d}\omega}{2\pi}. \tag{2.8}$$

Using ground motion data $x_1(t)$ and $x_2(t)$ taken by two sensors simultaneously, the so-called mutual power spectrum $p_{12}(\omega)$ of the two signals is defined as

$$p_{12}(\omega) = \lim_{T\to\infty} \frac{1}{T} \int_{-\frac{T}{2}}^{\frac{T}{2}} x_1(t) \exp(-i\omega t)\,\mathrm{d}t \int_{-\frac{T}{2}}^{\frac{T}{2}} x_2(t) \exp(-i\omega t')\,\mathrm{d}t', \tag{2.9}$$

which, in contrast to the absolute spectrum $p(\omega)$, is complex. In the case of identical signals, $x_1(t) = x_2(t)$, we have $p_{12}(\omega) = p_{11}(\omega) = p_{22}(\omega) = p(\omega)$.
Since $p_{12}^* = p_{21}$, its real and imaginary parts can be calculated as

$$\begin{aligned} 2i\Im(p_{12}) &= p_{12} - p_{12}^* \\ &= p_{12} - p_{21} \qquad (2.10) \\ 2\Re(p_{12}) &= p_{12} + p_{12}^* \\ &= p_{12} + p_{21}. \qquad (2.11) \end{aligned}$$

The correlation (or normalized mutual power spectrum) can be computed from the mutual power spectrum $p_{12}(\omega)$ and the power spectra $p_{11}(\omega)$ and $p_{22}(\omega)$ of the two time signals $x_1(t)$ and $x_2(t)$ as

$$\gamma(\omega) = \frac{p_{12}(\omega)}{\sqrt{p_{11}(\omega) p_{22}(\omega)}}. \tag{2.12}$$

According to eqn. (2.5) the power spectrum $\rho(\omega, \Delta L)$ of relative motion, i. e. of the difference signal $x_1(t) - x_2(t)$, is given by

$$\begin{aligned} \rho(\omega, \Delta L) &= \lim_{T\to\infty} \frac{1}{T} \left| \int_{-\frac{T}{2}}^{\frac{T}{2}} [x_1(t) - x_2(t)] \exp(-i\omega t)\,\mathrm{d}t \right|^2 \\ &= \lim_{T\to\infty} \frac{1}{T} \left| \int_{-\frac{T}{2}}^{\frac{T}{2}} [x(t, s_1) - x(t, s_2) \exp(-i\omega t)\,\mathrm{d}t] \right|^2. \end{aligned} \tag{2.13}$$

Under the assumption that averaged properties do not depend on the absolute longitudinal positions s_1 and s_2 but only on the distance $\Delta L = s_2 - s_1$ we can denote

$$s_1 = s \tag{2.14}$$
$$s_2 = s + \Delta L \tag{2.15}$$

and average over the longitudinal position:

$$\begin{aligned}
\rho(\omega, \Delta L) &= \lim_{L\to\infty}\lim_{T\to\infty}\frac{1}{L}\frac{1}{T}\int_{-\frac{L}{2}}^{\frac{L}{2}}\left|\int_{-\frac{T}{2}}^{\frac{T}{2}}[x(t,s)-x(t,s+\Delta L)]\exp(-i\omega t)\,\mathrm{d}t\right|^2\,\mathrm{d}s \\
&= \lim_{L\to\infty}\lim_{T\to\infty}\frac{1}{L}\frac{1}{T}\int_{-\frac{L}{2}}^{\frac{L}{2}}\int_{-\frac{T}{2}}^{\frac{T}{2}}\int_{-\frac{T}{2}}^{\frac{T}{2}}\exp(-i\omega t)\cdot\exp(i\omega t') \\
&\quad [x(t,s)-x(t,s+\Delta L)]\cdot[x^*(t',s)-x^*(t',s+\Delta L)]\,\mathrm{d}t\mathrm{d}t'\mathrm{d}s \\
&= \lim_{L\to\infty}\lim_{T\to\infty}\frac{1}{L}\frac{1}{T}\int_{-\frac{L}{2}}^{\frac{L}{2}}\int_{-\frac{T}{2}}^{\frac{T}{2}}\int_{-\frac{T}{2}}^{\frac{T}{2}}\exp(-i\omega t)\cdot\exp(i\omega t') \\
&\quad [x(t,s)x^*(t',s)+x(t,s+\Delta L)x^*(t',s+\Delta L) \\
&\quad -x(t,s)x^*(t',s+\Delta L)-x(t,s+\Delta L)x^*(t',s)]\,\mathrm{d}t\mathrm{d}t'\mathrm{d}s \\
&= \lim_{L\to\infty}\lim_{T\to\infty}\frac{1}{L}\frac{1}{T}\int_{-\frac{L}{2}}^{\frac{L}{2}}\int_{-\frac{T}{2}}^{\frac{T}{2}}\int_{-\frac{T}{2}}^{\frac{T}{2}}\exp(-i\omega t)\cdot\exp(i\omega t') \\
&\quad 2[x(t,s)x^*(t',s)-x(t,s)x^*(t',s+\Delta L)]\mathrm{d}t\mathrm{d}t'\mathrm{d}s \\
&= p_{11}(\omega)+p_{22}(\omega)-p_{12}(\omega,\Delta L)-p_{21}(\omega,\Delta L).
\end{aligned} \tag{2.16}$$

Here ΔL is the distance between the two measurement locations.
The variance $\sigma^2(\Delta L)$ is expressed as

$$\begin{aligned}
\sigma^2(\Delta L) &= \int_{-\infty}^{\infty}\rho(\omega,\Delta L)\,\frac{\mathrm{d}\omega}{2\pi} \\
&= \lim_{T\to\infty}\frac{1}{T}\int_{-\frac{T}{2}}^{\frac{T}{2}}[x_1(t)-x_2(t)]^2\,\mathrm{d}t,
\end{aligned} \tag{2.17}$$

in analogy with eqns. (2.4) and (2.6).
For an analytical description of ground motion a two-dimensional power spectrum of the displacement $x(t,s)$ can be introduced as [Ser 95]

$$P(\omega,k) = \lim_{T\to\infty}\lim_{L\to\infty}\frac{1}{T}\frac{1}{L}\left|\int_{-\frac{L}{2}}^{\frac{L}{2}}\int_{-\frac{T}{2}}^{\frac{T}{2}}x(t,s)\exp(-i\omega t)\exp(-iks)\,\mathrm{d}t\mathrm{d}s\right|^2 \tag{2.18}$$

with $k = 2\pi/\lambda$. This spectrum contains information about both relative and absolute motion. The absolute spectrum $p(\omega)$ can be derived as

$$\begin{aligned}
\int_{-\infty}^{\infty}P(\omega,k)\,\frac{\mathrm{d}k}{2\pi} &= \int_{-\infty}^{\infty}\lim_{T\to\infty}\lim_{L\to\infty}\frac{1}{T}\frac{1}{L}\left|\int_{-\frac{L}{2}}^{\frac{L}{2}}\int_{-\frac{T}{2}}^{\frac{T}{2}}x(t,s)\exp(-i\omega t)\exp(-iks)\,\mathrm{d}t\mathrm{d}s\right|^2\,\frac{\mathrm{d}k}{2\pi} \\
&= \int_{-\infty}^{\infty}\lim_{T\to\infty}\lim_{L\to\infty}\frac{1}{T}\frac{1}{L}\int_{-\frac{L}{2}}^{\frac{L}{2}}\int_{-\frac{T}{2}}^{\frac{T}{2}}x(t,s)\exp(-i\omega t)\exp(-iks)\,\mathrm{d}t\mathrm{d}s \\
&\quad \int_{-\frac{L}{2}}^{\frac{L}{2}}\int_{-\frac{T}{2}}^{\frac{T}{2}}x(t',s')\exp(i\omega t')\exp(iks')\,\mathrm{d}t'\mathrm{d}s'\frac{\mathrm{d}k}{2\pi}
\end{aligned}$$

$$
\begin{aligned}
&= \lim_{T\to\infty}\frac{1}{T}\int_{-\frac{T}{2}}^{\frac{T}{2}}\int_{-\frac{T}{2}}^{\frac{T}{2}}\exp[-i\omega(t-t')] \\
&\quad \int_{-\infty}^{\infty}\lim_{L\to\infty}\frac{1}{L}\int_{-\frac{L}{2}}^{\frac{L}{2}}\int_{-\frac{L}{2}}^{\frac{L}{2}}x(t,s)x(t',s')\exp[-ik(s-s')]\,\mathrm{d}s\mathrm{d}s'\frac{\mathrm{d}k}{2\pi}\mathrm{d}t\mathrm{d}t' \\
&= \lim_{T\to\infty}\frac{1}{T}\int_{-\frac{T}{2}}^{\frac{T}{2}}\int_{-\frac{T}{2}}^{\frac{T}{2}}\exp[-i\omega(t-t')]x(t,L)x(t',L)\,\mathrm{d}t\mathrm{d}t' \\
&= \lim_{T\to\infty}\frac{1}{T}\left|\int_{-\frac{T}{2}}^{\frac{T}{2}}x(t,L)\exp(-i\omega t)\,\mathrm{d}t\right|^2 \\
&= p(\omega), \qquad (2.19)
\end{aligned}
$$

and therefore

$$
\begin{aligned}
\sigma^2 &= \int_{-\infty}^{\infty}p(\omega)\,\frac{\mathrm{d}\omega}{2\pi} \\
&= \int_{-\infty}^{\infty}\int_{-\infty}^{\infty}P(\omega,k)\,\frac{\mathrm{d}\omega}{2\pi}\frac{\mathrm{d}k}{2\pi}, \qquad (2.20)
\end{aligned}
$$

while for the spectrum $\rho(\omega,\Delta L)$ of relative motion we get [Ser 95]

$$
\rho(\omega,\Delta L)=\int_{-\infty}^{\infty}P(\omega,k)2[1-\cos(k\Delta L)]\,\frac{\mathrm{d}k}{2\pi}. \qquad (2.21)
$$

The consistency with eqn. (2.13) can be shown as follows:

$$
\begin{aligned}
\rho(\omega,\Delta L) &= \int_{-\infty}^{\infty}\lim_{T\to\infty}\lim_{L\to\infty}\frac{1}{T}\frac{1}{L}\left|\int_{-\frac{T}{2}}^{\frac{T}{2}}\int_{-\frac{L}{2}}^{\frac{L}{2}}x(t,s)\exp(-i\omega t)\exp(-iks)\,\mathrm{d}s\mathrm{d}t\right|^2 \\
&\quad \cdot 2[1-\exp(-ik\Delta L)]\,\frac{\mathrm{d}k}{2\pi} \\
&= \int_{-\infty}^{\infty}\lim_{T\to\infty}\lim_{L\to\infty}\frac{1}{T}\frac{1}{L}\int_{-\frac{T}{2}}^{\frac{T}{2}}\int_{-\frac{T}{2}}^{\frac{T}{2}}\int_{-\frac{L}{2}}^{\frac{L}{2}}\int_{-\frac{L}{2}}^{\frac{L}{2}}x(t,s)x^*(t',s') \\
&\quad \exp(-i\omega t)\exp(-iks)\exp(i\omega t')\exp(iks')\,\mathrm{d}t\mathrm{d}t'\mathrm{d}s\mathrm{d}s' \\
&\quad \cdot 2[1-\exp(-ik\Delta L)]\,\frac{\mathrm{d}k}{2\pi}. \qquad (2.22)
\end{aligned}
$$

Using

$$
\begin{aligned}
\int_{-\infty}^{\infty}\exp[-ik(s-s')]\,\frac{\mathrm{d}k}{2\pi} &= \delta(s-s') \qquad (2.23) \\
\int_{-\infty}^{\infty}\exp[-ik(s-s'+\Delta L)]\,\frac{\mathrm{d}k}{2\pi} &= \delta(s-s'+\Delta L), \qquad (2.24)
\end{aligned}
$$

we finally get

$$
\begin{aligned}
\rho(\omega,\Delta L) &= \lim_{T\to\infty}\lim_{L\to\infty}\frac{1}{T}\frac{1}{L}\int_{-\frac{T}{2}}^{\frac{T}{2}}\int_{-\frac{T}{2}}^{\frac{T}{2}}\int_{-\frac{L}{2}}^{\frac{L}{2}}\int_{-\frac{L}{2}}^{\frac{L}{2}}x(t,s)x^*(t',s') \\
&\quad \exp(-i\omega t)\exp(i\omega t')\cdot 2[\delta(s-s')-\delta(s-s'+\Delta L)]\,\mathrm{d}t\mathrm{d}t'\mathrm{d}s\mathrm{d}s' \\
&= \lim_{L\to\infty}\lim_{T\to\infty}\frac{1}{L}\frac{1}{T}\int_{-\frac{L}{2}}^{\frac{L}{2}}\int_{-\frac{T}{2}}^{\frac{T}{2}}\int_{-\frac{T}{2}}^{\frac{T}{2}}\exp(-i\omega t)\exp(i\omega t') \\
&\quad \cdot 2[x(t,s)x^*(t',s)-x(t,s)x^*(t',s+\Delta L)]\,\mathrm{d}t\mathrm{d}t'\mathrm{d}s, \qquad (2.25)
\end{aligned}
$$

which is the same result as eqn. (2.16). The corresponding back-transformation yields

$$\begin{aligned} P(\omega,k) &= \int_0^\infty \cos(k\Delta L)[\rho(\omega,\Delta L=\infty)-\rho(\omega,\Delta L)]\,\mathrm{d}(\Delta L) \\ &= \int_0^\infty \cos(k\Delta L)[2p(\omega)-\rho(\omega,\Delta L)]\,\mathrm{d}(\Delta L). \end{aligned} \tag{2.26}$$

Here we have used the fact that correlations vanish at infinite distance L, resulting in a power spectrum of relative motion equal to $2p(\omega)$.
For the two-dimensional spectrum describing the ATL rule we get

$$P(\omega,k) = \frac{A}{\omega^2 k^2}, \tag{2.27}$$

because

$$\begin{aligned} \sigma^2(\Delta T,\Delta L) &= \int_{-\infty}^\infty\int_{-\infty}^\infty P(\omega,k)2[1-\cos(\omega\Delta T)]2[1-\cos(k\Delta L)]\,\frac{\mathrm{d}\omega}{2\pi}\frac{\mathrm{d}k}{2\pi} \\ &= \int_{-\infty}^\infty\int_{-\infty}^\infty \frac{A}{\omega^2k^2}2[1-\cos(\omega\Delta T)]2[1-\cos(k\Delta L)]\,\frac{\mathrm{d}\omega}{2\pi}\frac{\mathrm{d}k}{2\pi} \\ &= A\cdot\Delta T\cdot\Delta L. \end{aligned} \tag{2.28}$$

Also,

$$\begin{aligned} \rho(\omega,\Delta L) &= \int_{-\infty}^\infty P(\omega,k)2[1-\cos(k\Delta L)]\,\frac{\mathrm{d}k}{2\pi} \\ &= \int_{-\infty}^\infty \frac{A}{\omega^2k^2}2[1-\cos(k\Delta L)]\,\frac{\mathrm{d}k}{2\pi} \\ &= \frac{A\Delta L}{\omega^2}. \end{aligned} \tag{2.29}$$

2.1 Instrumentation

Two types of seismometers were used in correlation measurements performed in HERA hall West. Using sophisticated electronics, these sensors cover large bandwidths ranging from several mHz to approximately 100 Hz (see Section 4). Table 2.2 shows an excerpt of the data sheets of both sensor types.
While the CMG-3T sensor made by Guralp Systems Ltd. reaches lower frequencies, the upper frequency limit of the SM3-KV seismometer built by the Moscow Institute of Physics of the Earth is approximately three times larger than that of the CMG-3T. As these data indicate, both devices complement each other.

Figure 2.1 shows a comparison of the internal noise of these instruments as provided by the manufacturers with the New Low Noise Model NLNM [Pet 93], a composition of the lowest ground motion amplitudes measured at different quiet sites all over the world. The internal noise of the CMG-3T is below the NLNM in the frequency band from 0.01 to 10 Hz, while the electronic noise of the SM3-KV is significantly higher than that of the CMG-3T below approximately 0.8 Hz, but still below the NLNM between 0.1 and 20 Hz.

To avoid aliasing (see Appendix A), the output signals of the seismometers were processed with lowpass analog filters with cutoff frequencies of 0.5 ... 2000 Hz depending on the sampling rate. The signals were digitized at sampling rates between 0.1 and 32000 Hz using 20 bit CAMAC ADCs connected to a PC.

	SM3-KV	CMG-3T
Frequency band	0.05 . . . 140 Hz	0.003 . . . 50 Hz
Type	velocitymeter	velocitymeter
Output sensitivity	$80\ \frac{\mathrm{mV}}{\mu\mathrm{m/sec}}$	$0.75\ \frac{\mathrm{mV}}{\mu\mathrm{m/sec}}$
Sensor type	inductive	capacitive
Feedback transducer	electrodynamical	electrodynamical

Table 2.2: Seismometer data [Gur 93, Tra 77, Tok 84].

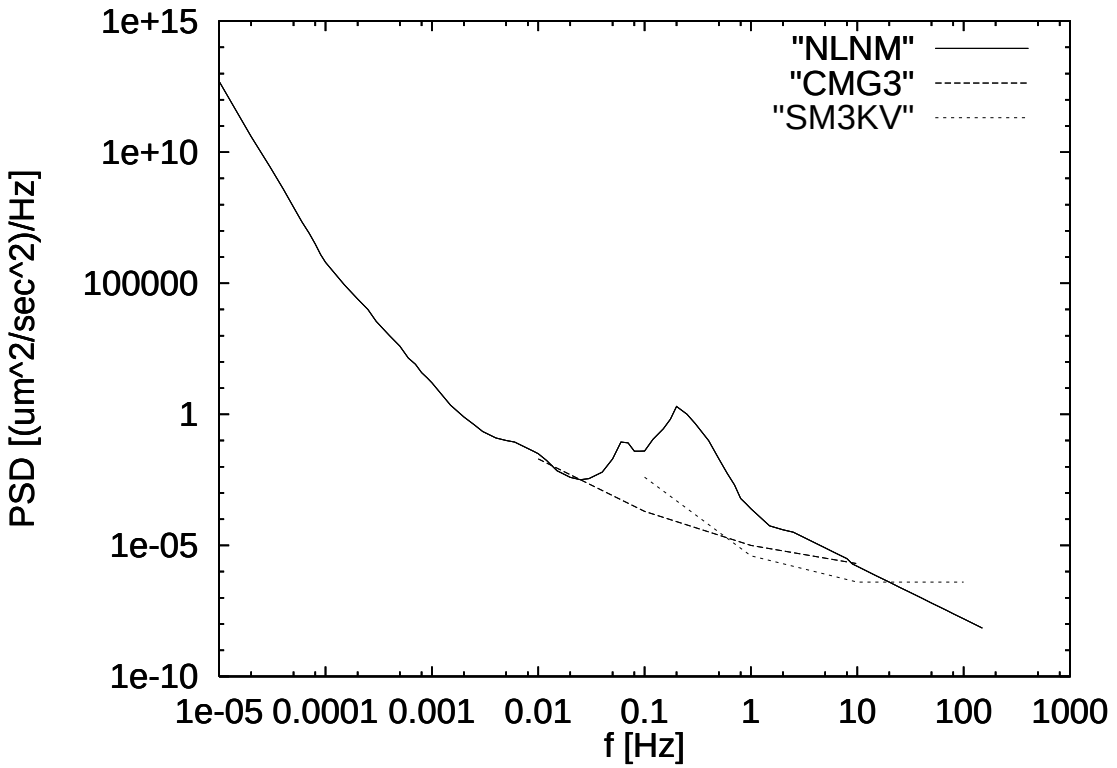

Figure 2.1: Comparison of the internal noise of the two seismometers with the New Low Noise Model NLNM.

It is difficult to extract the uncorrelated low frequency drift of the ground from seismometer signals representing "absolute" motion, i. e. motion with respect to an inertial frame of reference, due to the internal noise level of these instruments. Devices which measure only the relative motion of two points are more appropriate for this purpose.
The wire alignment system installed in the Final Focus Test Beam (FFTB) tunnel at SLAC is suitable to determine the constant A of the ATL rule, which describes uncorrelated drifts. This system consists of pairs of wires mounted in parallel to four straight sections of the beamline, shown schematically in fig. 2.2. A harmonic rf signal of 100 MHz is coupled to these wires. The end points of the wires (wire terminators, WT) are located near bending magnets in the FFTB beam line. One end of each wire is fixed to a terminator, the other is connected to a heavy mass of about 35 kg using a low friction pulley. Three high-resolution position monitors connected to each magnet measure the relative position of the magnet with respect to the wires, thus

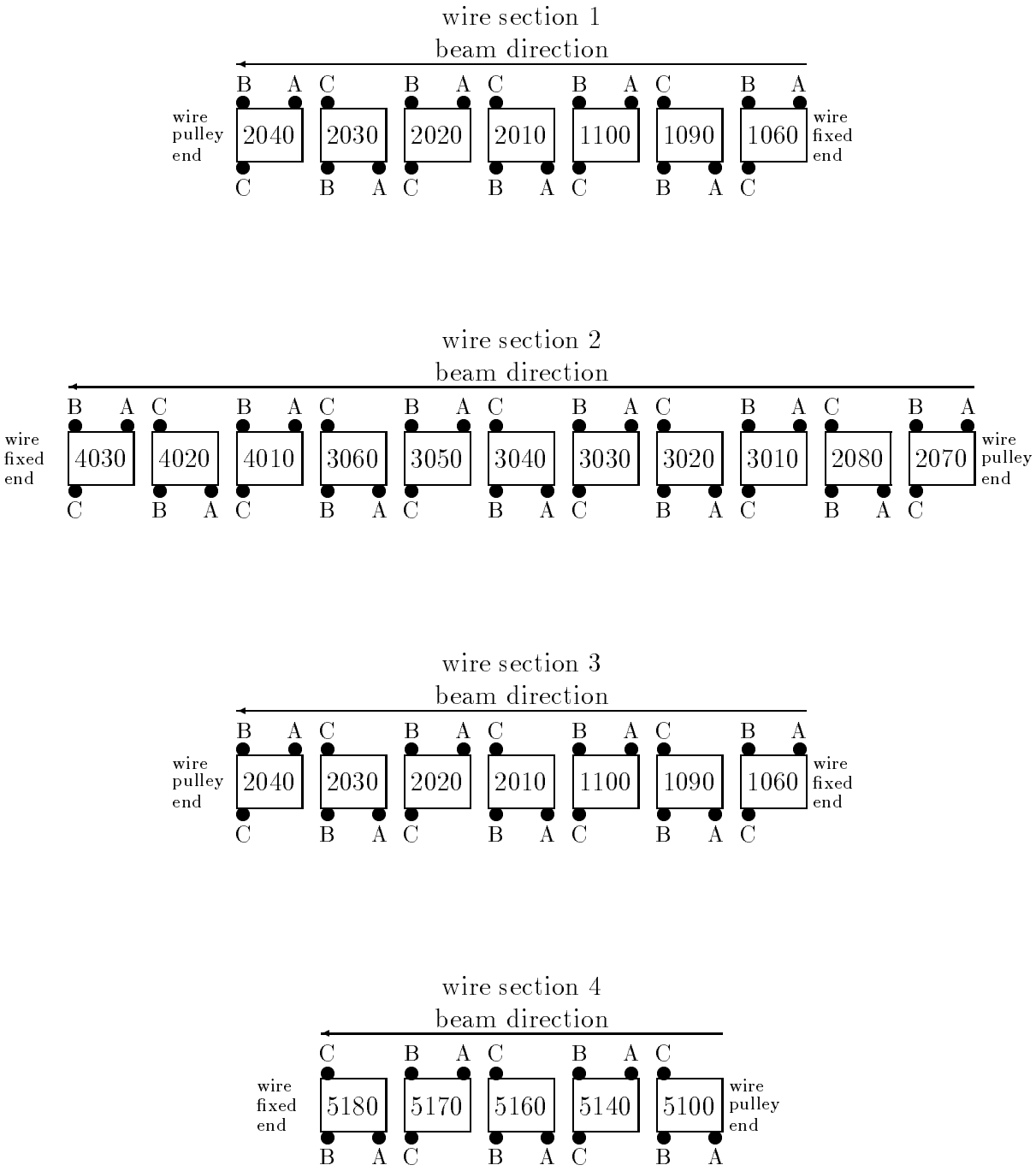

Figure 2.2: Schematic layout of the wire alignment system. The circles indicate the locations of the wire position monitors (A, B, C) in the four sections.

providing information about the transverse motion of the magnets as well as transverse and longitudinal rotations. The signals detected by the position monitors are mixed with a 50 kHz signal and are digitized with 16 bit ADCs, resulting in a resolution of 100 nm over a total range of 1.5 mm.
This system was developed by the DESY group MKI [Pet] based on the previous work of the DESY group MEA [Sch 90]. The data acquisition system is based on a PC network connected to the SLAC control system.

2.2 Results of ground motion measurements

It has been observed that ground motion power spectra depend on the time of the day when measurements take place, with nights being much more quiet than working hours, as well as on the day of the week, with amplitudes during working days being much higher than those during weekends [Dec 90]. The same is also true on a much smaller time scale. Therefore, the variance σ^2 of ground motion is also time dependent. In the theory of signal analysis, this characteristic is referred to as non-stationarity.
To overcome problems with the non-stationarity of ground motion, averaged power spectra are used in further analysis:

$$\Phi_{xx} = \langle p_{xx}(f) \rangle, \tag{2.30}$$
$$\Phi_{yy} = \langle p_{yy}(f) \rangle, \tag{2.31}$$
$$\Phi_{xy} = \langle p_{xy}(f) \rangle. \tag{2.32}$$

Here, p_{xx} and p_{yy} are the power spectra of two signals $x(t)$ and $y(t)$ measured in different places simultaneously (see eqn. (2.5)), while p_{xy} denotes the mutual power spectrum of these two signals (eqn. (2.9)). Using these averaged power spectra, the correlation function γ of two signals $x(t)$ and $y(t)$ is defined as

$$\gamma = \frac{\Phi_{xy}}{\sqrt{\Phi_{xx}\Phi_{yy}}}, \tag{2.33}$$

while its modulus $|\gamma|$ is referred to as the coherence of the signals.
The correlated part Φ_{ss} as well as the uncorrelated part Φ_{nn} of ground motion can be determined using the correlation function as (see Section 4)

$$\Phi_{nn} = \Phi_{yy} - |H|^2 \Phi_{xx}, \tag{2.34}$$
$$\Phi_{ss} = \Phi_{yy} \cdot |\gamma|^2, \tag{2.35}$$

with H being the ratio of the transfer functions of the two sensors involved. In the case of identical sensors, equation (2.34) reduces to

$$\Phi_{nn} = \Phi_{yy} - \Phi_{xx}. \tag{2.36}$$

To determine the properties of ground motion, two identical SM3-KV seismometers were placed at distances ranging from 5 to 30 m in the HERA hall West [Shi 95]. The coherence

$$|\gamma| = \frac{|\Phi_{xy}|}{\sqrt{\Phi_{xx}\Phi_{yy}}} \tag{2.37}$$

at vanishing distances was found to be practically unity in the frequency band ranging from 0.06 to 140 Hz, indicating that the internal noise level of the instruments is low compared to the ground motion signal in this frequency band. Therefore, any lack of coherence observed at larger distances between the sensors can be assumed to be a real property of ground motion. As expected, the coherence drops significantly if the distance between the probes is increased. Displaced by 5 m, decoherence occurs at frequencies higher than approximately 10 Hz with the only exception being a wide peak at about 50 Hz (fig. 2.3 a) caused by transformers and other electrical equipment operated at this frequency.

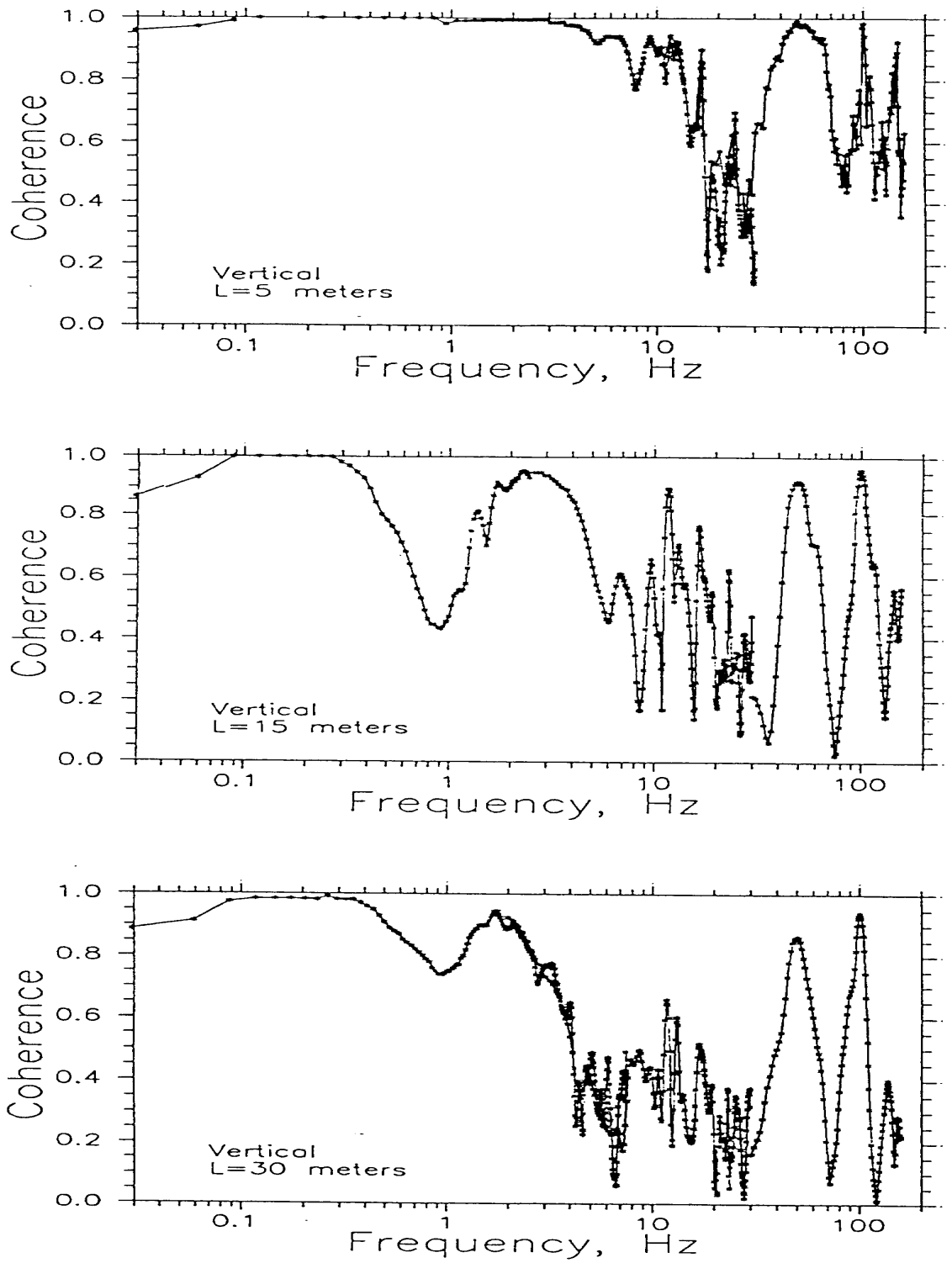

Figure 2.3: Coherence spectra of two SM3-KV seismometers separated by 5 m (a), 15 m (b) and 30 m (c), measured in HERA hall West.

Increasing the distance to 15 m (fig. 2.3 b) and to 30 m (fig. 2.3 c) leads to a loss of coherence at even lower frequencies. On the other hand, a comparison of figs. 2.3 b and c shows a larger

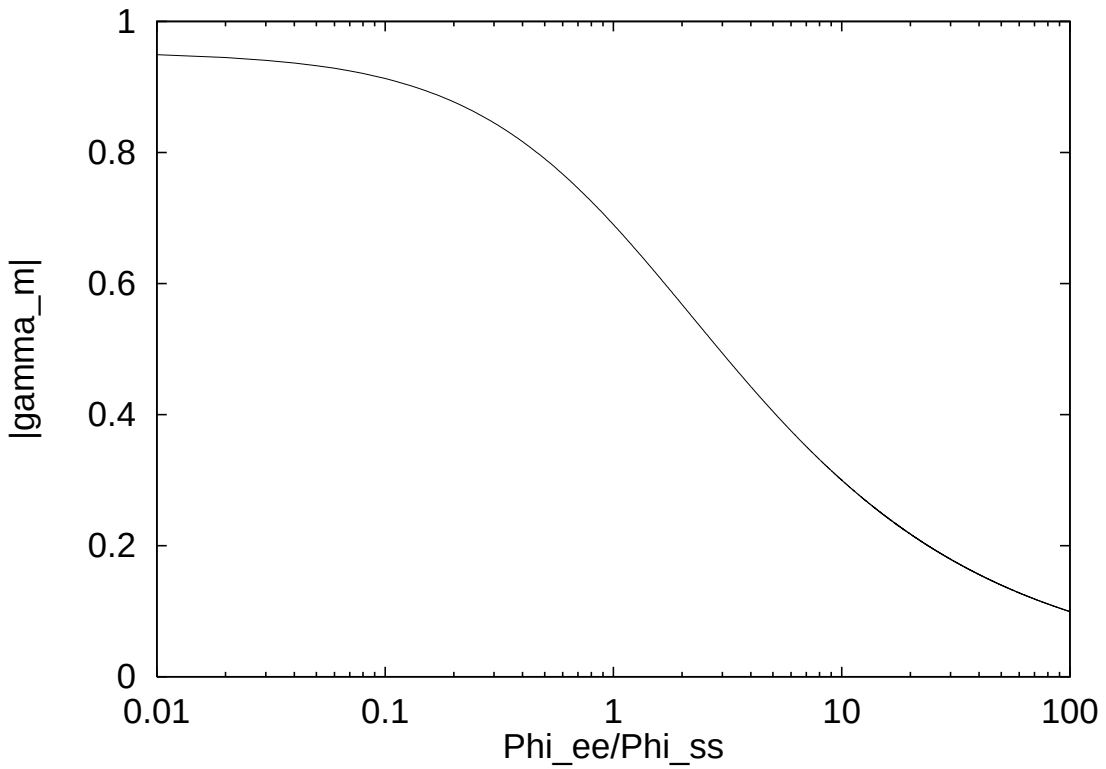

Figure 2.4: Measured coherence $|\gamma_m|$ as a function of the noise power Φ_{ee} for $\beta = 10$. The noise power Φ_{ee} is expressed in terms of the coherent signal power Φ_{ss}.

coherence in the band between 0.3 and 1 Hz for a distance of 30 m than for 15 m. Possible explanations include electrical noise picked-up by the sensor cables, temperature variations, air pressure fluctuations or air flow acting on the sensors. The measured coherence $|\gamma_m|$ in the presence of disturbances characterized by the power spectrum Φ_{ee} is (see Section 4)

$$\begin{aligned} |\gamma_m| &= \sqrt{\frac{\frac{\Phi_{ss}}{\Phi_{nn}+\Phi_{ee}}}{1+\frac{\Phi_{ss}}{\Phi_{nn}+\Phi_{ee}}}} \\ &= \sqrt{\frac{\Phi_{ss}}{\Phi_{ss}+\Phi_{nn}+\Phi_{ee}}} \\ &= \sqrt{\frac{\Phi_{ss}}{\Phi_{ss}+\frac{\Phi_{ss}}{\beta}+\Phi_{ee}}}, \end{aligned} \tag{2.38}$$

with $\beta = \Phi_{ss}/\Phi_{nn}$ being the ratio of the correlated and uncorrelated ground motion. Figure 2.4 shows the measured coherence $|\gamma_m|$ as a function of the noise Φ_{ee}, with $\beta = 10$.

This noise process Φ_{ee} is non-stationary, i. e. its power spectrum as well as its variance varies with time. To investigate the influence of these variations on the measured coherence $|\gamma_m|$, we compute the partial derivative of $|\gamma_m|$ with respect to Φ_{ee}. Using

$$\left|\frac{\partial|\gamma_m|}{\partial\Phi_{ee}}\right| = \frac{1}{2}\cdot\frac{\Phi_{ss}^{\frac{1}{2}}}{\left[\Phi_{ee}+\Phi_{ss}\left(\frac{1}{\beta}+1\right)\right]^{\frac{3}{2}}}, \tag{2.39}$$

one can show that the influence of noise on the measured coherence $|\gamma_m|$ increases with decreasing ground motion Φ_{ss}. For this reason, unexpected variations in the measured coherence for different distances L between the sensors should occur mainly in frequency bands where the ground motion signal is rather small. To illustrate this, figure 2.5 shows the modulus $|\mathrm{d}|\gamma_m|/\mathrm{d}\Phi_{ee}|$ as a function of the noise power Φ_{ee}, with $\beta = 10$ and $\Phi_{ss} = 1\,\mathrm{m}^2/\mathrm{Hz}$.
In addition to the previous considerations, we also need to quantify the effect of varying ground

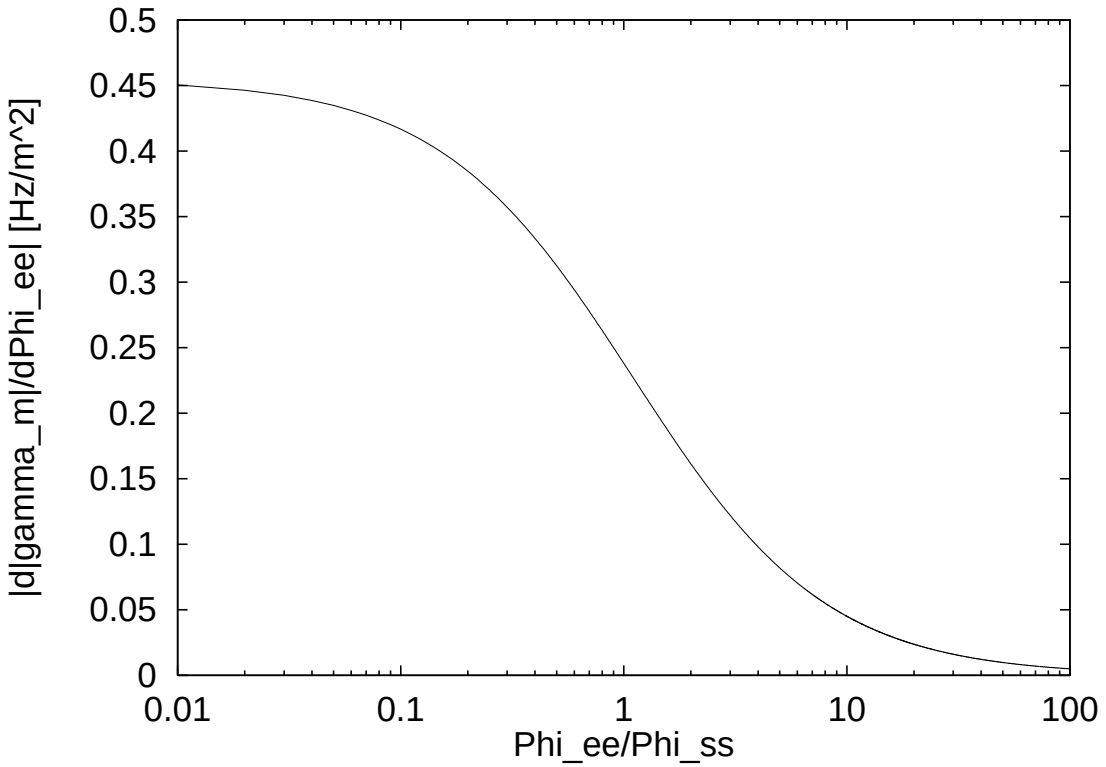

Figure 2.5: $|\mathrm{d}|\gamma_m|/\mathrm{d}\Phi_{ee}|$ as a function of the additional noise Φ_{ee} for $\beta = 10$. The noise power Φ_{ee} is expressed in terms of the coherent signal power $\Phi_{ss} = 1\,\mathrm{m}^2/\mathrm{Hz}$.

motion Φ_{ss} on the measured coherence in the presence of noise. To investigate this, the partial derivative

$$\left|\frac{\partial|\gamma_m|}{\partial\Phi_{ss}}\right| = \frac{\Phi_{ee}}{(1+\frac{1}{\beta}+\frac{\Phi_{ee}}{\Phi_{ss}})^{\frac{3}{2}}\cdot\Phi_{ss}^2} \tag{2.40}$$

has to be considered. As shown in figure 2.6, the effect of variations in Φ_{ss} grows rapidly as the ratio Φ_{ss}/Φ_{ee} decreases.
In contrast to the general tendency of decreasing coherence with increasing distance, ground motion remains well correlated at certain characteristic frequencies of $0.1\ldots0.2\,\mathrm{Hz}$ and at approximately $2.5\,\mathrm{Hz}$ (see fig. 2.3). A comparison with the power spectrum (fig. 2.7) shows that amplitudes in these frequency bands are significantly higher than in their vicinity, reflecting the microseismic peak as well as the resonant behaviour of the upper earth's crust, as mentioned above. Between $0.3\,\mathrm{Hz}$ and $1\,\mathrm{Hz}$, ground motion amplitudes are indeed quite low. Therefore,

the unexpected variations of coherence at these frequencies could be caused by external electrical noise.

We assume now perfectly correlated ground motion and try to estimate the amount of addi-

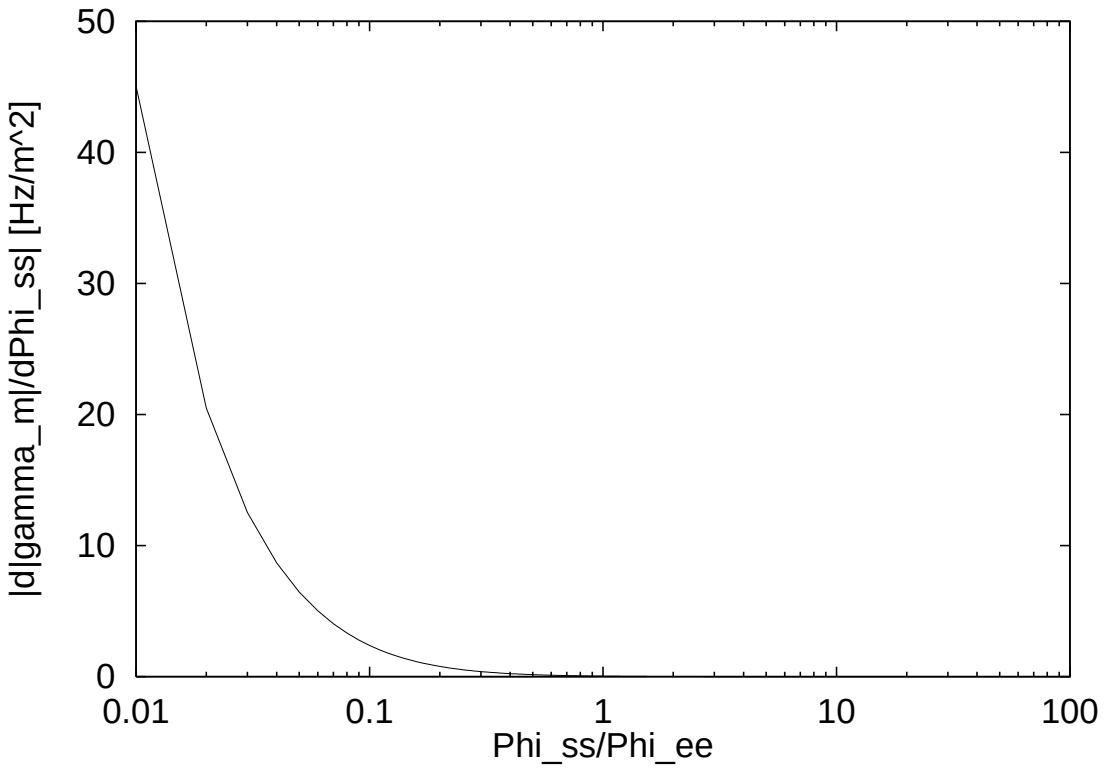

Figure 2.6: $|\mathrm{d}|\gamma_m|/\mathrm{d}\Phi_{ee}|$ as a function of the signal power Φ_{ss} for $\beta = 10$. The coherent ground motion power Φ_{ss} is expressed in terms of the noise power $\Phi_{ee} = 0.1\,\mathrm{m}^2/\mathrm{Hz}$.

tional noise Φ_{ee} which is needed to reproduce the measured coherence shown in fig. 2.3. The primary electrical signals transferred from the sensors to the ADCs are proportional to the velocity of the ground motion. If we assume that the electrical noise on the cables is white noise, the power spectrum of the noise is proportional to f^{-2} in the displacement power spectrum, with f being the frequency. Additionally, effects like air flow or temperature variations produce larger amplitudes of motion at low frequencies than at higher ones. Therefore, the power spectra of these disturbances are also assumed to be proportional to f^{-2}. Thus,

$$\Phi_{ee}(f) = \frac{C}{f^2}, \tag{2.41}$$

with the proportionality constant C.

An upper limit $C_{\max}$ for this proportionality constant can be estimated using the measured ground motion power spectrum (see fig. 2.7). The estimated noise power Φ_{ee} should be below this measured ground motion power Φ_{ss} over the whole frequency range for which it was measured. Otherwise the measured signals would be significantly larger, leading to a different spectrum. The measured ground motion power spectrum can be approximated as [Shi 95]

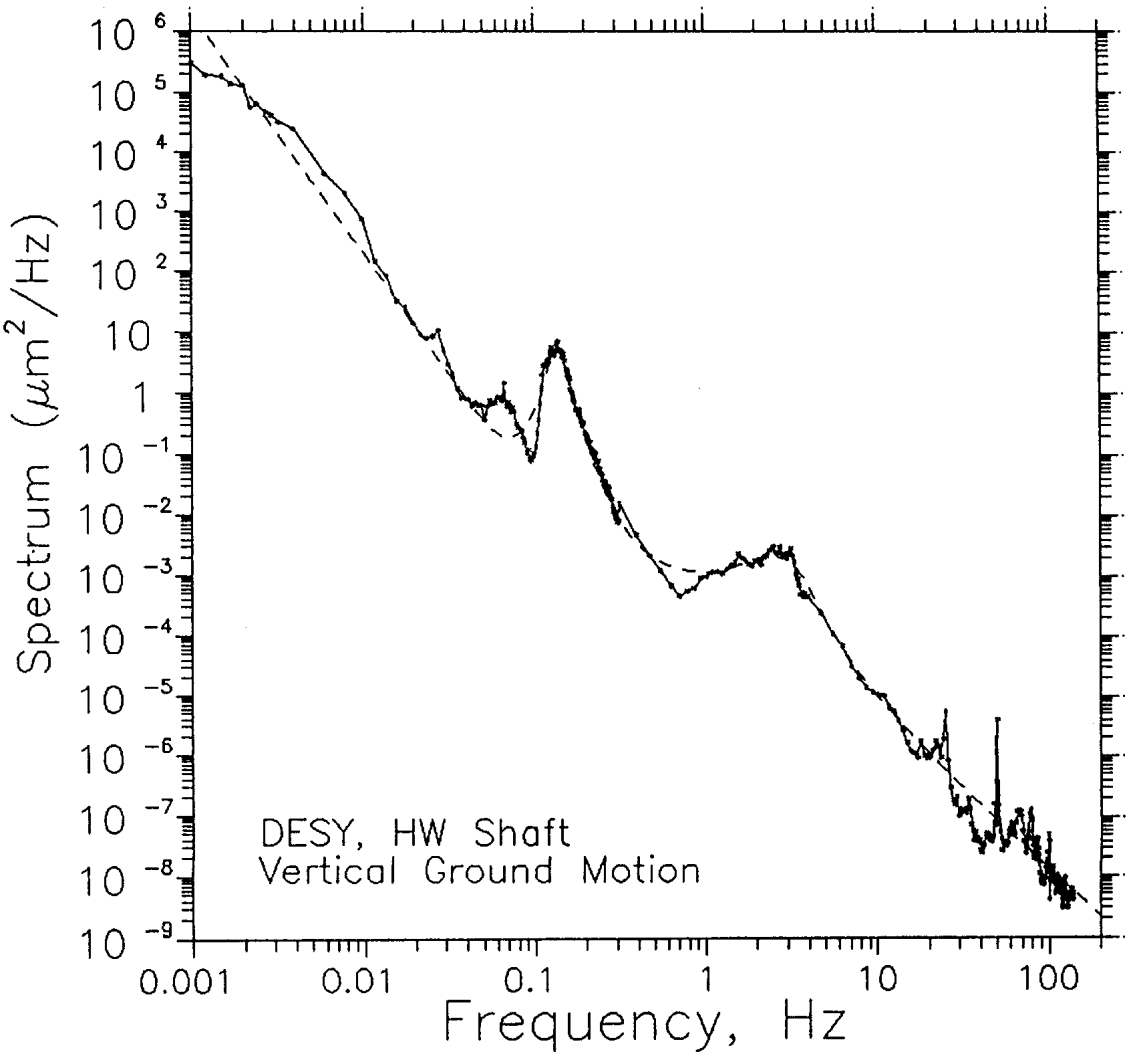

Figure 2.7: Ground motion power spectrum obtained in HERA hall West [Shi 95]. The dashed line shows a fit according to equation (2.42). In order to cover a large frequency range, this spectrum is composed of measurements obtained using both the SM3-KV and the CMG-3T sensors.

$$\Phi(f) \approx \left[\frac{2 \cdot 10^6}{\left(\frac{f}{0.001\,\mathrm{Hz}}\right)^4} + \frac{10^{-3}}{1 + \left(\frac{f}{\mathrm{Hz}}\right)^{\frac{5}{2}}} + \frac{5}{\left(1 + \left(\frac{f - 0.14\,\mathrm{Hz}}{0.14 \cdot 0.14\,\mathrm{Hz}}\right)^2\right)^{\frac{3}{2}}} + \right.$$
$$\left. + \frac{2 \cdot 10^{-3}}{\left(1 + \left(\frac{f - 2.5\,\mathrm{Hz}}{0.45 \cdot 2.5\,\mathrm{Hz}}\right)^2\right)^{\frac{3}{2}}} \right] \frac{\mu\mathrm{m}^2}{\mathrm{Hz}}. \qquad (2.42)$$

This approximation is represented in figure 2.7. The various terms in this fit represent the low frequency motion below 0.1 Hz, the continous part above 1 Hz, the microseismic peak around 1/7 Hz, and the broad 2.5 Hz peak, respectively. Peaks at higher frequencies are not described by this formula due to their artificial origins which depend strongly on the local environment,

for example vacuum pumps, transformers, cooling water, etc.
As shown in figure 2.7, this fit corresponds to a power spectrum density of about $2 \cdot 10^{-9}\,\mu\mathrm{m}^2/\mathrm{Hz}$ at 200 Hz. Assuming $\Phi_{ee}(200\,\mathrm{Hz}) = \Phi_{ss}(200\,\mathrm{Hz})$, we get

$$C_{\max} = (200\,\mathrm{Hz})^2 \cdot 2 \cdot 10^{-9}\,\frac{\mu\mathrm{m}^2}{\mathrm{Hz}} = 8 \cdot 10^{-5}\,\frac{\mu\mathrm{m}^2}{sec}. \tag{2.43}$$

Since drifts described by the ATL rule are also characterized by a power spectrum proportional to f^{-2} (see eqn. (2.29)), these processes also result in similar effects like the noise sources described above. Therefore, we calculate the proportionality constant A in analogy to equation (2.43) and compare it to the value obtained from measurements of closed orbit drifts at HERA [Bri 94]. For a distance $L = 30\,\mathrm{m}$ we get

$$A = \frac{8 \cdot 10^{-5}}{L}\,\frac{\mu\mathrm{m}^2}{\mathrm{sec}} = 2.7 \cdot 10^{-6}\,\frac{\mu\mathrm{m}^2}{\mathrm{m} \cdot \mathrm{sec}}, \tag{2.44}$$

which is consistent with the measured value of $(4 \pm 2) \cdot 10^{-6}\,\frac{\mu\mathrm{m}^2}{\mathrm{Hz}}$. Therefore, if the observed lack of correlation can be explained by an uncorrelated power spectrum proportional to f^{-2}, one cannot decide whether this is caused by uncorrelated ground motion according to the ATL rule or by an additional noise source.
Under the assumption of perfectly correlated ground motion, i. e. $\Phi_{nn} \equiv 0$, the measured coherence $|\gamma_{\mathrm{th}}|$ can be theoretically calculated according to equation (2.38), with Φ_{ss} according to equation (2.42) and $\Phi_{ee} = C_{\max}/f^2$. The resulting coherence is shown in figure 2.8. As this plot shows, the calculated values are higher than those observed at all frequencies, but the general signature is quite close to what has been measured.
Since equation (2.41) may only be valid over a limited band in the frequency range up to 200 Hz, we further increase the proportionality constant C of the additional noise power spectrum Φ_{ee} beyond $C_{\max}$. As shown in figure 2.9, an increased proportionality constant $C = 5 \cdot 10^{-4}\,\mu\mathrm{m}^2/\mathrm{sec}$ would lead to a coherence close to the measured one (see fig. 2.3).
To estimate the effect of slight variations of the noise power spectrum Φ_{ee} as well as the ground motion spectrum Φ_{ss} on the measured coherence $|\gamma_m|$, we compute the variance $\sigma^2_{\gamma_{\mathrm{m}}}$

$$\sigma^2_{\gamma_{\mathrm{m}}} = \left|\frac{\partial|\gamma_m|}{\partial\Phi_{ss}}\right|^2 \cdot \sigma^2_{\Phi_{ss}} + \left|\frac{\partial|\gamma_m|}{\partial\Phi_{ee}}\right|^2 \cdot \sigma^2_{\Phi_{ee}}. \tag{2.45}$$

Figure 2.9 shows the effect of varying ground motion power Φ_{ss} and noise power Φ_{ee} on the measured coherence $|\gamma_m|$. As can be seen, the relative variations σ_{γ_m} of the measured coherence $|\gamma_m|$ increase with decreasing $|\gamma_m|$. A comparison with the measured data presented in figure 2.3 shows that unexpected variations in the coherence, i. e. increasing instead of decreasing coherence with increasing distance between the sensors, indeed occur at frequencies where the measured coherence is quite small, e. g. around 1 Hz.
If we assume that the noise power spectrum Φ_{ee} is purely due to electrical noise on the cables between the sensors and the ADCs, we can estimate the rms value of these disturbances which are required to reproduce the measured coherence. Using $\Phi_{ee} = 5 \cdot 10^{-4}\,\frac{\mu\mathrm{m}^2/\mathrm{sec}}{f^2}$ and with the output sensitivity of the SM3-KV seismometer of $80\,\mathrm{mV}/\mu\mathrm{m\,sec}^{-1}$ (see table 2.2), the corresponding white noise power spectrum Φ_{UU} is computed as

$$\begin{aligned} \Phi_{UU} &= \omega^2 \cdot \Phi_{ee} \cdot \left(80\,\frac{\mathrm{mV}}{\mu\mathrm{m\,sec}^{-1}}\right)^2 \\ &= 128\,\frac{\mathrm{mV}^2}{\mathrm{Hz}}. \end{aligned} \tag{2.46}$$

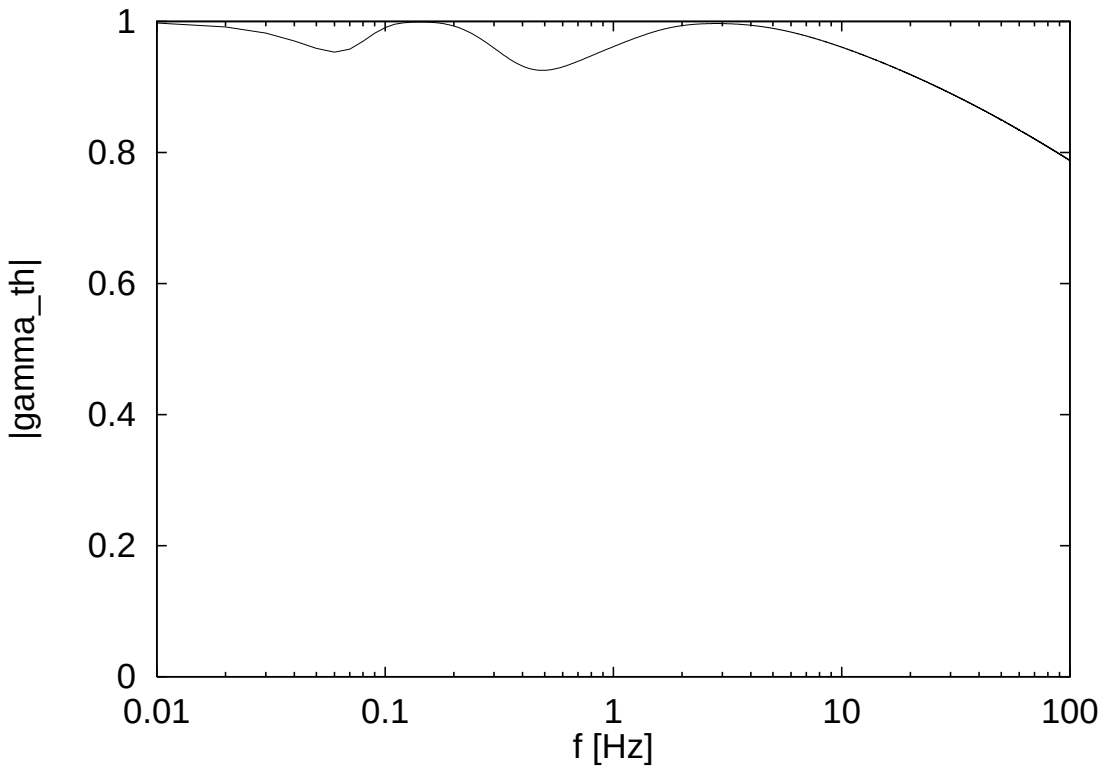

Figure 2.8: Theoretical prediction of the measured coherence $|\gamma_{\text{th}}|$ for a ground motion spectrum Φ_{ss} according to equation (2.42) and noise power spectrum $\Phi_{ee} = C_{\max}/f^2$. The power spectrum Φ_{nn} of uncorrelated ground motion is assumed to be negligible.

Since the power spectrum Φ_{UU} is the Fourier transform of the autocorrelation function of the voltage signal $u(t)$ [Ste 75],

$$\begin{aligned} \Phi_{UU} &= \int_{-\infty}^{\infty} \langle u(t) \cdot u(t+\tau) \rangle \exp(-i\omega\tau)\,\mathrm{d}\tau \\ &= \int_{-\infty}^{\infty} \sigma_u^2 \delta(\tau)\,\mathrm{d}\tau \\ &= \sigma_u^2\,\mathrm{sec}, \end{aligned} \tag{2.47}$$

the required rms value is about $\sigma_u = 11.3\,\mathrm{mV}$ for the electrical noise signals on the cables. Since coaxial cables were used, this seems to be quite unlikely.
To exclude such effects, digital instead of analog data transfer from the seismometers to the computer could help to overcome problems with electric noise.
The effects of (local) air pressure variations are difficult to estimate. The sensors are equipped with a sealed housing, so variations in air pressure cannot act directly on the seismic masses by effects such as buoyancy. On the other hand, air pressure fluctuations lead to real ground motion.
To estimate the air pressure power spectrum corresponding to the required noise power spectrum Φ_{ee}, we calculate the bending Δx of the earth's surface due to air pressure:

$$\Delta x = \frac{p \cdot l}{E}, \tag{2.48}$$

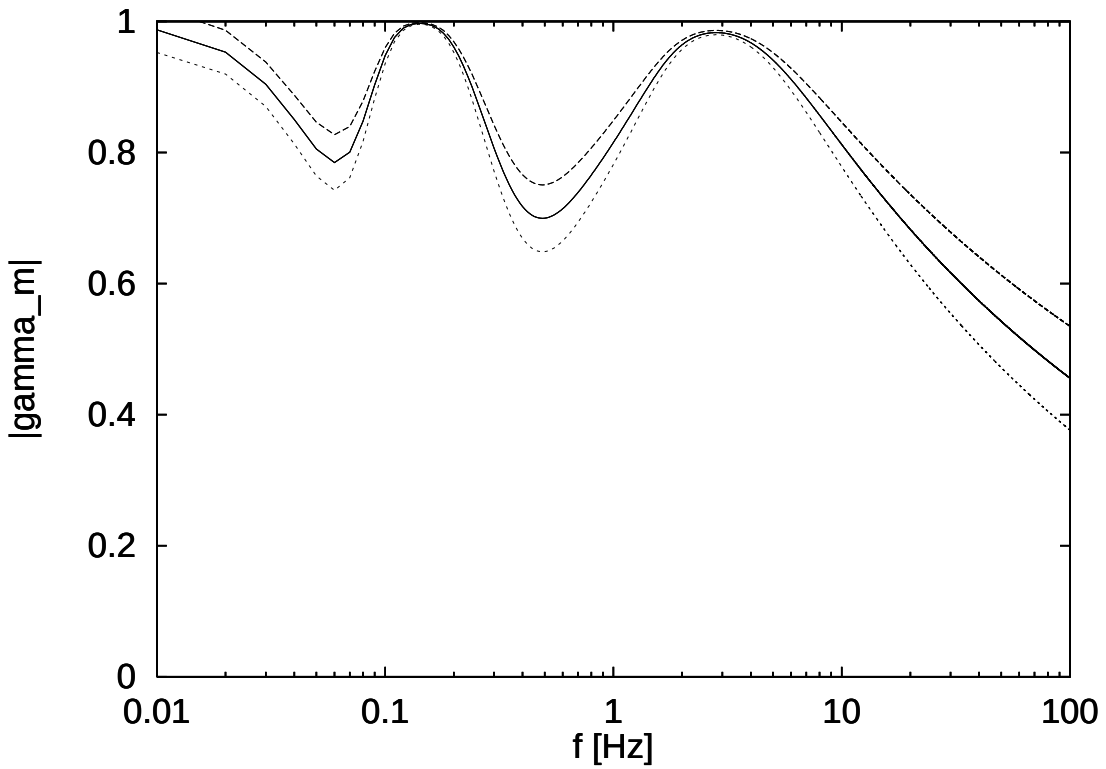

Figure 2.9: Theoretically calculated coherence $|\gamma_m|$ for a ground motion spectrum Φ_{ss} according to equation (2.42) and an additional noise power spectrum $\Phi_{ee} = C/f^2$, for $C = 5 \cdot 10^{-4}\,\mu\text{m}^2/\text{sec}$ (solid line). The dashed lines represent "error bars" according to equation (2.45), with $\sigma_{\Phi_{ss}} = 0.2 \cdot \Phi_{ss}$ and $\sigma_{\Phi_{ee}} = 0.2 \cdot \Phi_{ee}$. The power spectrum Φ_{nn} of uncorrelated ground motion is assumed to be zero.

where p is the air pressure, l is the effective depth of the bent surface layer and E is the ground's Young's modulus. In this estimation, we use the Young's modulus of soft soil because the HERA halls are built on sand. Thus, the hall is assumed to move as a whole when the air pressure varies. With $l \approx 1\,\text{m}$, $E = 3 \cdot 10^9\,\text{N/m}^2$ and $p = 1000\,\text{mbar} = 10^5\,\text{N/m}^2$, we get

$$\Delta x = \frac{10^5\,\frac{\text{N}}{\text{m}^2} \cdot 1\,\text{m}}{3 \cdot 10^9\,\frac{\text{N}}{\text{m}^2}} = 33\,\mu\text{m}. \tag{2.49}$$

Using this result, the power spectrum Φ_{pp} of uncorrelated air pressure fluctuations becomes

$$\begin{aligned} \Phi_{pp} &= \Phi_{ee} \cdot \frac{1}{33^2}\,\frac{\text{bar}^2}{\mu\text{m}^2} \\ &= 4.6 \cdot 10^{-7}\,\frac{\frac{\text{bar}^2}{\text{sec}}}{f^2}. \end{aligned} \tag{2.50}$$

During the measurements, the sensors are placed on the floor of HERA hall West, which is made of concrete. This floor might be compressed due to air pressure. Since the Young's modulus E of concrete is about a factor of 10 larger than the value used in this estimate [Ric 96] the

obtained result is quite conservative. Calculating the rms air pressure fluctuation σ_p in the frequency range from 1 Hz to infinity we get

$$\sigma_p(f > 1\,\mathrm{Hz}) = \sqrt{\int_{1\,\mathrm{Hz}}^{\infty} \Phi_{pp}\,\mathrm{d}f} = 6.8 \cdot 10^{-4}\,\mathrm{bar}. \tag{2.51}$$

An air pressure fluctuation of 0.7mbar rms at 1 Hz (or, correspondingly, 7 mbar at 0.01 Hz) is very unlikely and could be easily detected by a barometer.
Temperature variations lead to air convection inside the sealed seismometer housing. This could lead to motion of the seismic mass and therefore to errors in the measurements, but this effect is hard to quantify.
To suppress artefacts due to temperature variations or due to air flow, an increased measuring time to get better statistics and/or simultaneous measurements at different distances should be considered. Additionally, the sensors should be carefully shielded and insulated.
Figure 2.10 [Shi 95] shows a comparison of the spectrum measured at HERA hall West with data taken at several other high energy physics laboratories, namely KEK (Tsukuba, Japan) [Oga 92], SSC (Waxahachie, Texas, USA) [Par 93], VEPP-3 (Novosibirsk, Russia) [Leb 92] and UNK (Protvino, Russia) [Bak 91a, Bak 93]. While all spectra show the same general

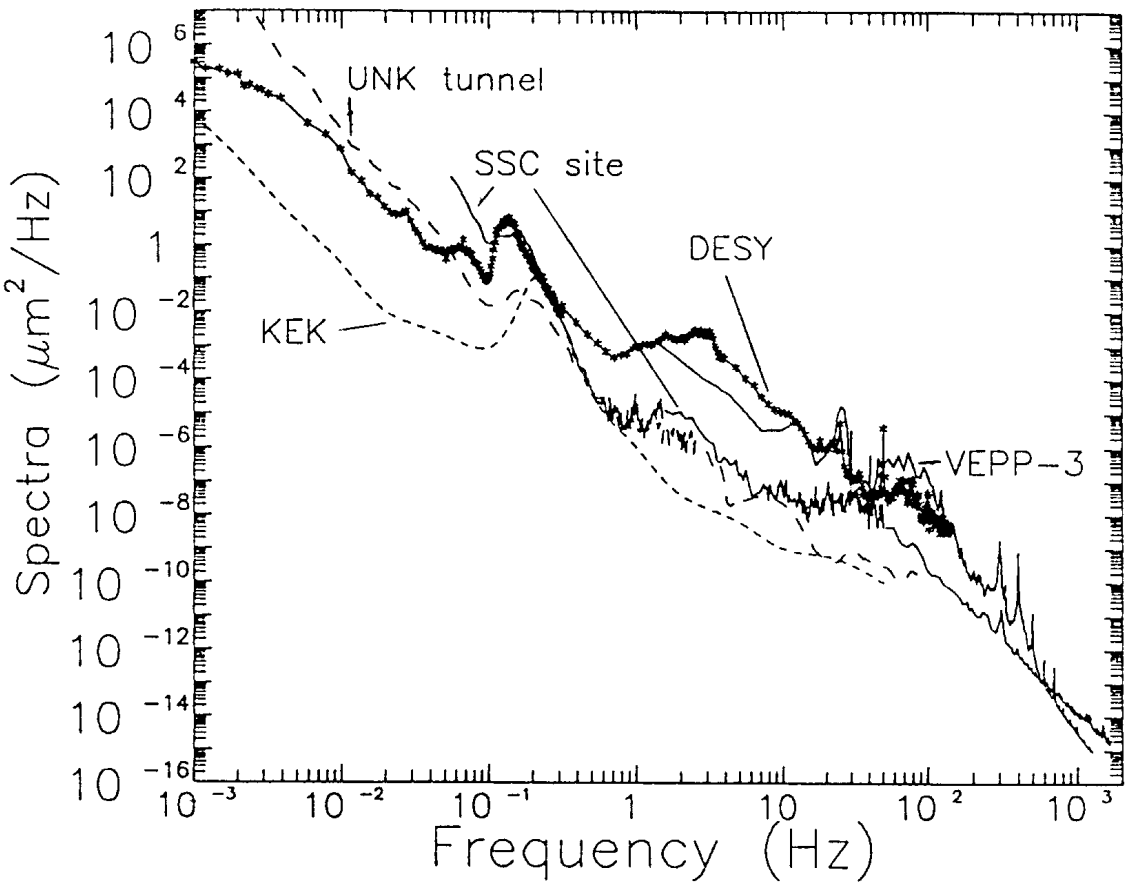

Figure 2.10: Comparison of the spectrum measured at HERA with data obtained at KEK (Tsukuba, Japan), SSC (Waxahachie, Texas, USA), VEPP-3 (Novosibirsk, Russia) and UNK (Protvino, Russia) [Shi 95].

$1/\omega^4$-tendency and the microseismic peak, they differ significantly in the high-frequency regime between approximately 1 Hz and 100 Hz, where cultural noise dominates. The spectrum measured in the VEPP-3 tunnel, as well as that one taken at HERA, was obtained while the storage ring was under operation. These spectra are quite similar, while the data taken at KEK and SSC show significantly less contribution in the 1-100 Hz regime since they were measured far from any artificial sources of vibration.
To determine the validity of the ATL rule and to measure the proportionality constant A, magnet motion in the FFTB tunnel at SLAC was monitored with the wire alignment system [Ass 96]. The electronic noise of the wire monitors can be estimated as the signal detected by monitors mounted on neighbouring quadrupoles since it is plausible to assume that practically no relative motion of these magnets with respect to each other occurs there. Fig. 2.11 shows the spectrum of uncorrelated vertical motion of two quadrupoles separated by approximately 70 cm. Since these two magnets are not located in exactly the same position, this measured

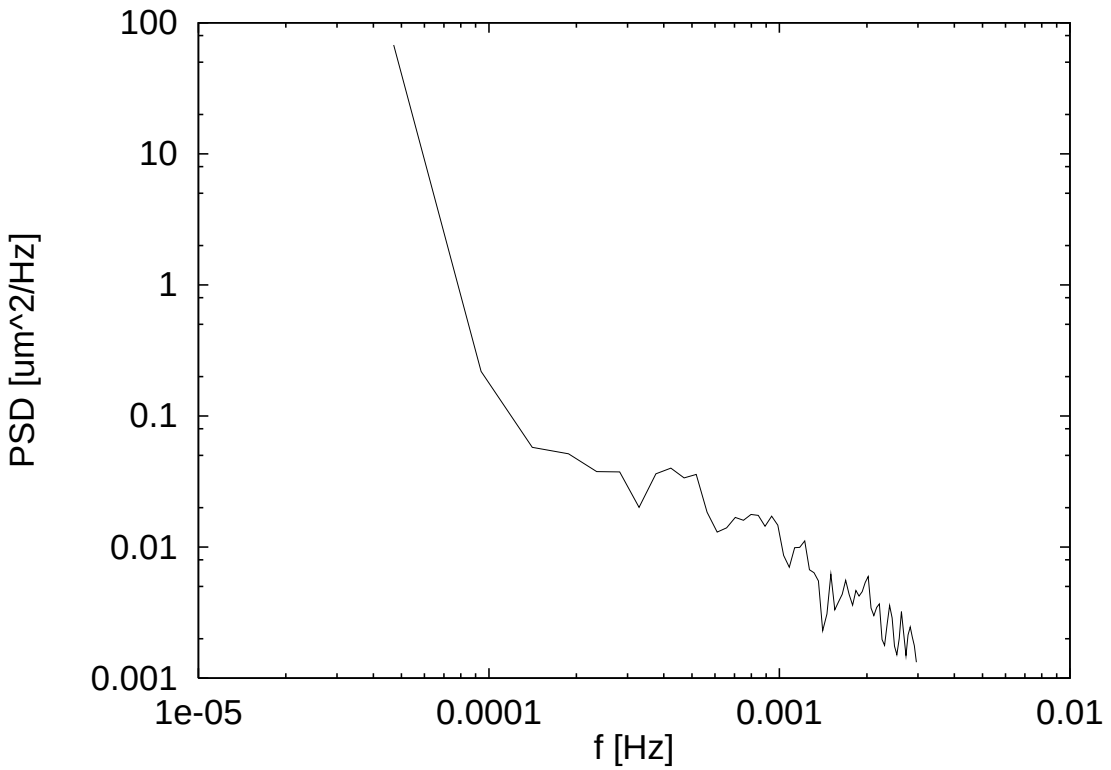

Figure 2.11: Spectrum of uncorrelated motion of two neighbouring magnets, reflecting the electronic noise of the wire position monitors.

spectrum is a slight overestimation of the effect of electronic noise, because some real uncorrelated motion might be present. Possible sources of this are not only motion of the magnets themselves, but also of the wire terminators which are located at slightly different distances from the magnets.
To determine the proportionality constant A of the ATL rule, motion signals of two magnets located at approximately one third of the total wire length L_{tot} (see fig. 2.12) were processed. The resulting power spectrum Φ_{nn} of uncorrelated motion is shown in figure 2.13. As mentioned

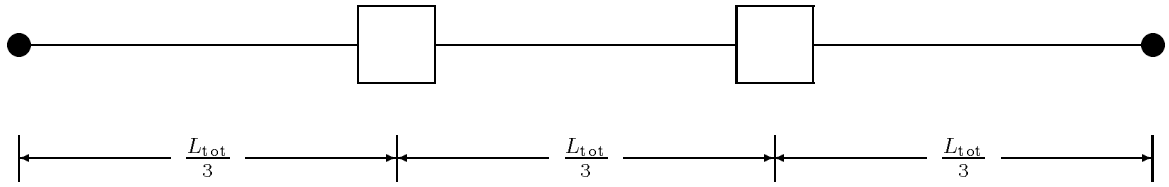

Figure 2.12: Location of magnets used for ATL investigations. $L_{\rm tot} \approx 39.5\,\mathrm{m}$. Since the magnets in the FFTB tunnel are not located exactly as indicated here, the distance L used for determining the proportionality constant A of the ATL rule was conservatively estimated at $L = 10\,\mathrm{m}$.

above, the ATL rule corresponds to a power spectrum $\rho(\omega, L)$ of uncorrelated relative motion of two points described by (eqn. (2.29))

$$\rho(\omega, L) = \frac{A \cdot L}{\omega^2}. \tag{2.52}$$

A fit is indicated in fig. 2.13 by the straight line. Since the monitors used in these investigations are not located at exactly the positions indicated in figure 2.12, a distance $L = L_{\rm tot}/3 = 10\,\mathrm{m}$ was used. This fit corresponds to a proportionality constant of the ATL rule of

$$\begin{aligned} A &= \frac{\Phi_{nn}(\omega) \cdot \omega^2}{10\,\mathrm{m}} \\ &= (2 \pm 1) \cdot 10^{-8}\, \frac{\mu\mathrm{m}^2}{\mathrm{m} \cdot \mathrm{sec}}. \end{aligned} \tag{2.53}$$

This value is about two orders of magnitude smaller than the value $A = (4 \pm 2) \cdot 10^{-6}\, \frac{\mu\mathrm{m}^2}{\mathrm{m}\cdot\mathrm{sec}}$ obtained from closed orbit measurements at the ep collider HERA [Bri 94]. This indicates that this "constant" strongly depends on site geology (type of ground) or that the HERA measurements include other sources of orbit motion.
This result might be not surprising taking into account the fact that the HERA tunnel is built on sand and is partially covered by ground water with varying water level, while SLAC is built on a rather rocky site.

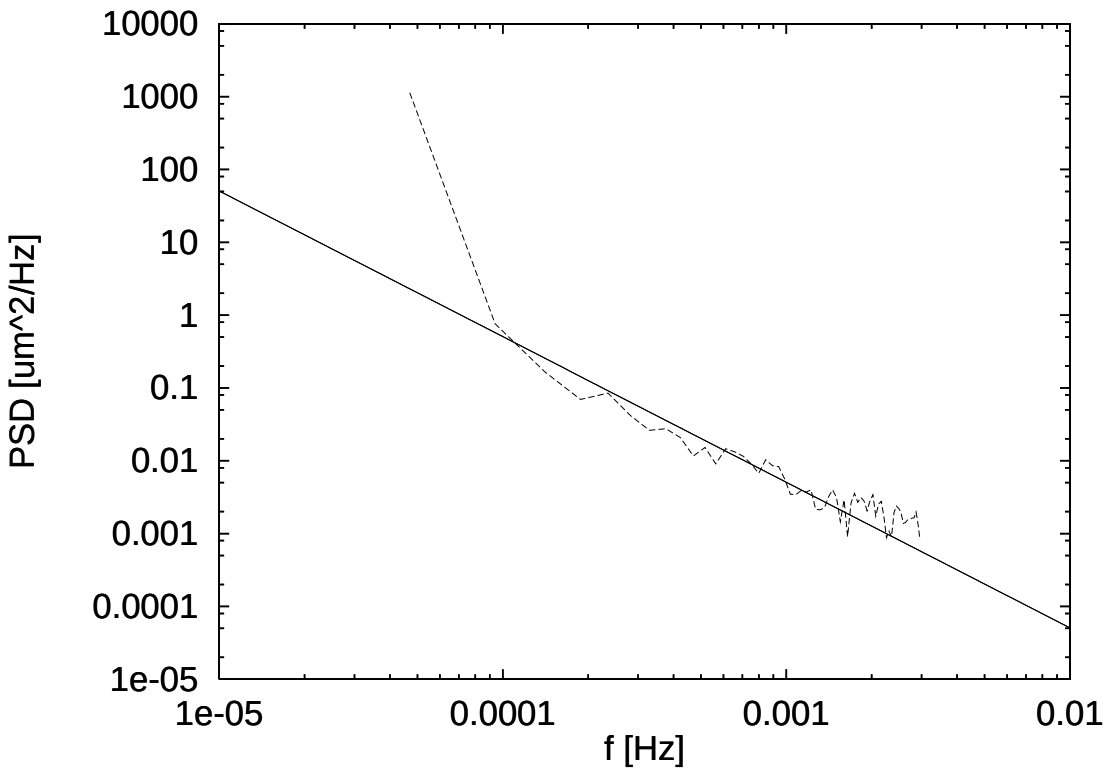

Figure 2.13: Spectrum of uncorrelated vertical magnet motion obtained in section 2 of the Final Focus Test Beam at SLAC [Ass 96]. The straight line corresponds to an ATL-like spectrum with proportionality constant $A = 2 \cdot 10^{-8}\,\mu\mathrm{m}/(\mathrm{m} \cdot \mathrm{sec})$ and distance $L = 10\,\mathrm{m}$.

3 Support concept

For compensation purposes the ground motion spectrum can be divided into various frequency domains, each of them requiring different compensation schemes [Mon 95].
As the experience at SLAC has shown, beam-based orbit correction schemes can be successfully employed only in the low frequency region where $f < f_{\mathrm{rep}}/25 = 2\,\mathrm{Hz}$ [Min 95]. Above this frequency limit the compensation capability of any beam-based method is not sufficient, and may even lead to an amplification of the beam jitter at higher frequencies. To decrease beam jitter amplitudes at frequencies beyond 2 Hz it is necessary to fight beam jitter at its source. For this purpose the linear collider quadrupole vibrations have to be either passively damped or measured independently of the beam and compensated by some means.
The simplest passive damping system consists of some kind of "spring" with resonance frequency f_r and damping constant k acting as magnet support, shown schematically in fig. 3.1. The force

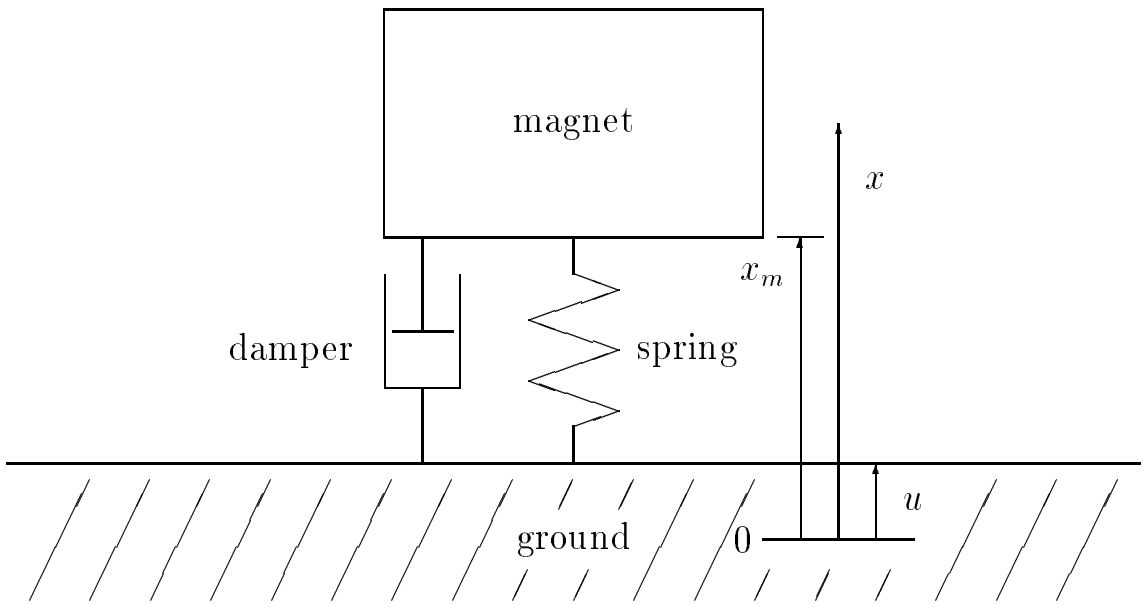

Figure 3.1: Schematic view of a passive damping system, consisting of a spring supporting the magnet.

due to compression and expansion of the spring is proportional to its length $L = x_m - u$, thus

$$F_{\mathrm{spring}} = -D(x_m - u), \tag{3.1}$$

where D is the spring constant.
Since the damping force is proportional to the relative velocity $v_{\mathrm{rel}} = \frac{\mathrm{d}}{\mathrm{d}t}(x_m - u)$ of the magnet with respect to the ground, we get

$$F_{\mathrm{damping}} = -k\,\frac{\mathrm{d}}{\mathrm{d}t}(x_m - u). \tag{3.2}$$

With

$$m\frac{\mathrm{d}^2}{\mathrm{d}t^2}x_m = F_{\mathrm{damping}} + F_{\mathrm{spring}}, \tag{3.3}$$

we get the following differential equation of this damped oscillator:

$$m\ddot{x}_m + k(\dot{x}_m - \dot{u}) + D(x_m - u) = 0. \tag{3.4}$$

Here, m, k and D are the magnet mass, the damping constant and the spring constant, respectively.
Application of the Laplace transformation (see Appendix B.1) to this differential equation leads to

$$\begin{aligned} & m \cdot s^2 X_m(s) + k \cdot s(X_m(s) - U(s)) + D(X_m(s) - U(s)) &= 0 & (3.5)\\ \Leftrightarrow \quad & s^2 X_m(s) + 2\delta\omega_r s(X_m(s) - U(s)) + \omega_r^2(X_m(s) - U(s)) &= 0 & (3.6)\\ \Leftrightarrow \quad & X_m(s) = \frac{\omega_r^2 + 2\delta\omega_r s}{s^2 + 2\delta\omega_r s + \omega_r^2} \cdot U(s) &= H_r(s) \cdot U(s). & (3.7) \end{aligned}$$

Here, $X_m(s)$ and $U(s)$ denote the Laplace transforms of $x_m(t)$ and $u(t)$, respectively, while

$$H_r(s) = \frac{\omega_r^2 + 2\delta\omega_r s}{s^2 + 2\delta\omega_r s + \omega_r^2} \tag{3.8}$$

is the transfer function of this passive vibration absorber with resonance frequency $f_r = \omega_r/2\pi = \sqrt{D/m}/2\pi$.
According to this transfer function a passive vibration absorber attenuates vibration amplitudes by a factor proportional to $1/\omega^2$ at frequencies between the resonance frequency ω_r and approximately ω_r/δ, while for higher frequencies the attenuation is proportional to $1/\omega$ (see fig. 3.2).
The repetition rate f_{rep} of the SBLC is 50 Hz, therefore the limiting frequency for beam-based orbit correction schemes is some 2 Hz. In this case a passive quadrupole support with a resonance frequency f_r of approximately 1 Hz is required to achieve an attenuation by a factor of 5 at 2 Hz. If one assumes a magnet mass of 100 kg, this corresponds to a spring constant D of $4000\,\mathrm{N \cdot m^{-1}}$.
Though such a system would provide sufficient damping of ground motion above its resonance frequency it would be very sensitive to any force acting on the magnet directly. The ratio of the resulting amplitude per input force is often referred to as the compliance of the system. For example a static force as small as $4 \cdot 10^{-3}$N would lead to a static magnet displacement of 1μm.
In the case of a force $f(t)$ acting on the magnet directly the differential equation for the resulting quadrupole motion $x_m(t)$ becomes ($u(t) \equiv 0$)

$$\begin{aligned} & m\ddot{x}_m &= f - k\dot{x}_m - Dx_m & (3.9)\\ \Leftrightarrow \quad & \ddot{x}_m + 2\delta\omega_r\dot{x}_m + \omega_r^2 x_m &= \frac{f}{m} = \frac{\omega_r^2}{D} f. & (3.10) \end{aligned}$$

Note that in these equations $f = f(t)$ denotes a force rather than a frequency.
In the frequency domain the excitation amplitude $X_m(s)$ resulting from an input force $F(s)$ as function of the Laplace variable s can therefore be written as

$$X_m(s) = \frac{\frac{\omega_r^2}{D}}{s^2 + 2\delta\omega_r s + \omega_r^2} \cdot F(s). \tag{3.11}$$

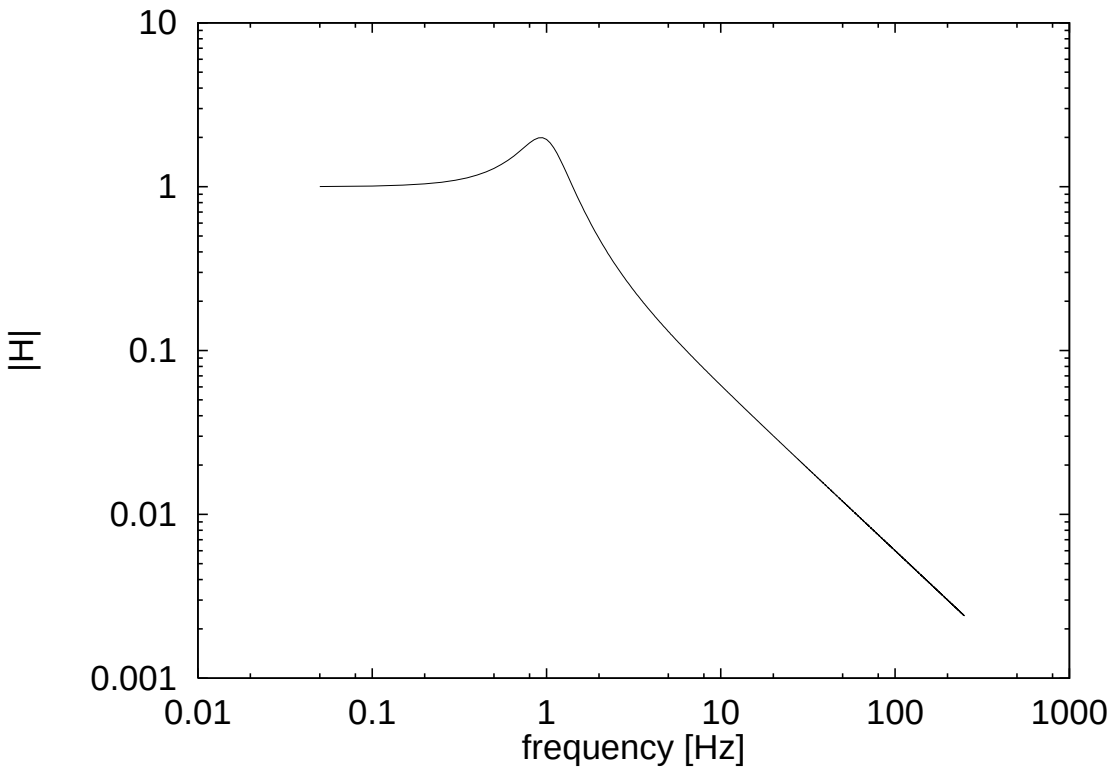

Figure 3.2: Amplitude of the transfer function H_r of a passive vibration absorber, according to equation (3.8), with damping coefficient $\delta = 0.3$ and resonance frequency $f_r = 1\,\mathrm{Hz}$.

Here $X_m(s)$ and $F(s)$ are the Laplace transforms of $x_m(t)$ and $f(t)$, respectively.
Using $s = i\omega = i \cdot 2\pi f$ figure 3.3 shows the modulus of this transfer function for forces acting on the magnet directly and resulting in vibration amplitudes, for example coil vibrations due to cooling water pressure fluctuations or air motion caused by air conditioning systems installed in the linac tunnel, for the resonance frequencies $f_r = 1\,\mathrm{Hz}$, $10\,\mathrm{Hz}$ and $100\,\mathrm{Hz}$.

To quantify this we estimate the effect of air flow with velocity v acting on a magnet with cross section A. The resulting force can be calculated as

$$F = \frac{1}{2} c_w \rho A v^2, \tag{3.12}$$

with $\rho = 1.3\,\mathrm{kg/m^3}$ being the density of air. Here we assume the drag coefficient c_w of the quadrupole to be unity.
For a magnet cross section A of $0.04\,\mathrm{m^2}$ the tolerable air velocity v leading to a magnet motion of 50 nm (i. e. the tolerable quadrupole jitter level) yields

$$v = \sqrt{\frac{2 \cdot F}{c_w \rho \cdot A}} = \sqrt{\frac{2 \cdot 2 \cdot 10^{-4}}{1 \cdot 1.3 \cdot 0.04}}\,\frac{\mathrm{m}}{\mathrm{sec}} = 0.09\,\frac{\mathrm{m}}{\mathrm{sec}}. \tag{3.13}$$

This very low air velocity is likely to be exceeded by any air conditioning system.
These considerations led to the development of an active stabilization system with a vibration sensor on top of each magnet and an actuator to counteract ground motion in order to keep the magnet at rest.
A critical decision is the choice of the mechanical resonance frequency of the active support.

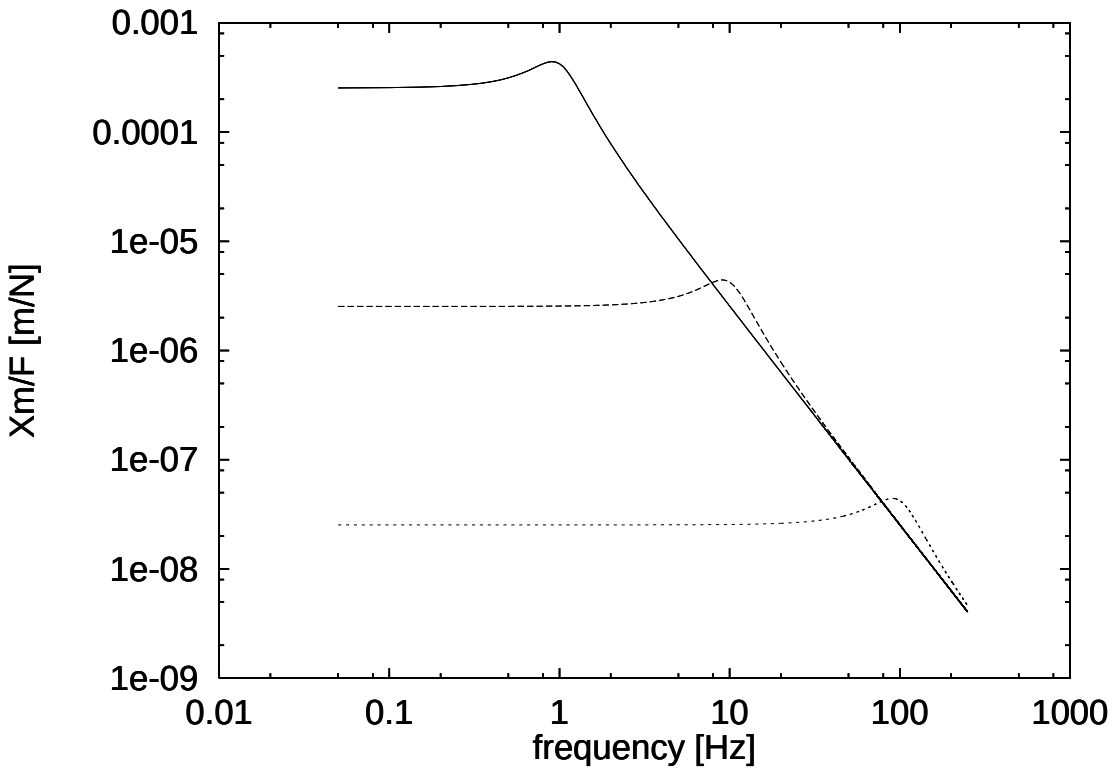

Figure 3.3: Transfer function for frequency dependent forces acting on the magnet itself and resulting in displacement $X_m(f)$ according to equation (3.11) with $m = 100\,\mathrm{kg}$ and $\delta = 0.3$ for three different resonance frequencies $f_r = 1\,\mathrm{Hz}$ (solid), $10\,\mathrm{Hz}$ (broken) and $100\,\mathrm{Hz}$ (dashed).

One possibility is an intermediate frequency of about $f_r = 10\,\mathrm{Hz}$ which would lead to passive attenuation of higher frequencies while slow vibrations would be compensated actively using for example an electrodynamic transducer. Assuming a motion sensor with a lower frequency limit f_s and transfer function H_s, together with the transfer function H_r of the support

$$H_r = \frac{\omega_r^2 + 2\delta\omega_r s}{s^2 + 2\delta\omega_r s + \omega_r^2} \tag{3.14}$$

and a feedback algorithm $R(s)$, one gets the transfer function

$$H_g(s) = \frac{H_r(s)}{1 + R(s)H_r(s)H_s(s)}, \tag{3.15}$$

which describes the transfer of ground motion amplitudes to the magnet (see Appendix C). On the other hand the transfer function for excitation forces acting on the magnet directly becomes

$$H_m(s) = \frac{\frac{1}{D}}{1 + R(s)H_r(s)H_s(s)}. \tag{3.16}$$

Since $\lim_{s\to 0} H_s(s) = 0$ due to the finite lower frequency limit f_s and $\lim_{s\to\infty} H_r(s) = 0$ (eq. (3.14)),

$$\lim_{s\to 0} H_m(s) = \lim_{s\to\infty} H_m(s) = \frac{1}{D}. \tag{3.17}$$

Thus the effective spring constant H_m^{-1} in the limit of low and high frequencies equals the passive spring constant D of the magnet support. Therefore the mechanical resonance frequency and correspondingly the spring constant of the support should be chosen as high as possible, but at least that high that any possible forces acting on the magnet directly, like air flow or cooling water pressure fluctuations, lead to magnet motion below the desired tolerance level.
Another possibility is a system based on correction magnets to compensate the quadrupole jitter induced beam motion. A parallel displacement of a quadrupole magnet of length l_{quad} with respect to the design orbit leads to an additional integrated dipole field $b_{\mathrm{quad}}(t) \cdot l_{\mathrm{quad}}$ on the design orbit. Here $b_{\mathrm{quad}}(t)$ is the time dependent additional dipole field produced by the displaced quadrupole. This integrated field is proportional to the displacement $u(t)$ of the magnet with the proportionality constant being the field gradient $g = \partial B_x/\partial y$. This can be compensated by a dipole magnet which is preferably mounted inside the quadrupole. For simplicity it is assumed here that the length of the dipole corrector equals the length l_{quad} of the quadrupole magnet. The magnetic field of the dipole corrector is adjusted such that it compensates the additional dipole field of the quadrupole. Therefore the integrated field of the dipole corrector is also proportional to the displacement of the quadrupole, with the same proportionality constant g. Denoting $H(s)$ as the transfer function of the correction path consisting of the motion sensor on top of each quadrupole and several amplifiers, the applied correction field is $B(s) = g \cdot H(s)$. Here $B(s)$ is the Laplace transform of the magnetic field $b(t)$. The magnetic field $\delta B(s)$ that remains after correction as a function of the quadrupole motion $U(s)$ is therefore

$$\begin{aligned} \delta B(s) &= g \cdot U(s) - g \cdot H(s) \cdot U(s) \\ &= (1 - H(s)) \cdot g \cdot U(s) \\ &= G(s) \cdot U(s). \end{aligned} \tag{3.18}$$

Here $\delta B(s)$ and $U(s)$ are the Laplace transforms of the remaining magnetic field $\delta B(t)$ and of the quadrupole motion $u(t)$, respectively.
To suppress beam jitter effectively the condition $|G(s)| \approx 0$ has to be fulfilled. Therefore the conditions $|H(s)| \approx 1$ and $\arg(H(s)) \approx 0$ are required over the relevant frequency range.
To fulfill these conditions a sensor with vanishing phase shift and constant amplitude transfer function for frequencies higher than 2 Hz is necessary. A reasonable upper frequency limit is given by the frequency where the rms ground motion jitter becomes negligible. To achieve a practically constant transfer function $H_{\mathrm{sensor}}(s)$ of the sensor with $\arg(H_{\mathrm{sensor}}(s)) \approx 0$ for frequencies down to 2 Hz its resonance frequency must be well below 2 Hz. These requirements can only be fulfilled by seismometers with internal feedback systems (see Section 4). Usually these instruments are quite expensive.
In the case of an active mechanical stabilization system the requirements on the transfer function of the motion sensor are more relaxed (see Appendix C) because, in contrast to the dipole corrector scheme, it employs a closed instead of an open loop.

4 Vibration sensors

In any active stabilization system the vibration sensor is the most critical component, while piezo actuators and high voltage amplifiers are standard devices. Obviously the sensor must be capable of measuring at high accuracy vibrations within the frequency range of ground motion to be suppressed. The internal noise level of the sensor has to be well below the desired residual vibration level of the active stabilization system. Additionally the phase shift within the desired feedback bandwidth should be limited to $\pm\pi$ to fulfill the stability criterion (see Appendix D). These requirements can be fulfilled by electrodynamical geophones. These devices consist of a coil suspended on a spring within the field of a permanent magnet (see fig. 4.1). The voltage

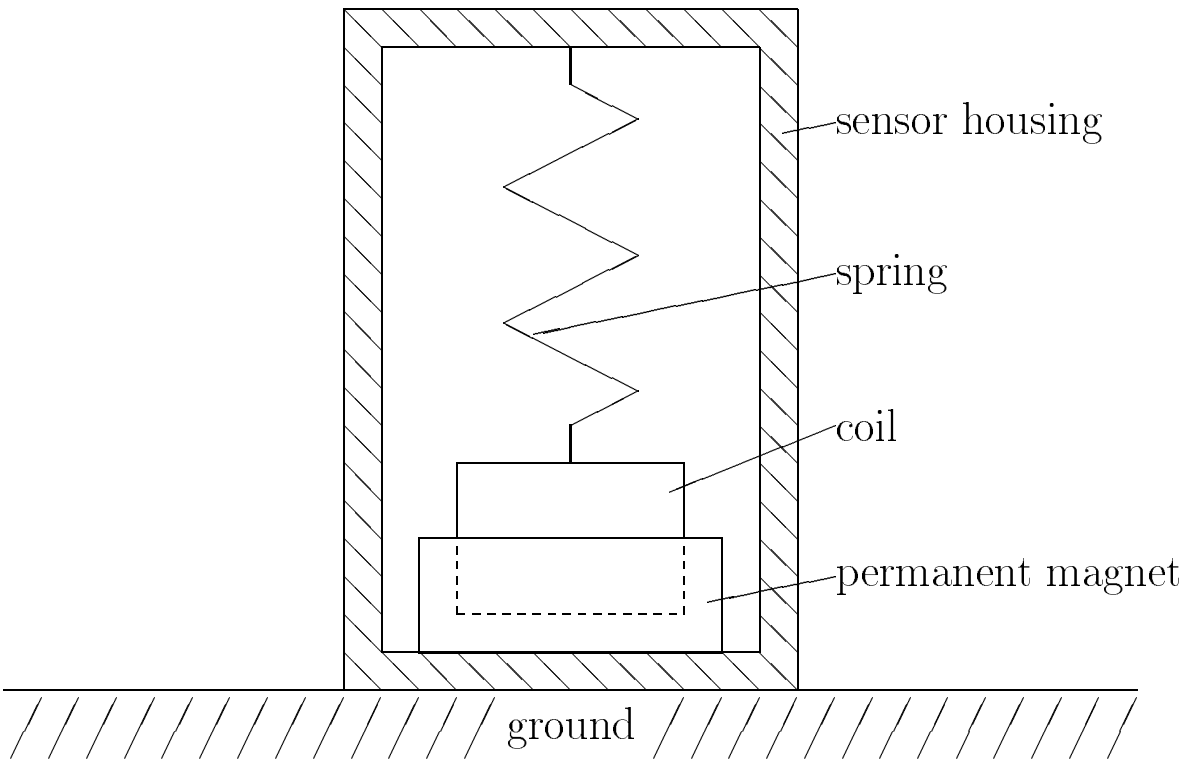

Figure 4.1: Schematic view of a geophone type vibration sensor.

induced in the coil is proportional to the velocity of the coil with respect to the permanent magnet.
The transfer function of such a sensor can be easily calculated. As derived in Section 3, the transfer function describing the motion $X_m(s)$ of the mass due to ground motion $U(s)$ is (eqn. (3.8))

$$H(s) = \frac{\omega_r^2 + 2\delta\omega_r s}{s^2 + 2\delta\omega_r s + \omega_r^2}, \tag{4.1}$$

with ω_r and δ being the resonance frequency and the damping coefficient of the system, respectively. s is the Laplace variable.
While this transfer function describes the motion of the mass relative to an inertial frame of reference, the primary output signal of an electrodynamical geophone is proportional to the velocity of the mass with respect to the ground. The relative position $X_m(s) - U(s)$ as a function

of the ground motion signal $U(s)$ can be written

$$\begin{aligned} X_m(s) - U(s) &= H(s) \cdot U(s) - U(s) \\ &= \left[\frac{\omega_r^2 + 2\delta\omega_r s}{s^2 + 2\delta\omega_r s + \omega_r^2} - 1 \right] U(s) \\ &= -\frac{s^2}{s^2 + 2\delta\omega_r s + \omega_r^2} U(s). \end{aligned} \tag{4.2}$$

Here $X_m(s)$ and $U(s)$ denote the Laplace transforms of $x_m(t)$ and $u(t)$.
Such a sensor is capable of measuring with high accuracy vibrations at frequencies beyond the mechanical resonance frequency of the spring, while frequencies below this limit are hardly detected, as can be seen from the transfer function

$$H(s) = -\frac{s^2}{s^2 + 2\delta\omega_r s + \omega_r^2} \tag{4.3}$$

which vanishes for $s = i\omega \to 0$. To ensure significant sensitivity of a geophone sensor at frequencies far below 2 Hz, the mechanical resonance frequency of the coil suspended on the spring should therefore be chosen as low as possible. Unfortunately this leads to large dimensions of the sensors.
To overcome this modern seismometers, like those used for the ground motion measurements presented in Section 2, are equipped with internal feedback loops which stabilize the position of the coil with respect to the sensor housing and the permanent magnet. The transfer function of the purely mechanical part,

$$H_m(s) = -\frac{s^2}{s^2 + 2\delta\omega_r s + \omega_r^2}, \tag{4.4}$$

is then modified by this feedback to

$$H_f(s) = -\frac{s^2}{s^2 + 2\Delta\Omega_r s + \Omega_r^2}, \tag{4.5}$$

with $\Omega_r < \omega_r$ and Δ being the resonance frequency and the damping coefficient of the desired transfer function H_f. To compute this we calculate the transfer function of the closed feedback loop with a PID controller (see Appendices B.1 and C):

$$\begin{aligned} H_l(s) &= \frac{H_m(s)}{1 + (P + \frac{I}{s} + Ds) H_m(s)} \\ &= -\frac{s^2}{s^2 + 2\delta\omega_r s + \omega_r^2 - (P + \frac{I}{s} + Ds)s^2} \\ &= -\frac{s^2}{(1-P)s^2 + (2\delta\omega_r - I)s + \omega_r^2 - Ds^3} \\ &= -\frac{s^2/(1-P)}{s^2 + \frac{2\delta\omega_r - I}{1-P} s + \frac{\omega_r^2}{1-P} + \frac{D}{1-P} s^3}. \end{aligned} \tag{4.6}$$

The parameters P, I and D can be obtained by comparing eqns. (4.5) and (4.6),

$$P = 1 - \frac{\omega_r^2}{\Omega_r^2}, \tag{4.7}$$

$$I = 2\delta\omega_r - 2\Delta\frac{\omega_r^2}{\Omega_r}, \tag{4.8}$$

$$D = 0, \tag{4.9}$$

resulting in a PI feedback. In other words, a signal composed of the sum of signals proportional to the relative displacement of the sensor mass with respect to the housing and its time integral is fed back to stabilize the mass position. This method is limited only by the electronics noise of the feedback circuit, and extremely long periods can be achieved. In the case of the CMG-3T seismometer made by Guralp Systems Ltd. for example, the mechanical resonance frequency of 2 Hz is modified to 0.00277 Hz [Gur 93].
A third type of vibration sensors are piezoelectric accelerometers. These devices consist of a piezo crystal mounted to the sensor housing at one side, while a seismic mass is fixed to the opposite side. Therefore the piezo crystal acts as a spring connecting the sensor housing and the seismic mass. An acceleration of the sensor in the sensitive direction leads to a shearing force inside the crystal. The piezo voltage induced in the crystal is proportional to the shearing force and therefore to the acceleration of the probe.
The resonance frequency of the crystals is very high. Therefore accelerometers are operated far below their resonance frequency. This fact makes it extremely difficult to measure vibrations of very low frequency with sufficient accuracy. As measurements of the sensitivity have shown, they are not applicable in the active stabilization system because the internal noise level of their low-noise preamplifiers corresponds to displacements larger than the required magnet motion tolerances.
The noise of geophone type vibration sensors has been studied to determine their applicability in the active stabilization system [Mon 94].
This measurement is not trivial because it is very difficult to provide a perfectly quiet environment as a noise-free reference. Instead, two sensors of the same type are placed side-by-side, so both of them measure the same ground motion signal, as schematically shown in figure 4.2 [Ste 79]. The output signals $x(t)$ and $y(t)$ of both sensors with transfer functions H_1 and H_2

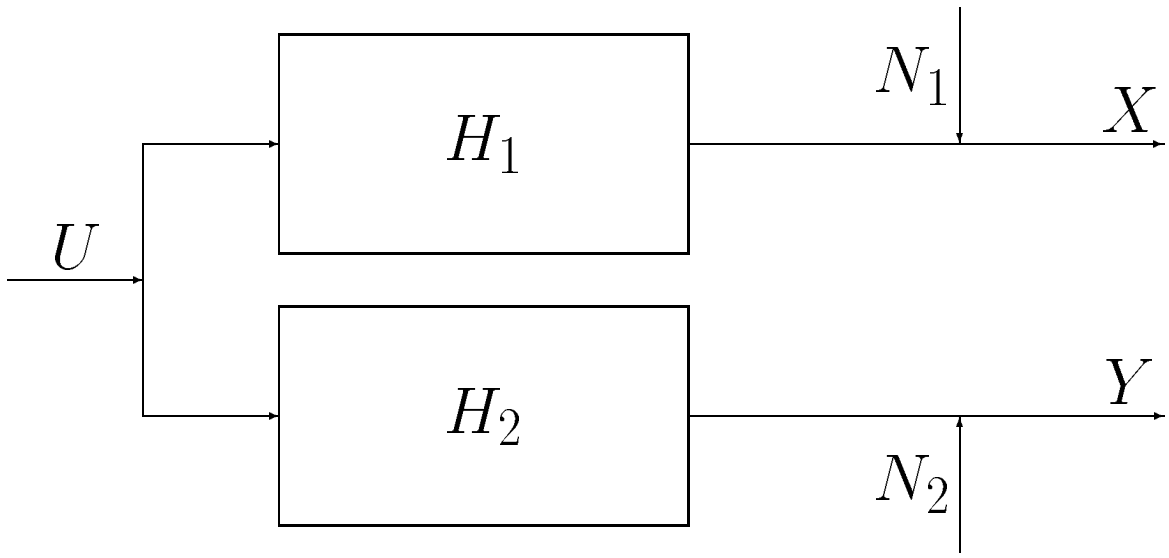

Figure 4.2: Schematic view of two sensors measuring the same input vibration.

are sampled simultaneously and digitized at 1 kHz. As indicated in fig. 4.2, these output signals consist of the input signal $u(t)$, transferred to the corresponding sensor, and the noise signals $n_1(t)$ and $n_2(t)$, respectively.
Using the Laplace transformation these relations can be written as

$$X(s) \quad = \quad H_1(s) \cdot U(s) + N_1(s) \tag{4.10}$$

$$Y(s) = H_2(s) \cdot U(s) + N_2(s), \tag{4.11}$$

where $X(s)$ is the Laplace transform of $x(t)$, etc.
Solving eqn. (4.10) for $U(s)$ and substituting this in equation (4.11) yields

$$Y(s) = H(s) \cdot X(s) + N(s), \tag{4.12}$$

with

$$H(s) = \frac{H_2(s)}{H_1(s)}, \tag{4.13}$$

$$N(s) = N_2(s) - H(s) \cdot N_1(s). \tag{4.14}$$

The corresponding scheme is shown in figure 4.3.

From the two output signals $x(t)$ and $y(t)$, the power spectrum density of both the ground

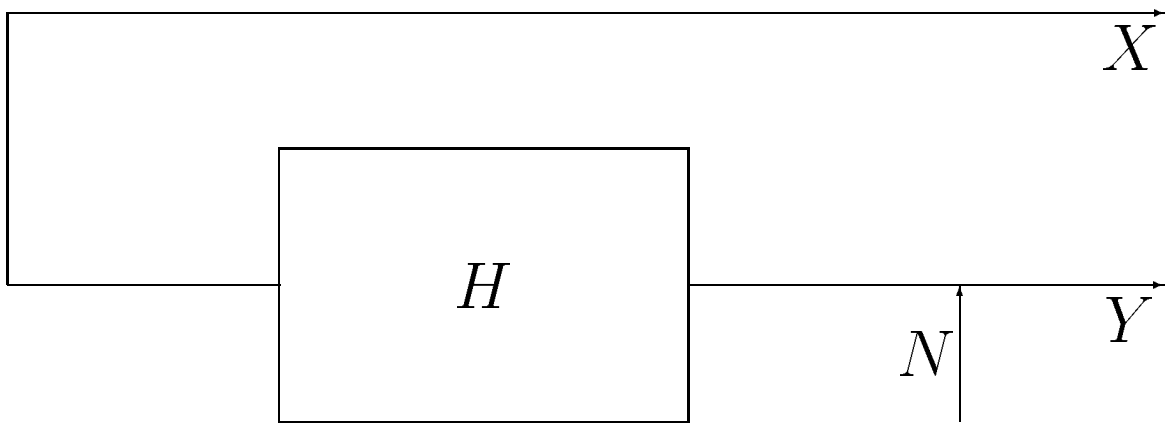

Figure 4.3: Equivalent scheme for coherence study.

motion and the internal noise of the sensors can be obtained using the correlation function [Ste 75]

$$\gamma = \frac{\Phi_{xy}}{\sqrt{\Phi_{xx}\Phi_{yy}}}, \tag{4.15}$$

with

$$\Phi_{xx} = \left\langle 2 \cdot \lim_{T\to\infty} \frac{1}{T} |X(f)|^2 \right\rangle, \tag{4.16}$$

$$\Phi_{yy} = \left\langle 2 \cdot \lim_{T\to\infty} \frac{1}{T} |Y(f)|^2 \right\rangle, \tag{4.17}$$

$$\Phi_{xy} = \left\langle 2 \cdot \lim_{T\to\infty} \frac{1}{T} X(f) Y^*(f) \right\rangle, \tag{4.18}$$

where $X(f)$ is the Fourier transform of $x(t)$

$$X(f) = \int_{-\frac{T}{2}}^{\frac{T}{2}} x(t) \cdot e^{-i \cdot 2\pi f t} \mathrm{d}t, \tag{4.19}$$

etc. As usual the asterisk denotes the complex conjugate.
According to eqn. (4.12) (see fig. 4.3) Φ_{xy} and Φ_{yy} can be rewritten as

$$\begin{aligned}\Phi_{xy} &= \left\langle 2 \cdot \lim_{T\to\infty} \frac{1}{T} XY^* \right\rangle \\ &= \left\langle 2 \cdot \lim_{T\to\infty} \frac{1}{T} X(HX+N)^* \right\rangle \\ &= \left\langle 2 \cdot \lim_{T\to\infty} \frac{1}{T} [XH^*X^* + XN^*] \right\rangle \\ &= H^*\Phi_{xx} \end{aligned} \tag{4.20}$$

and

$$\begin{aligned}\Phi_{yy} &= \left\langle 2 \cdot \lim_{T\to\infty} \frac{1}{T} YY^* \right\rangle \\ &= \left\langle 2 \cdot \lim_{T\to\infty} \frac{1}{T} (HX+N)(HX+N)^* \right\rangle \\ &= \left\langle 2 \cdot \lim_{T\to\infty} \frac{1}{T} (XX^*HH^* + XHN^* + X^*H^*N + NN^*) \right\rangle \\ &= \Phi_{xx}|H|^2 + \Phi_{nn}, \end{aligned} \tag{4.21}$$

since $x(t)$ and $n(t)$ are independent signals with $\langle XN^* \rangle = 0$ at all frequencies.
Utilizing the power spectra Φ_{xx}, Φ_{yy} and Φ_{xy} one gets the following relations:

$$H = \frac{\Phi_{xy}^*}{\Phi_{xx}}, \tag{4.22}$$

$$\Phi_{nn} = \Phi_{yy} - |H|^2\Phi_{xx}, \tag{4.23}$$

$$\Phi_{ss} = \Phi_{xx}|H|^2 = \Phi_{yy} \cdot |\gamma|^2, \tag{4.24}$$

$$\beta = \frac{\Phi_{ss}}{\Phi_{nn}} = \frac{\Phi_{xx}|H|^2}{\Phi_{nn}} = \frac{|\gamma|^2}{1-|\gamma|^2}, \tag{4.25}$$

where Φ_{nn}, Φ_{ss} and β are the noise power spectrum, signal power spectrum, and the signal-to-noise ratio, respectively. Here Φ_{ss} and Φ_{nn} are defined such that the correlated part of the two output signals $x(t)$ and $y(t)$ is referred to as the signal, while the uncorrelated part is called the noise. In the case of two sensors being placed side-by-side both probes measure the same input vibration; i. e. the input signals of both sensors are correlated. Thus any uncorrelated part in the output signals $x(t)$ and $y(t)$ is an artefact due to imperfections of the sensors, e. g. electronics noise. In the case of two probes with sufficiently low internal noise level being separated by some distance, the uncorrelated part in the output signals reflects a real property of the input signal, i. e. the ground motion in the two points.
The averaged power spectra Φ have been calculated by dividing each time series into overlapping segments, the overlap being 62.5% [Car 73], and Fourier-transforming these segments.
Since the discrete Fourier transformation of a signal $x(k)$ over n data points assumes a periodic signal with period length n, i. e. $x(k+n) = x(k)$, the Fourier transformation leads to enhanced amplitudes at high frequencies because in general $x(0) \neq x(n)$. The resulting step between the nth and the $(n+1)$th data point, which is equal to the zeroth one, contributes these additional high-frequency components. Therefore the time signal $x(t)$ has to be modified by multiplication with a so-called window. Here a Hanning window $w(k)$ with

$$w(k) = \frac{1}{2} - \frac{1}{2}\cos\frac{2\pi k}{n} \tag{4.26}$$

was used.
This method has been applied to the geophone motion sensors manufactured by KEBE Scientific Instruments [Keb 94] having a transfer function shown in figure 4.4. While the resonance frequency f_0 of the geophone itself is 4.5 Hz with a damping constant $\delta = 1$, the flat transfer function is achieved by application of several filters within the preamplifier circuit. The proportionality constant can be selected in three steps as 0.01, 0.02 and 0.05 mm/(Vsec) with a dynamic range of 0.05 to 0.25 mm/sec.

The rms value σ_n of the sensor noise in the frequency band f_0 to f_1 can be calculated by

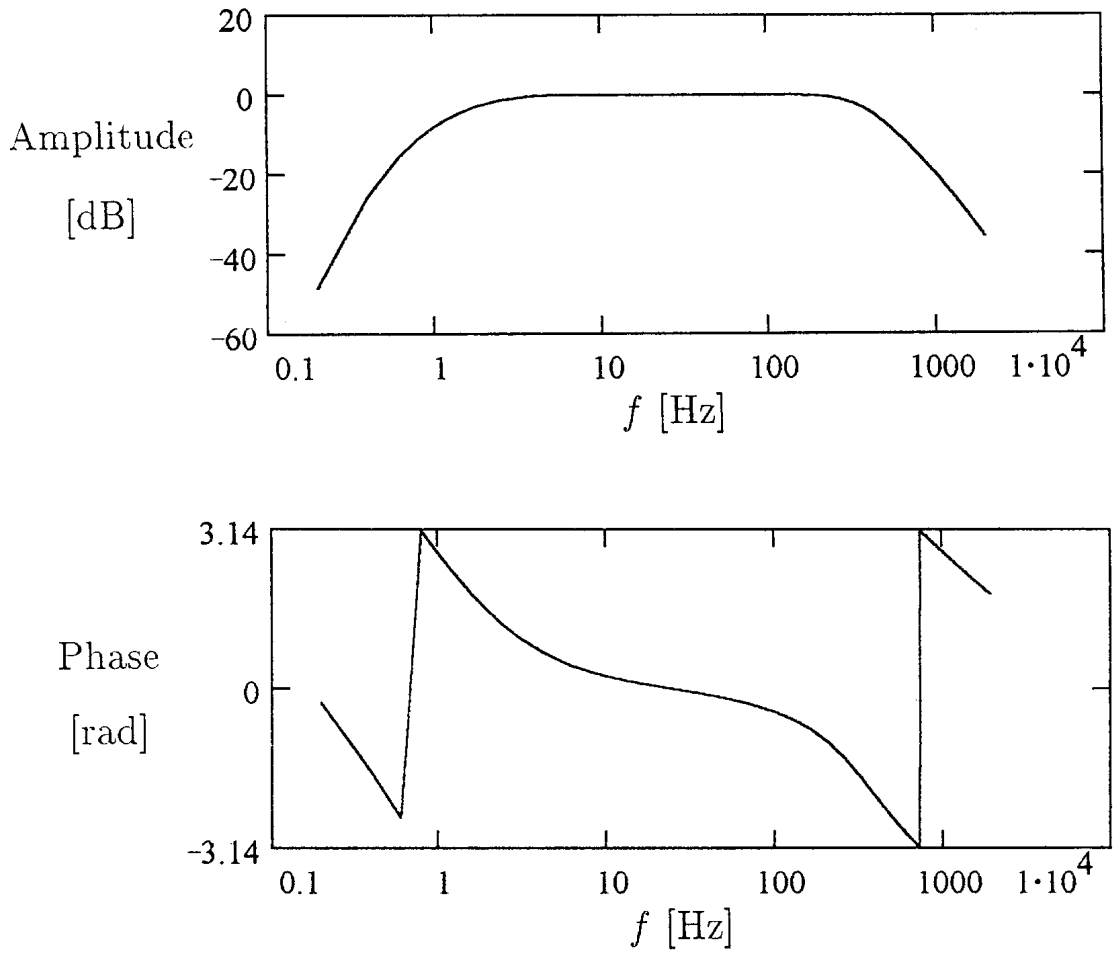

Figure 4.4: Bode plot of the KEBE geophone with preamplifier [Keb 94]. The amplitude is normalized to 0 dB at 16 Hz.

integrating the noise power spectrum Φ_{nn} over this frequency band:

$$\sigma_n^2 = \int_{\omega_0=2\pi f_0}^{\omega_1=2\pi f_1} \Phi_{nn}(\omega)\,\frac{\mathrm{d}\omega}{2\pi}. \tag{4.27}$$

Figure 4.5 shows the rms noise level of the KEBE sensors in the frequency band f_0 to infinity as a function of the lower frequency f_0 :

$$\sigma_n(f > f_0) = \sqrt{\int_{\omega_0=2\pi f_0}^{\infty} \Phi_{nn}(\omega)\,\frac{\mathrm{d}\omega}{2\pi}} \tag{4.28}$$

The resulting rms noise level in the frequency band from 2 Hz to infinity has been found to be

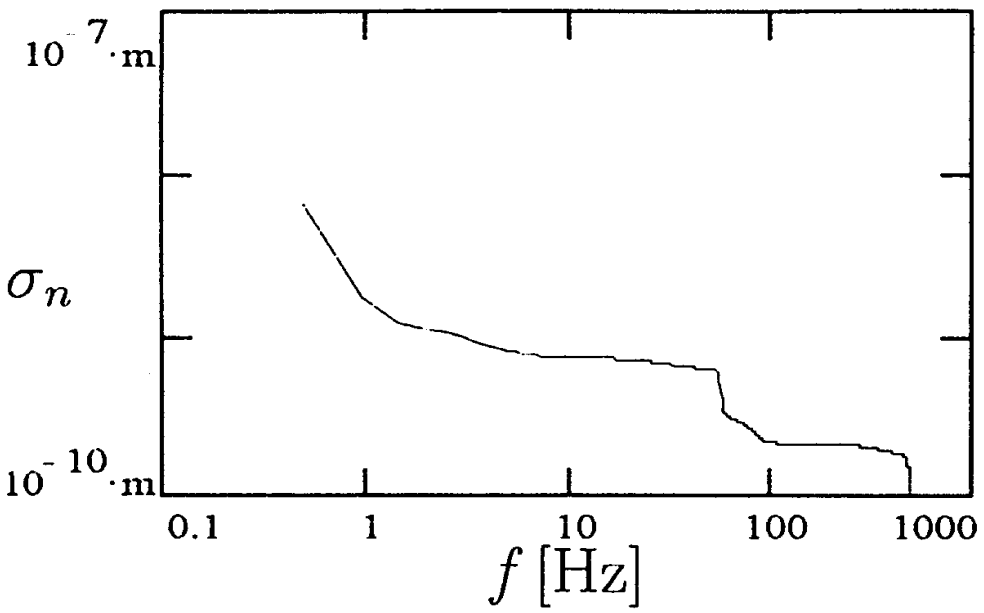

Figure 4.5: rms value of the internal noise of the KEBE sensors in the frequency band f_0 to infinity as function of the lower frequency f_0.

1.1 ± 0.3 nm, which is well below the quadrupole jitter tolerance even for the 1 TeV machine. Therefore these sensors have been considered useful for the active stabilization system.

5 Design of the active stabilization system

For reasons of simplicity as well as cost limitation the mechanical design is based on a single piezoelectric actuator tilting the quadrupole around a transverse horizontal axis. This is done in such a way that the magnet center is kept at rest with respect to the averaged vertical position as determined by the sensor on top of the magnet. The arrangement is shown schematically in figure 5.1. As shown in Appendix F, the effect of this tilt on the accelerator optics can be neglected compared to the corresponding offset of the quadrupole center.

The opposite end of the magnet is placed on two massive ball-ended feet to reduce dry friction.

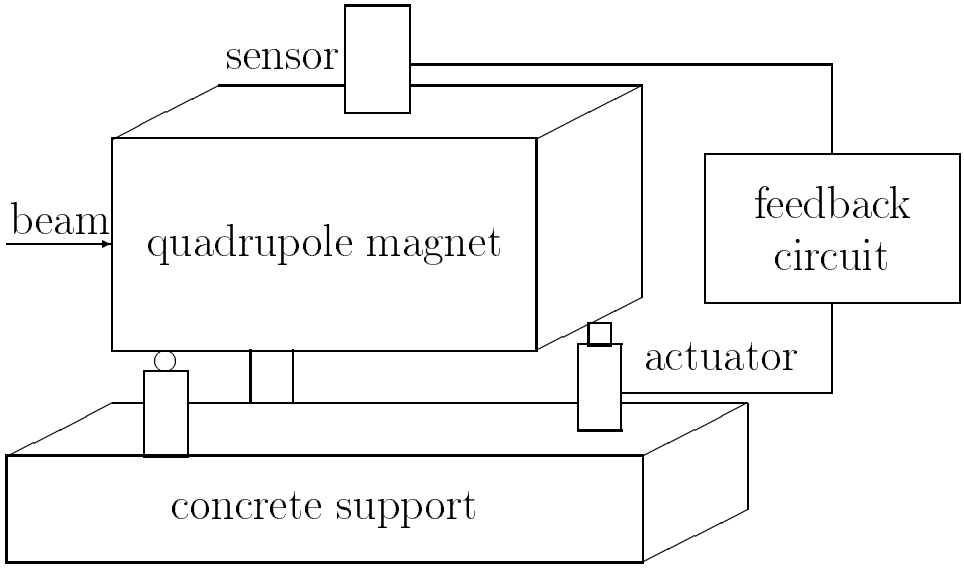

Figure 5.1: Schematic view of the active stabilization system.

To fix the horizontal magnet position two "arms" with sufficient vertical compliance but high stiffness in the horizontal direction have been placed on one side of the quadrupole. The sensor is mounted on top of the magnet just above its center. The complete active quadrupole support is shown in figure 5.2. Figures 5.3 to 5.5 show the design drawing of the active support with magnet and sensor.

The transfer function of the system actuator-magnet-geophone plus amplifiers has been determined using a network analyzer. Figure 5.6 shows the measured transfer function with an additional 1.6 Hz analog lowpass filter used as an integrator in order to get the displacement from the velocity output signal. This measured curve can be approximated as a sum of three resonances, multiplied by the transfer functions $H_{\mathrm{KEBE}}(s)$ of the KEBE sensor and $H_{\mathrm{LP}}(s)$ of the 1.6 Hz lowpass filter:

$$\begin{aligned} H(s) &= \left(\frac{\omega_1^2}{s^2 + 2\delta_1\omega_1 s + \omega_1^2} + \frac{0.44 \cdot \omega_2^2}{s^2 + 2\delta_2\omega_2 s + \omega_2^2} + \frac{0.07 \cdot \omega_3^2}{s^2 + 2\delta_3\omega_3 s + \omega_3^2} \right) \cdot \\ &\quad \cdot H_{\mathrm{KEBE}}(s) \cdot H_{\mathrm{LP}}(s) \cdot s \end{aligned} \tag{5.1}$$

with

$$\omega_1 = 2\pi \cdot 70\,\mathrm{Hz}, \tag{5.2}$$

$$\omega_2 = 2\pi \cdot 143\,\mathrm{Hz}, \tag{5.3}$$

$$\omega_3 = 2\pi \cdot 175\,\mathrm{Hz}, \tag{5.4}$$

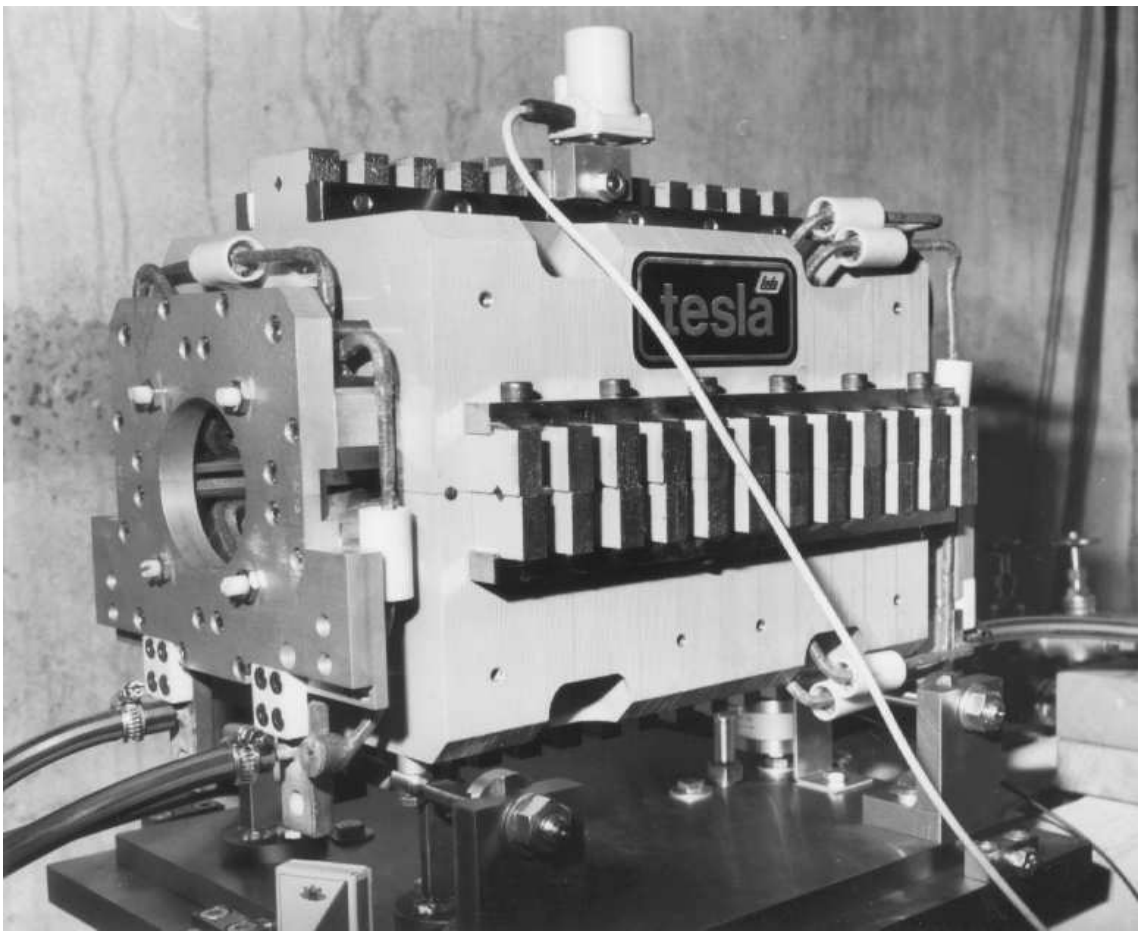

Figure 5.2: Active stabilization system, consisting of a KEBE geophone on top of the magnet and a piezo actuator below it to tilt the quadrupole around its horizontal transverse axis. The length of the magnet is about 30 cm.

$$\delta_1 = 0.2, \tag{5.5}$$
$$\delta_2 = 0.02, \tag{5.6}$$
$$\delta_3 = 0.01. \tag{5.7}$$

The stiffness of the piezo actuator is specified by the manufacturer to be $1300\,\mathrm{N}/\mu\mathrm{m}$. Together with a magnet mass of 100 kg, this should result in a resonance frequency of $f_r = 575\,\mathrm{Hz}$. Nevertheless the lowest resonance occurs at 70 Hz (see fig. 5.6), corresponding to a spring constant D of about $20\,\mathrm{N}/\mu\mathrm{m}$ which is still quite large regarding sensitivity to forces acting on the magnet directly. On the other hand this reduces the bandwidth of the feedback system significantly due to the 180 degree phase shift occuring at the second lowest resonance frequency which was determined at 143 Hz, corresponding to a spring constant of $D = 80\,\mathrm{N}/\mu\mathrm{m}$.
The origin of these resonances could not be identified. Experiments using lead blocks with a mass equivalent to the magnet mass placed directly onto the piezo actuator showed practically the same transfer function as the complete support with the quadrupole. This indicates that the piezo actuator has a much lower stiffness than given in its data sheets. Experiments with three different actuators provided by two different manufacturers and connected to two different high voltage amplifiers gave similar transfer functions within less than 10 % frequency difference, although the specified stiffnesses of the actuators ranged from 200 to $1300\,\mathrm{N}/\mu\mathrm{m}$.

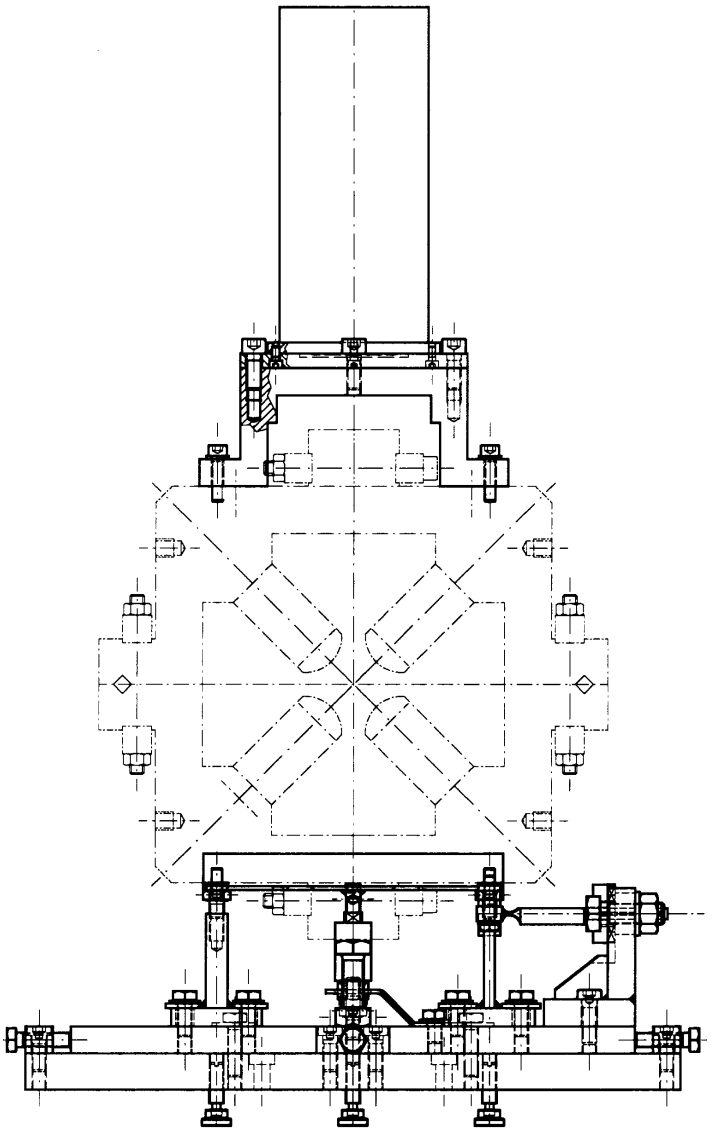

Figure 5.3: Design drawing of the active stabilization system (front view). The "arms" fixing the magnet's horizontal position are shown on the right. Instead of the KEBE geophone, a Guralp CMG-40T broadband seismometer is shown as vibration sensor.

Additionally the transfer function was measured with a piezoelectric accelerometer used as motion sensor. Since the results remained the same one can also exclude the sensor as origin of these resonances. Measurements of the transfer function at different positions in DESY hall 2 in order to exclude any effects of the floor of this building also showed no effect.
Measurements of the static stiffness of the piezo actuator resulted in a stiffness of $1000 \pm 300\,\mathrm{N}\,\mu\mathrm{m}^{-1}$, showing no force dependence.
The whole system is placed on a very stiff concrete support with high internal damping to avoid amplification of ground motion due to mechanical resonances. As experimentally confirmed, this support has no mechanical eigenmodes in the frequency range up to 300 Hz. The triangular cross section has been chosen to ensure the transfer of horizontal ground motion without further amplification, i. e. $H_{\mathrm{hor}} = 1$ for frequencies below 300 Hz.

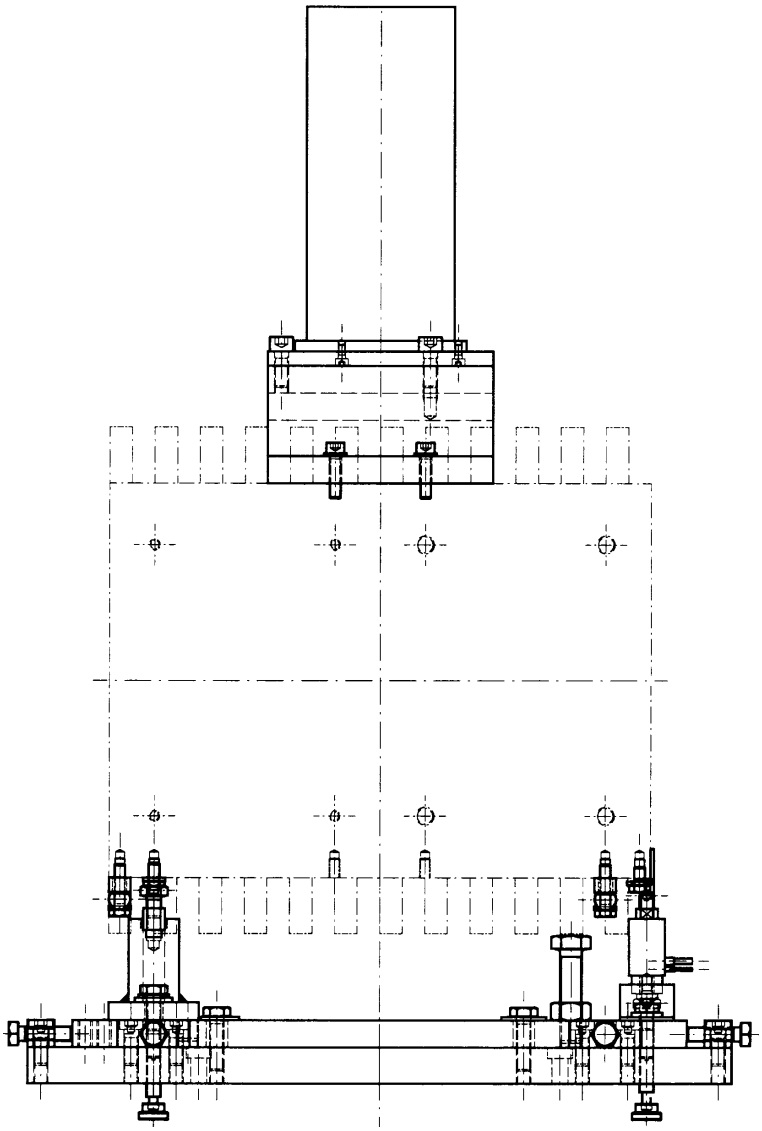

Figure 5.4: Design drawing of the active stabilization system (side view). The massive ball-ended feet are shown on the left, while the piezo actuator supports the right end of the magnet. A M16 screw supports the magnet while the piezo actuator is being installed.

For this first prototype of the active stabilization system the feedback circuit has been realized on a PC with 16 bit A/D board. The sampling frequency has been chosen at 2 kHz. Compared to an analog system this has several advantages. In particular filters with extremely long time constants of many seconds can be realized, limited only by the numerical accuracy of the processor. Furthermore, the feedback algorithm can be changed easily.
The algorithm consists of a 0.01 Hz highpass filter to remove offsets of the input signal, a 100 sec lowpass filter used as integrator to get the displacement from the velocity signal and several digital filters, as shown schematically in fig. 5.7. An 8 Hz first-order lowpass filter is used to suppress the 143 Hz resonance below 0 dB in order to achieve stability of the feedback system. To compensate the gain loss connected with this low cutoff frequency, a 7 to 30 Hz first-order bandpass filter is connected in parallel to the output of this lowpass filter, resulting in addi-

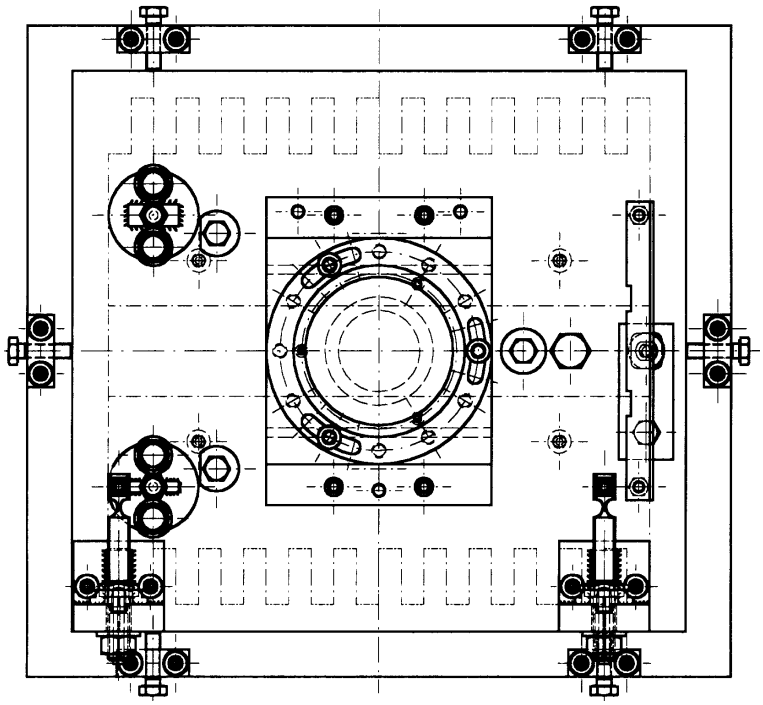

Figure 5.5: Design drawing of the active stabilization system (top view). The two "arms" fixing the horizontal position are shown on the bottom.

tional gain in this frequency band without any global but only some local phase shift. The gain factors G_1 and G_2 are chosen as 2.9 and 1.5, respectively, which is close to the stability limit of the feedback system. This results in increased amplitudes at 0.8 Hz and between 30 and 70 Hz. Nevertheless, this is experimentally confirmed to be the best compromise between a high attenuation factor in the frequency band from 2 Hz to 30 Hz and this amplification, resulting in the smallest rms value for frequencies higher than 2 Hz. Of course this result depends on the ground motion spectrum and may have to be re-optimized in the linear collider environment.

As was observed during the tests, the feedback system tends to perform low frequency oscillations over the total 16 bit range of the DAC after having accidentally reached its range limit due to some unusually high ground motion amplitudes. To re-stabilize the system it is necessary to decrease the gain. Therefore the gain factor G_2 is reduced by 20 % each time the output value of the DAC reaches ± 15 bit and then increased again by an increment of $2 \cdot 10^{-4}$ in each cycle. This results in a high reliability of the system even under extreme conditions.
An additional anti-aliasing filter (Appendix A) is not neccessary for two reasons. Firstly the preamplifier of the KEBE geophone provides analog lowpass filters with cutoff frequencies around 300 Hz, as shown in the Bode plot of the sensor (fig. 4.4). Secondly the ground motion power spectrum of displacement is proportional to ω^{-4}, corresponding to a velocity power spectrum proportional to ω^{-2}. Together with the analog lowpass filters of the sensor this ensures that practically no high frequency contributions above half the sampling frequency of 2 kHz are present in the analog signal.

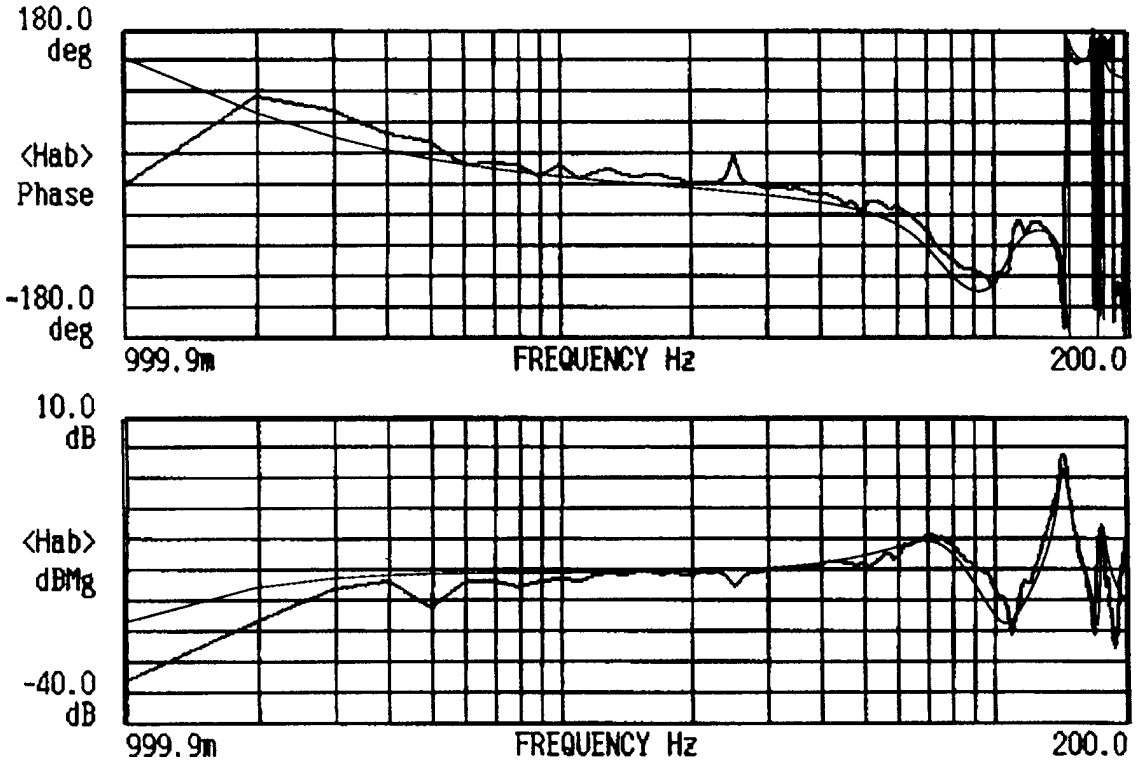

Figure 5.6: Measured transfer function H(s) of the system actuator-magnet-geophone. The smooth line shows a fit according to eqn. (5.1).

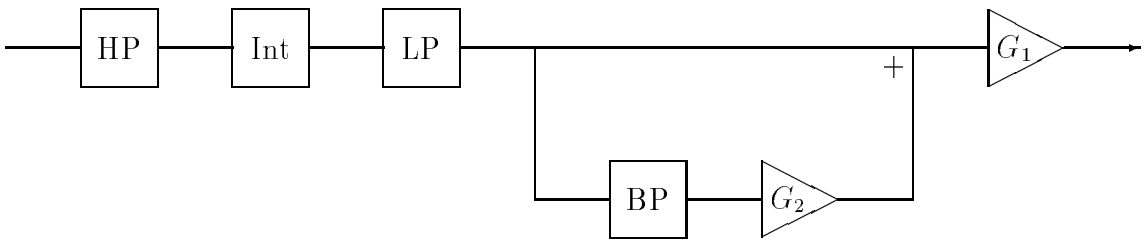

Figure 5.7: Schematic view of the feedback algorithm, consisting of an integrator (Int) and several digital filters (lowpass LP, highpass HP, bandpass BP).

6 Experimental results on active stabilization

The active stabilization system has been set up in DESY hall 2, an experimental hall close to the DESY synchrotrons which has been chosen for the installation of the S-band test linac. Since there are two accelerators, several transformers and some other technical equipment operated nearby, it may be considered as an example of an operating linear collider environment. Therefore the results obtained in this environment may be comparable to those to be expected in the future accelerator.

To determine the performance of the system, a second KEBE sensor was placed on the floor just below the magnet. The signals of the feedback sensor as well as the ground motion signal were simultaneously sampled at 400 Hz to exclude artefacts in the results due to the statistical behaviour of ground motion. Sets of 1024 data points each were integrated to obtain the displacement from the velocity signal, multiplied by a Hanning window (see Section 4) and Fourier-transformed in order to determine the power spectra Φ_{xx} and Φ_{yy} of the two signals. Here the subscript x denotes the ground motion signal, while y corresponds to the signal measured on top of the magnet. From these power spectra the rms values, σ_x and σ_y, of the displacement in the frequency band f_0 to infinity can be calculated as

$$\sigma(f > f_0) = \sqrt{\int_{\omega_0=2\pi f_0}^{\infty} \Phi(\omega)\,\frac{\mathrm{d}\omega}{2\pi}}. \tag{6.1}$$

To ensure the reliability of this method, signals of both sensors are processed with the feedback system switched off. In this case the transfer function is expected to be unity. Because the internal noise level of the two identical sensors is negligible compared to typical ground motion amplitudes the correlation function γ is expected to be unity in the frequency range under study. With this assumption, the transfer function H reduces to (see eqn. (4.12))

$$H(f) = \frac{Y(f)}{X(f)}, \tag{6.2}$$

and therefore its modulus can be calculated from the square root of the ratio of both power spectra:

$$|H(f)| = \sqrt{\frac{\Phi_{yy}}{\Phi_{xx}}}. \tag{6.3}$$

As shown in figure 6.1, the transfer function is indeed close to unity in the frequency range below approximately 30 Hz, while amplitudes of vibrations beyond this frequency appear to be higher on top of the magnet than on the floor. This latter effect results from the lowest mechanical resonance at 70 Hz but, due to the small ground motion amplitudes in this frequency region, its contribution to the rms value is negligible. With the feedback switched on this effect is slightly amplified (fig. 6.2) but still does not appear to be harmful. Below 30 Hz the damping effect is clearly visible.

The measured feedback gain, calculated as the square root of the ratio of these two power spectra, is shown in figure 6.3 together with the theoretically expected curve. Both curves are in good agreement.

As already mentioned in the introduction, the aim of active stabilization is to reduce the (uncorrelated) quadrupole jitter to an rms value of less than 43 nm for $f > 2$ Hz for the 1 TeV S-band Linear Collider. Fig. 6.4 presents the rms value σ of simultaneously measured ground

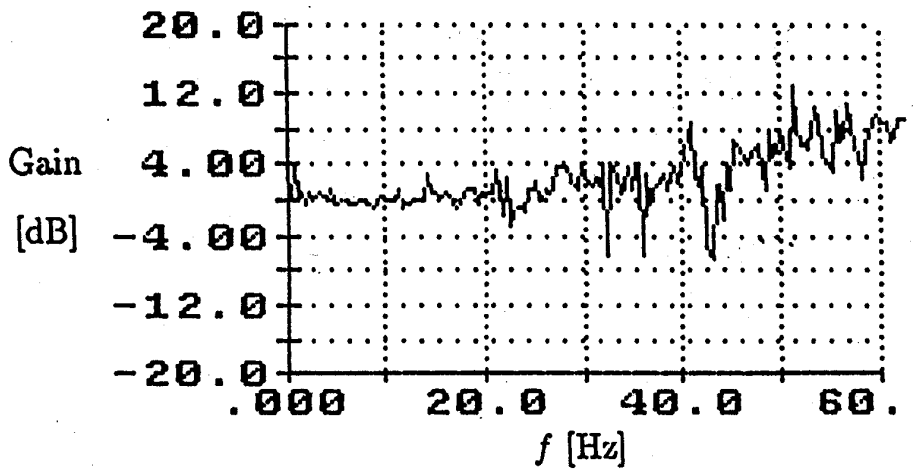

Figure 6.1: Measured transfer function for ground motion acting on the magnet with the feedback system switched off. As expected the transfer function is practically unity below approximately 30 Hz, while beyond this frequency ground motion amplitudes are amplified by the magnet support.

and magnet motion as a function of the lower cut-off frequency f_0, as has been calculated from the power spectra shown in fig. 6.2. Although a vertical ground motion rms value of 100 nm at $f_0 = 2$ Hz is considered a noisy environment, the active stabilization system is capable of damping magnet motion to an rms value of about 26 nm in this frequency band. Taking into account the very low internal noise of the sensors, one can expect even lower values in less noisy environments. Therefore this system might be even applicable in some parts of the final focus system where no klystrons and modulators operated at 50 Hz are present.
Cooling water pressure fluctuations are known as a main source of high frequency quadrupole vibrations for example at SLAC [Tur 95a]. To investigate their effect magnet motion power spectra have been obtained with cooling water switched on and off. In this case, data samples of 20 sec each were recorded at 1 kHz. Both data sets were divided into 20 overlapping windows of 2048 data points and Fourier transformed. The obtained power spectra were averaged in order to suppress artefacts due to the non-stationarity of the statistical ground motion signal. While the design water flow is 120 l/h, these data were taken at an increased flow of 220 l/h. It turned out that the influence of cooling water is almost negligible. The only difference in both power spectra is a small enhancement around 100 Hz. Its contribution to the rms value is less than 1 nm and may therefore be considered negligible.
The data presented in figs. 6.2 to 6.4 were obtained at a cooling water flow of 220 l/h.

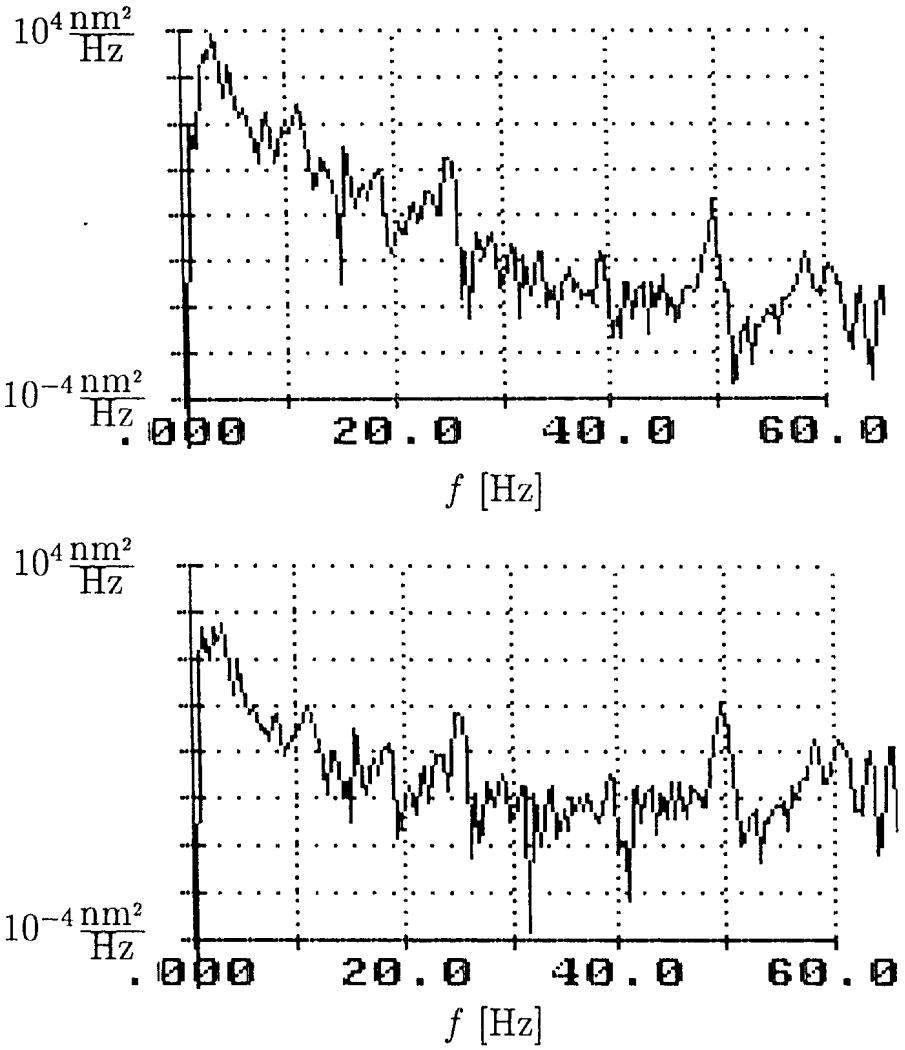

Figure 6.2: Simultaneously measured power spectra of ground motion (top) and magnet motion (bottom) with the feedback system switched on. Below 30 Hz the damping effect of the active stabilization system is clearly visible, while for higher frequencies ground motion amplitudes are amplified.

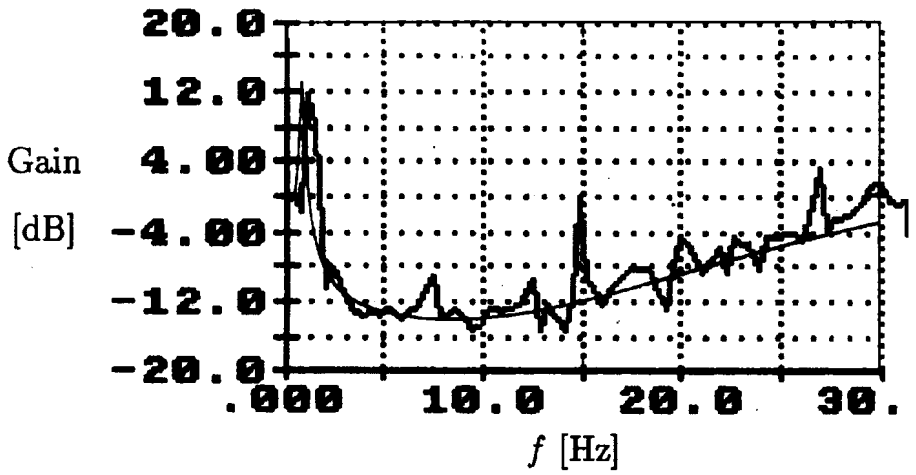

Figure 6.3: Measured feedback gain (thick line) in the frequency band from 0 to 30 Hz, calculated from the square root of the ratio of the two power spectra shown in figure 6.2. The smooth thinner curve shows the theoretical transfer function.

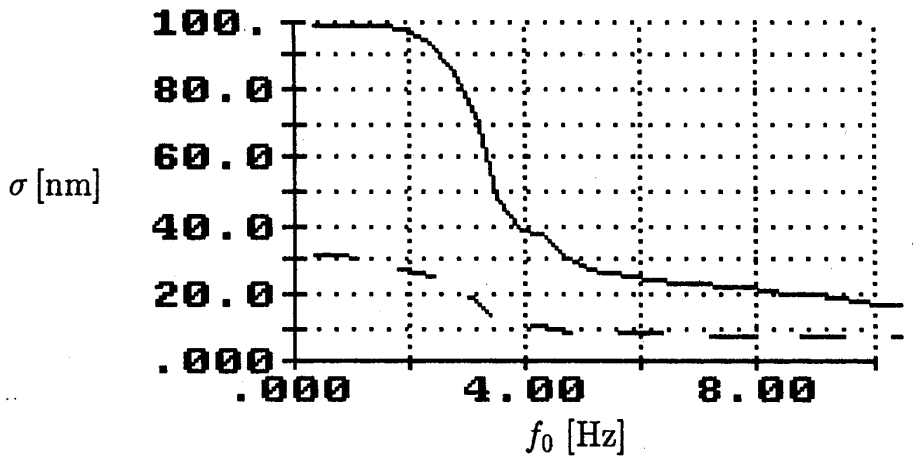

Figure 6.4: rms value of ground motion (solid) and magnet motion (dashed) in the frequency band f_0 to infinity as function of the lower frequency f_0, measured with the feedback system switched on.

7 Ground motion simulation models

Two complementary algorithms have been developed to investigate the influence of ground motion on the beam dynamics in a linear collider. The first one is based on digital filters shaping white noise random signals in order to get a realistic spectrum and correlation properties, while the second one employs fast Fourier transformations to compute ground motion signals in the time domain from the power spectra of absolute ground motion and the coherence spectra. It should be emphasized that none of these algorithms is based on a "realistic" model of ground motion; the purpose of these studies was just to create an algorithm producing signals with similar spectra and coherence properties as measured from ground motion.

7.1 The filter-based model

As already mentioned in Section 2, the power spectrum $P(\omega)$ of absolute ground motion can be roughly approximated as

$$P_{\mathrm{tot}}(\omega) = \frac{B}{\omega^4}, \tag{7.1}$$

while the power spectrum of uncorrelated (ATL-)motion of two points at a distance L is desribed as

$$\rho(\omega, L) = \frac{A \cdot L}{\omega^2}. \tag{7.2}$$

Obviously, the latter relation has to be modified in the high frequency domain where $\omega > \omega_0 = \sqrt{B/(A \cdot L)}$, since otherwise $P_{\mathrm{tot}}(\omega) < \rho(\omega, L)$ there. Therefore, equation (7.2) is considered to be valid only for $\omega < \omega_0$ [Ser 95].
The correlated part $p_{\mathrm{corr},n+1}(t)$ of the motion signal of magnet $(n+1)$ with respect to that of magnet n can be calculated by applying a first order lowpass filter with a cutoff frequency $\omega_0 = \sqrt{B/(A \cdot L)}$ to the motion signal $p_{\mathrm{tot},n}(t)$ of the nth magnet. In the frequency domain, this leads to

$$\begin{aligned} P_{\mathrm{corr},n+1}(\omega) &= \left|\frac{\omega_0}{s+\omega_0}\right|^2 \cdot P_{\mathrm{tot},n}(\omega) \\ &= \left|\frac{\omega_0}{s+\omega_0}\right|^2 \cdot \frac{B}{\omega^4}, \end{aligned} \tag{7.3}$$

with $P_{\mathrm{corr},n+1}(\omega)$ and $P_{\mathrm{tot},n}(\omega)$ being the power spectrum of the correlated part of motion of the $(n+1)$th magnet with respect to the nth one, and the power spectrum of absolute motion of the nth magnet, respectively.
The corresponding uncorrelated part $p_{\mathrm{uncorr},n+1}(t)$ can then be computed by application of a first order highpass filter with cutoff frequency ω_0 to another signal $p_{n+1}(t)$ with the same power spectrum $P_{n+1}(\omega)$ as $p_{\mathrm{tot},n}(t)$,

$$\begin{aligned} P_{\mathrm{uncorr},n+1}(\omega) &= \left|\frac{s}{s+\omega_0}\right|^2 \cdot P_{n+1}(\omega) \\ &= \left|\frac{s}{s+\sqrt{\frac{B}{A \cdot L}}}\right|^2 \cdot \frac{B}{\omega^4} \end{aligned}$$

$$
\begin{aligned}
&= \frac{\omega^2}{\omega^2 + \frac{B}{A \cdot L}} \cdot \frac{B}{\omega^4} \\
&= \frac{B \cdot A \cdot L}{A \cdot L \cdot \omega^2 + B} \cdot \frac{1}{\omega^2}.
\end{aligned} \tag{7.4}
$$

Thus, in the low-frequency limit we get

$$
\begin{aligned}
\lim_{\omega \to 0} P_{\mathrm{uncorr},n+1} &= \lim_{\omega \to 0} \left[\frac{B \cdot A \cdot L}{A \cdot L \cdot \omega^2 + B} \cdot \frac{1}{\omega^2} \right] \\
&= \frac{A \cdot L}{\omega^2} \\
&= \rho(\omega, L),
\end{aligned} \tag{7.5}
$$

which reflects the ATL rule.
The total motion $p_{\mathrm{tot},n+1}(t)$ of the $(n+1)$th magnet is then calculated as the sum of its correlated part $p_{\mathrm{corr},n+1}(t)$ and the corresponding uncorrelated signal $p_{\mathrm{uncorr},n+1}(t)$, leading to a total power spectrum

$$
\begin{aligned}
P_{\mathrm{tot},n+1}(\omega) &= P_{\mathrm{corr},n+1}(\omega) + P_{\mathrm{uncorr},n+1}(\omega) \\
&= \left| \frac{\omega_0}{s + \omega_0} \right|^2 \cdot P_{\mathrm{tot},n}(\omega) + \left| \frac{s}{s + \omega_0} \right|^2 \cdot P_{n+1}(\omega) \\
&= \left[\left| \frac{\omega_0}{s + \omega_0} \right|^2 + \left| \frac{s}{s + \omega_0} \right|^2 \right] \cdot P_{\mathrm{tot},n}(\omega) \\
&= \frac{\omega_0^2 + |i\omega|^2}{|i\omega + \omega_0|^2} \cdot P_{\mathrm{tot},n}(\omega) \\
&= \frac{\omega_0^2 + \omega^2}{\omega^2 + \omega_0^2} \cdot P_{\mathrm{tot},n}(\omega) \\
&= P_{\mathrm{tot},n}(\omega),
\end{aligned} \tag{7.6}
$$

since $P_{\mathrm{tot},n}(\omega) = P_{n+1}(\omega)$. Thus the various filters used in this model lead to identical power spectra P_{tot} of absolute motion of each magnet, while the uncorrelated motion of two magnets with respect to each other occurs according to the ATL rule.
The resulting coherence $|\gamma|$ can be calculated as (see eqn. (4.25))

$$
\begin{aligned}
|\gamma| &= \sqrt{\frac{P_{\mathrm{corr},n}}{P_{\mathrm{uncorr},n}} \Bigg/ \left(1 + \frac{P_{\mathrm{corr},n}}{P_{\mathrm{uncorr},n}} \right)} \\
&= \sqrt{\frac{\left| \frac{\omega_0}{s+\omega_0} \right|^2}{\left| \frac{s}{s+\omega_0} \right|^2} \Bigg/ \left(1 + \frac{\left| \frac{\omega_0}{s+\omega_0} \right|^2}{\left| \frac{s}{s+\omega_0} \right|^2} \right)} \\
&= \sqrt{\frac{|\omega_0|^2}{|s|^2} \Bigg/ \left(1 + \frac{|\omega_0|^2}{|s|^2} \right)} \\
&= \sqrt{\frac{\omega_0^2}{|s|^2 + \omega_0^2}}.
\end{aligned} \tag{7.7}
$$

These relations form the basis for the filter-based model.
This simple model is further improved in order to get a more realistic spectrum including the

microseismic peak, the 2.5 Hz resonance and some additional high frequency vibrations. For this purpose, the ground motion spectrum has to be expressed as a sum of power spectra that can be realized by filtering white noise, so its various terms can be interpreted as filter transfer functions. According to Appendix B.1, this requires integer exponents of the frequency ω resp. the Laplace variable s. For this reason, equation (2.42) is not applicable in this context. Therefore the total power spectrum is expressed as

$$\begin{aligned} P(\omega) &= \left|\frac{B}{s^4}\right| + \left|\frac{4.225\cdot 10^{-14}}{s^2}\right| \mathrm{m}^2\cdot\mathrm{Hz} + \left|\frac{7\cdot 10^{-6}}{s^2 + 9.425\,\mathrm{Hz}\cdot s + 246.74\,\mathrm{Hz}^2}\right|^2 \mathrm{m}^2\cdot\mathrm{Hz}^3 \\ &\quad + \left|\frac{7\cdot 10^{-7}}{s^2 + 0.528\,\mathrm{Hz}\cdot s + 0.774\,\mathrm{Hz}^2}\right|^2 \mathrm{m}^2\cdot\mathrm{Hz}^3, \end{aligned} \tag{7.8}$$

with $s = i\omega = i\cdot 2\pi f$ being the Laplace variable.
In this fit, the first term again represents the general $1/\omega^4$ behaviour of the power spectrum, while the others add some high-frequency noise, the 2.5 Hz resonance of the upper earth's crust, and the microseismic peak, respectively.
As an example, figure 7.1 shows the resulting spectra of absolute and relative motion of two magnets at a distance of $L = 30\,\mathrm{m}$ for $A = 4\cdot 10^{-6}\,\frac{\mu\mathrm{m}^2}{\mathrm{m\cdot sec}}$ and $B = 3\cdot 10^{-2}\,\mu\mathrm{m}^2\cdot\mathrm{Hz}^3$, while fig. 7.2 presents the coherence $|\gamma|$ for three different distances $L = 5\,\mathrm{m}$, $L = 15\,\mathrm{m}$ and $L = 30\,\mathrm{m}$, calculated according to equation (7.7). The parameter A is chosen according to measurements at HERA [Bri 94], while B is adapted such that both the resulting power spectrum and the coherence are in good agreement with measurements.
The first-order lowpass filters employed in this model introduce a certain unavoidable phase shift, leading to a travelling wave-like characteristic of the correlated motion along the linac. Since this can only lead to enhanced beam jitter amplitudes compared to ground motion with vanishing additional phase shift, the model tends to over-estimate the effect of ground motion on the beam trajectory. Furthermore this model does not contain any wave properties of ground motion as has been clearly observed for the microseismic peak and the 2.5 Hz resonance of the upper earth's crust. Additionally, the clearly visible enhanced coherence around these two peaks is not reflected in this model.

7.2 The FFT-based model

To overcome the deficiencies of the filter-based simulation algorithm and for a consistency check, a second ground motion simulation model based on Fourier transformations has been developed.
As already mentioned in Section 2, the absolute ground motion power spectrum $\Phi(\omega)$ measured in HERA hall West can be approximated as (eqn. (2.42), $f = \omega/(2\pi)$)

$$\begin{aligned} \Phi(\omega) \approx \Bigg[&\frac{2\cdot 10^{-6}}{\left(\frac{\omega}{2\pi\cdot 0.001\,\mathrm{Hz}}\right)^4} + \frac{10^{-3}}{1+\left(\frac{\omega}{2\pi\,\mathrm{Hz}}\right)^{\frac{5}{2}}} + \frac{5}{\left[1+\left(\frac{\frac{\omega}{2\pi}-0.14\,\mathrm{Hz}}{0.14\cdot 0.14\,\mathrm{Hz}}\right)^2\right]^{\frac{3}{2}}} \\ &+ \frac{2\cdot 10^{-3}}{\left[1+\left(\frac{\frac{\omega}{2\pi}-2.5\,\mathrm{Hz}}{0.45\cdot 2.5\,\mathrm{Hz}}\right)^2\right]^{\frac{3}{2}}} \Bigg] \frac{\mu\mathrm{m}^2}{\mathrm{Hz}}. \end{aligned} \tag{7.9}$$

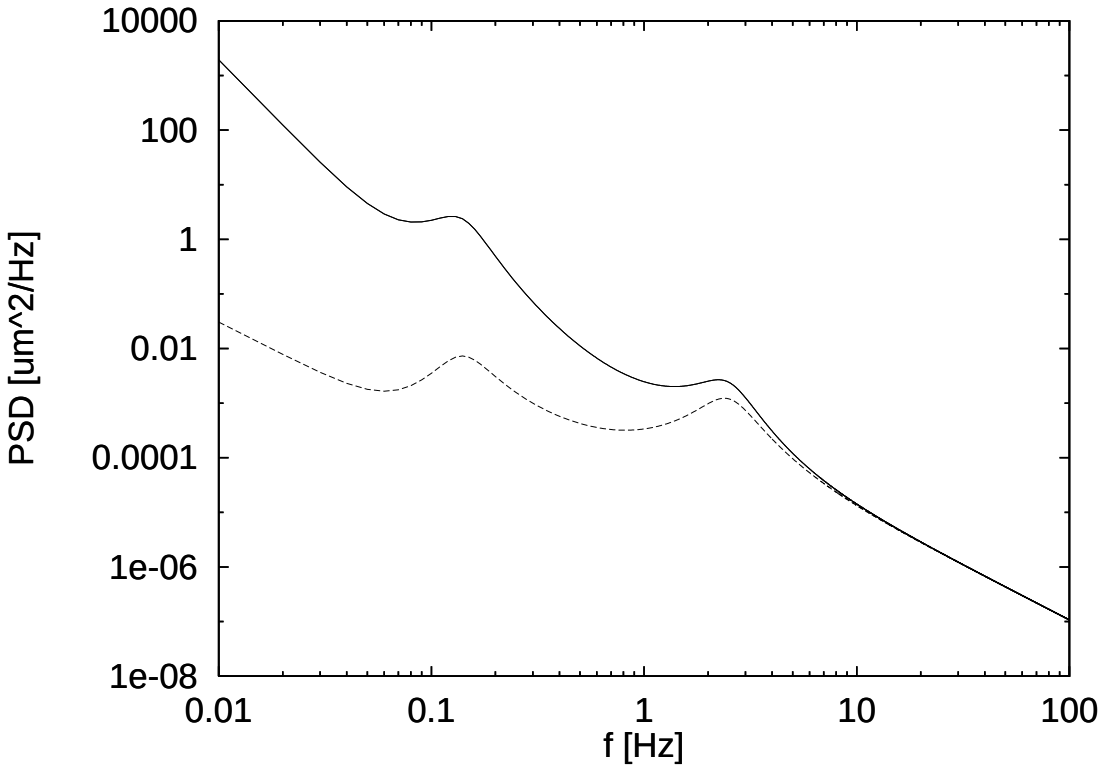

Figure 7.1: Power spectra (PSD) of absolute (solid line) and relative (dashed line) motion of two magnets at $L = 30\,\mathrm{m}$ distance for $A = 4 \cdot 10^{-6}\,\frac{\mu\mathrm{m}^2}{\mathrm{m\cdot sec}}$ and $B = 3 \cdot 10^{-2}\,\mu\mathrm{m}^2 \cdot \mathrm{Hz}^3$.

For the computation of the time-dependent motion signals at various points s_k along a straight line, the corresponding amplitude spectrum $P_a(\omega)$ has to be multiplied by a phase factor function $\exp[i(\omega t + \phi_k(\omega)]$ and inversely Fourier transformed.
As can be easily shown, this leads to perfectly correlated signals $x(t)$ and $y(t)$ at any two points s_x and s_y for any arbitrarily chosen initial phase functions $\phi_x(\omega)$ and $\phi_y(\omega)$,

$$\begin{aligned} |\gamma(\omega)| &= \left| \frac{\Phi_{xy}(\omega)}{\sqrt{\Phi_{xx}(\omega)\Phi_{yy}(\omega)}} \right| \\ &= \left| \frac{\Phi(\omega) \cdot \exp[i(\phi_x(\omega) - \phi_y(\omega))]}{\Phi(\omega)} \right| \\ &= 1. \end{aligned} \tag{7.10}$$

On the other hand, averaging over all neighbouring points s_k, s_{k-1} distanced by the same amount L leads to the coherence

$$\begin{aligned} |\gamma(\omega)| &= |\langle \exp[i(\phi_k(\omega) - \phi_{k-1}(\omega))] \rangle| \\ &= |\langle \exp[i \cdot \Delta\phi_k(\omega)] \rangle| \end{aligned} \tag{7.11}$$

with

$$0 \leq |\gamma(\omega)| \leq 1. \tag{7.12}$$

Assuming $\Delta\phi_k$ to be normally distributed with mean value $\mu = 0$ and variance σ^2 leads to the corresponding coherence

$$\begin{aligned} |\gamma| &= \left| \lim_{K\to\infty} \frac{1}{K} \sum_{k=1}^{K} \exp(i \cdot \Delta\phi_k) \right| \\ &= \left| \frac{1}{\sqrt{2\pi\sigma^2}} \int_{-\infty}^{\infty} \exp\left(-\frac{1}{2\sigma^2}\phi^2\right) \cdot \exp(i \cdot \phi)\, \mathrm{d}\phi \right| \\ &= \left| 2 \cdot \frac{1}{\sqrt{2\pi\sigma^2}} \int_{0}^{\infty} \exp\left(-\frac{1}{2\sigma^2}\phi^2\right) \cos\phi\, \mathrm{d}\phi \right| \\ &= \exp\left(-\frac{\sigma^2}{2}\right). \end{aligned} \tag{7.13}$$

For the computation of signals with a desired correlation function $\gamma(\omega)$, the phases $\phi_k(\omega)$ for the motion signal at the location s_k are calculated from those at the point s_{k-1} according to

$$\phi_k(\omega) = \phi_{k-1}(\omega) + \Delta\phi_k(\omega), \tag{7.14}$$

with $\Delta\phi_k(\omega)$ being normally distributed with $\sigma(\omega) = \sqrt{-2\ln(\gamma(\omega))}$ and mean value $\mu = 0$.
It is sufficient to choose $\gamma(\omega)$ for only one distance L_0. From this elementary cell the coherence of any other distance L results automatically,

$$|\gamma(L)| = \exp\left(-\frac{L}{L_0}\frac{\sigma^2(L_0)}{2}\right). \tag{7.15}$$

In the case of the S-band Linear Collider, this basic length was chosen equal to the length of one accelerating structure, i. e. $L = 6\,\mathrm{m}$.
For simulation purposes, the coherence function $|\gamma(\omega)|$ for two points separated by $L = 6\,\mathrm{m}$ has been described as

$$\begin{aligned} |\gamma(\omega)| = {} & \exp\left(-\frac{0.08}{2\pi} \cdot \omega\right) + \\ & +0.0028 \cdot \frac{\omega}{\sqrt{(\omega_m^2 - \omega^2)^2 + (2 \cdot \delta \cdot \omega_m \cdot \omega)^2}} + \\ & +1.05 \cdot \frac{\omega}{\sqrt{(\omega_c^2 - \omega^2)^2 + (2 \cdot \delta \cdot \omega_c \cdot \omega)^2}} \end{aligned} \tag{7.16}$$

with

$$\omega_m = 2\pi \cdot 0.14\,\mathrm{Hz} \tag{7.17}$$

$$\omega_c = 2\pi \cdot 2.5\,\mathrm{Hz}, \tag{7.18}$$

$$\delta = 0.2. \tag{7.19}$$

In this fit, the first term describes the decrease of the coherence with increasing frequency, while the second and third describe the enhanced coherence at the microseismic peak around 0.14 Hz and the upper earth's crust resonance around 2.5 Hz, respectively.
As a comparison of figure 7.3 for $L = \frac{5}{6} \cdot 6\,\mathrm{m} = 5\,\mathrm{m}$ and fig. 2.3 a indicates, this is a reasonable description of the measured coherence function.
The other curves in fig. 7.3 show the resulting coherence functions for $2.5 \cdot 6\,\mathrm{m} = 15\,\mathrm{m}$ and

$5 \cdot 6\,\mathrm{m} = 30\,\mathrm{m}$ distance, which are also in reasonable agreement with the measured curves shown in figure 2.3 b and c.

The wave character of the microseismic motion and the 2.5 Hz resonance is introduced by modifying equation (7.14) for frequencies around 0.14 Hz and 2.5 Hz as

$$\begin{aligned}\phi_k(\omega) &= \phi_{k-1}(\omega) + \Delta\phi_k(\omega) + \\ &+ \left(\frac{2\delta\omega_m\omega}{\sqrt{(\omega_m^2-\omega^2)^2+(2\delta\omega_m\omega)^2}}\right)^4 \cdot \frac{2\pi L}{\lambda_m} + \\ &+ \left(\frac{2\delta\omega_c\omega}{\sqrt{(\omega_c^2-\omega^2)^2+(2\delta\omega_c\omega)^2}}\right)^4 \cdot \frac{2\pi L}{\lambda_c}, \end{aligned} \tag{7.20}$$

with λ_m being the wavelength of the microseismic peak and λ_c of the 2.5 Hz resonance of the upper earth's crust, respectively.

As can be seen from eqn. (7.13), this constant additional phase advance does not change the coherence $|\gamma|$.

Since the time dependent ground motion signals generated by this model are based on Fourier transformations they are naturally periodic. Therefore uncorrelated drifts as described by the ATL rule are not included in this algorithm.

Both the filter-based model and the FFT-based algorithm can be adapted to any measured ground motion data (power spectrum and coherence). Therefore beam dynamics in a linear collider under the influence of ground motion can be studied and compared for different sites.

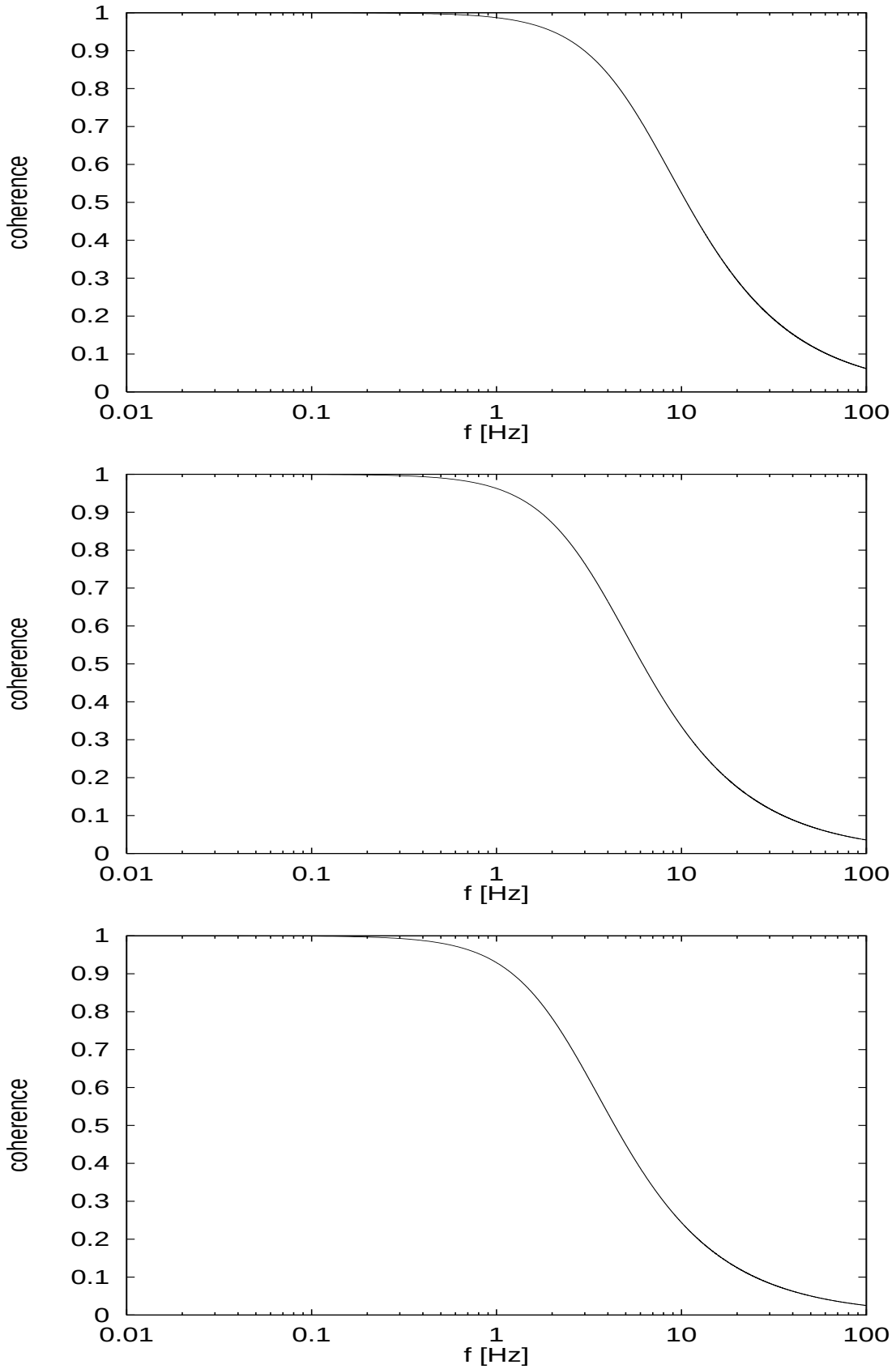

Figure 7.2: Coherence functions $|\gamma|$ for three different distances $L = 5\,\mathrm{m}$, $L = 15\,\mathrm{m}$ and $L = 30\,\mathrm{m}$, calculated according to equation (7.7), with $A = 4 \cdot 10^{-6}\ \frac{\mu\mathrm{m}^2}{\mathrm{m \cdot sec}}$ and $B = 3 \cdot 10^{-2}\ \mu\mathrm{m}^2 \cdot \mathrm{Hz}^3$.

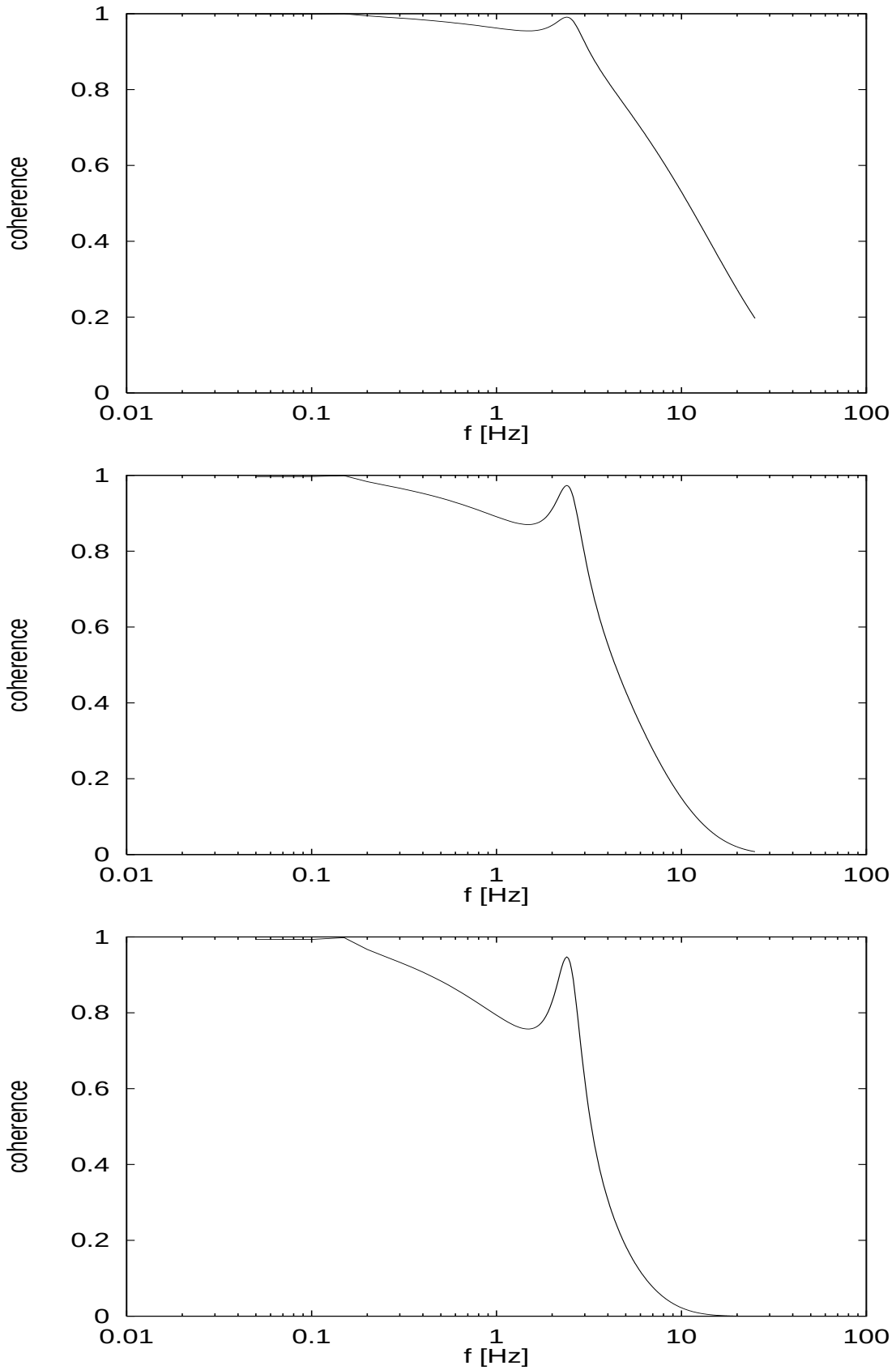

Figure 7.3: Coherence $|\gamma|$ for two points at distances of $L = 5\,\mathrm{m}$, $L = 15\mathrm{m}$ and $L = 30\,\mathrm{m}$ according to eqns. (7.15) and (7.16).

8 Beam dynamics under the influence of ground motion

8.1 The lattice

The lattice of the S-band Linear Collider SBLC main linac is composed of FODO cells with constant phase advance $\mu = 90°$ and a scaling of the β-function proportional to the square root of the energy, $\beta \propto \sqrt{E}$.
Since the accelerating sections between the quadrupoles consist of identical units of $l = 6\,\mathrm{m}$ length each, the scaling of the β-function has to be chosen as a stepwise function of the energy, approximating the $\sqrt{E}$ behaviour as [Cou 58]

$$\hat{\beta} = 2L\frac{1+\sin(\mu/2)}{\sin(\mu)}, \tag{8.1}$$

$$\check{\beta} = 2L\frac{1-\sin(\mu/2)}{\sin(\mu)}, \tag{8.2}$$

with $L = n \cdot l$.
Therefore, the SBLC main linac is divided into eight sections with constant β-function FODO lattice in each section. While the first section contains only one 6 m accelerating section between each two quadrupoles, the 8th one consists of eight of them between each two magnets. The resulting lattice is summarized in table 8.1, showing the number of FODO cells and accelerating structures as well as the energy gain ΔE per section and the total energy E at the end of each section under the assumption of a loaded gradient of 17.3 MeV/m and an injection energy of 3.15 GeV. The average of the β-function in the focusing and defocusing quadrupole is denoted by $\overline{\beta}$. Here, a filling factor of 90 % is assumed, leading to a cell length of 13.3 m in the first linac section.
For the investigation of ground motion effects, a thin lens FODO lattice with ideal telescopic systems matching the β-functions between each two sections has been used. Figure 8.1 shows the scaling of the β-function in this lattice.

section	# of FODO cells	# of accel. structures per FODO cell	per section	$\overline{\beta}$/m	ΔE/GeV	E/GeV
1	48	$\times 2 =$	96	13.3	9.8	13.1
2	36	$\times 4 =$	144	26.6	15.0	28.1
3	36	$\times 6 =$	216	40.0	22.4	50.5
4	32	$\times 8 =$	256	53.5	26.6	77.1
5	32	$\times 10 =$	320	66.6	33.2	110.3
6	32	$\times 12 =$	384	80.0	39.9	150.2
7	32	$\times 14 =$	448	93.3	46.5	196.7
8	32	$\times 16 =$	512	106.6	53.2	250.0
$\sum$	280		2376			

Table 8.1: FODO lattice for the SBLC main linac, consisting of eight sections with a β-function scaling approximating $\beta \propto \sqrt{E}$.

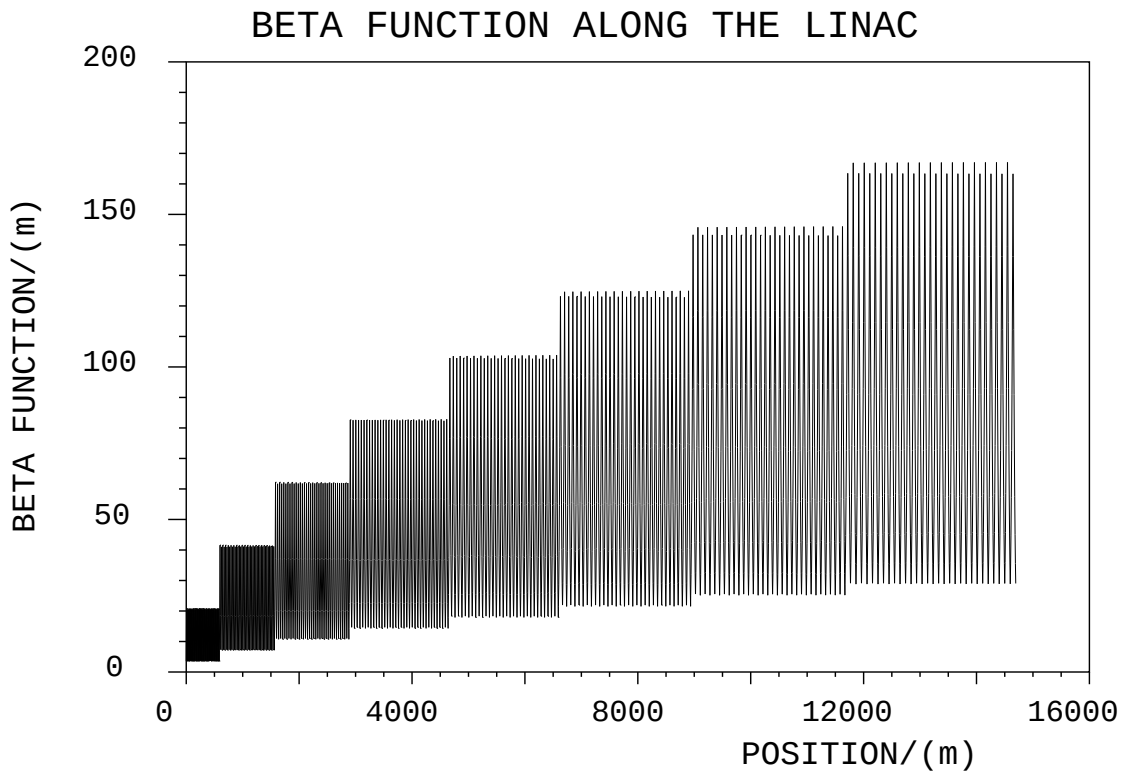

Figure 8.1: β-function scaling chosen for the SBLC main linac.

8.2 Simulation results

One of the main goals of the simulation of beam dynamics under the influence of ground motion is to prove that the active stabilization system is capable of reducing the rms beam jitter sufficiently in spite of the enhancement of quadrupole motion within certain frequency bands around 0.8 Hz and beyond 30 Hz, as presented in Section 5.
Therefore, beam motion was simulated using both the filter-based and the FFT-based ground motion algorithm.
At the end of the linac, a beam based correction system has been assumed which corrects the position of each bunch train by subtracting the value measured at the previous one, corresponding to the transfer function

$$H(s) = 1 - \exp(-sT_0). \tag{8.3}$$

Here, s denotes the Laplace variable, while $T_0 = 0.02\,\mathrm{sec} = 50^{-1}\,\mathrm{Hz}^{-1}$ is the time between consecutive bunch trains. Figure 8.2 shows the modulus $|H(s)|$ of this transfer function using $s = i\omega = i \cdot 2\pi f$.
As this plot shows, this algorithm suppresses beam motion at frequencies below 8.3 Hz, while beam jitter in the frequency band 8.3 Hz to 41.7 Hz is even amplified. This unavoidable effect can be easily understood as follows:
Assuming a sinusoidal vertical beam motion with amplitude A and frequency ω,

$$y_{\mathrm{beam}}(t) = A \cdot \sin(\omega t), \tag{8.4}$$

the time T_{beam} between consecutive bunch trains corresponds to a phase shift ϕ between the position measured at the ith bunch and the position of the $(i+1)$th bunch of

$$\phi = \frac{\omega}{\omega_{\mathrm{beam}}} = \frac{\omega}{\frac{2\pi}{T_{\mathrm{beam}}}} \tag{8.5}$$

This results in a remaining beam motion

$$\begin{aligned} \delta y_{\mathrm{beam}} &= A \cdot \sin(\omega t) - A \cdot \sin(\omega t - \phi) \\ &= 2 \cdot A \cdot \sin\frac{\phi}{2} \cos\left(\omega t - \frac{\phi}{2}\right). \end{aligned} \tag{8.6}$$

Therefore a phase shift ϕ with $|\phi| > 60°$ corresponding to the frequency band between $f_{\mathrm{rep}}/6$ and $5f_{\mathrm{rep}}/6$ leads to enhanced beam jitter.
The same result can also be obtained from equation (8.3), with

$$\begin{aligned} |H(s)| &= |1 - \exp(-sT_0)| \\ &= |1 - [\cos(-\omega T_0) + i\sin(-\omega T_0)]| \\ &= \sqrt{[1-\cos(-\omega T_0)]^2 + \sin^2(-\omega T_0)} \\ &= \sqrt{2 - 2\cos(-\omega T_0)} \\ &= \sqrt{2 - 2\cos(\omega T_0)}. \end{aligned} \tag{8.7}$$

Resolving $|H(s_0)| = 1$ for $s_0 = i\omega_0$ yields

$$\omega_0 = 2\pi f_0 = \frac{1}{T_0} \arccos\left(\frac{1}{2}\right) \tag{8.8}$$

and therefore, with $T_0 = 1/f_{\mathrm{rep}}$,

$$f_0 = \frac{1}{2\pi T_0}\frac{\pi}{3} = \frac{f_{\mathrm{rep}}}{6}. \tag{8.9}$$

Since a beam position monitor is also influenced by ground motion, the beam position is measured with respect to the center of the last quadrupole of the main linac. Thus the beam position monitor as well as the correction kicker are assumed to be fixed to this magnet. In an accelerator, however, the correction signal is provided by a kicker changing the angle of the beam trajectory with respect to the design orbit. Therefore the location of this corrector has to be chosen at a betatron phase advance of $\pi/2$ with respect to the location of the monitor.
As a first step the lattice response function to ground motion waves at the characteristic frequency, $f_c = 2.5\,\mathrm{Hz}$, of the ground surface (see Section 2) is investigated assuming plane monochromatic sinusoidal waves with wavelengths λ_c between 1 and 1000 m, corresponding to phase velocities v of 2.5 to 2500 m/s.
This assumption is somewhat unrealistic since any dissipative effect is neglected and the motion of each pair of magnets is perfectly correlated. Since all distances between quadrupoles in the SBLC lattice are multiples of the accelerating structure length of $l = 6\,\mathrm{m}$, even short wavelengths λ_c with $m \cdot \lambda_c = n \cdot 6\,\mathrm{m}$, with n and m being integer numbers, lead to very small beam jitter amplitudes since neighbouring magnets in several sections of the linac move at the same phase. In terms of the wave number, $k_c = 2\pi/\lambda_c$, this is a spatial equivalent of the Shannon

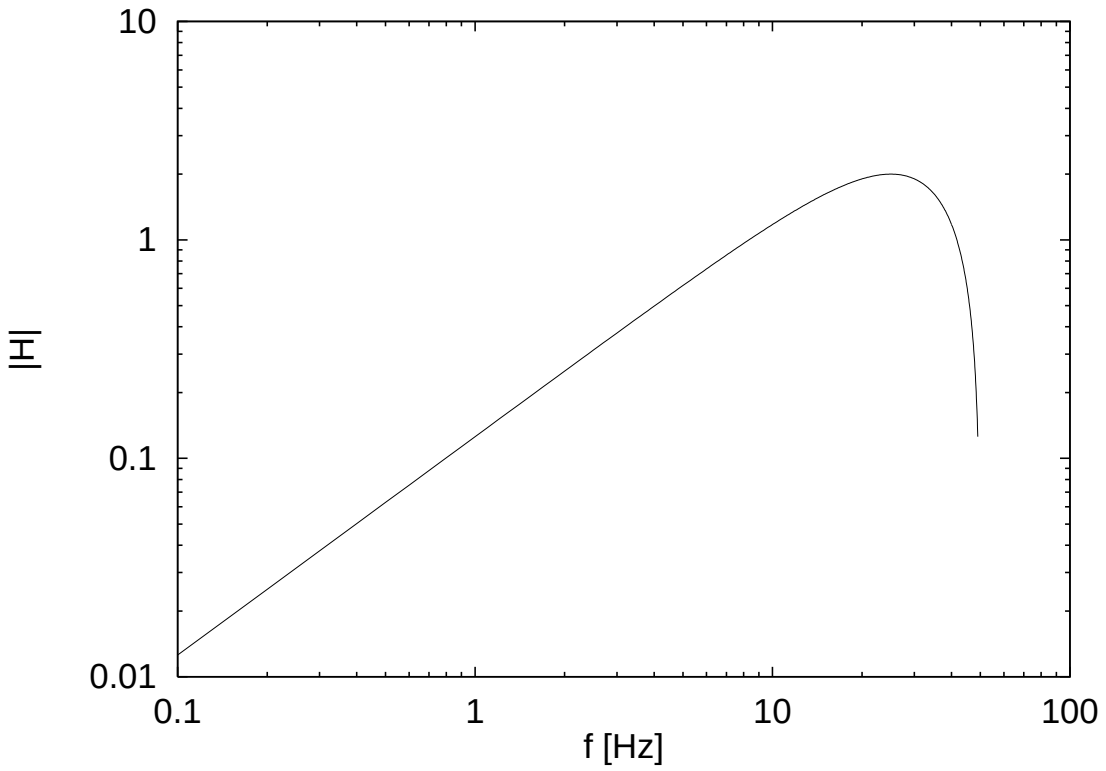

Figure 8.2: Transfer function $|H|$ of the beam based correction system applied at the end of the main linac.

theorem stating that at a given sampling frequency, ω_0, only frequencies with $\omega < \omega_0/2$ can be correctly detected (see Appendix A). In the case of waves travelling along the linac this means that only wavelengths $\lambda_c > 2\Delta L$, with ΔL being the distance between two neighbouring quadrupoles, need to be considered. Shorter wavelengths are undersampled resulting in increased effective wavelengths.
Since this is a well-known phenomenon in the theory of digital sampling of analog signals, the lattice response function is investigated as function of the wave number k_c instead of the wavelength λ_c. The result is shown in figure 8.3, which presents the ratio of beam jitter amplitude and ground wave amplitude, with the beam jitter amplitude being the rms value of the beam jitter remaining after application of the beam based correction algorithm (eqn. (8.3)) at the end of the linac. The corresponding values without this correction algorithm are larger by a factor $|H(s = i \cdot 2\pi \cdot 2.5\,\mathrm{Hz})|^{-1} = 3.2$.

As this plot shows, sinusoidal waves travelling along the linac lead to resonant behaviour of beam motion at the end of the accelerator for several wavelengths that are multiples of the distance between neighbouring quadrupoles. With increasing wavelength λ (or decreasing wave number k), this amplification of magnet jitter is significantly reduced, indicating that the beam trajectory begins to follow the distorted magnet position. Since the distances between neighbouring quadrupoles are larger at the end of the linac than at the beginning, these latter magnets do not contribute significantly to the resulting beam jitter whenever the ground motion wavelength exceeds their distance. The least significant resonance peak occurs around $k = 0.0164$, which corresponds to the largest betatron wavelength of 384 m in the lattice.

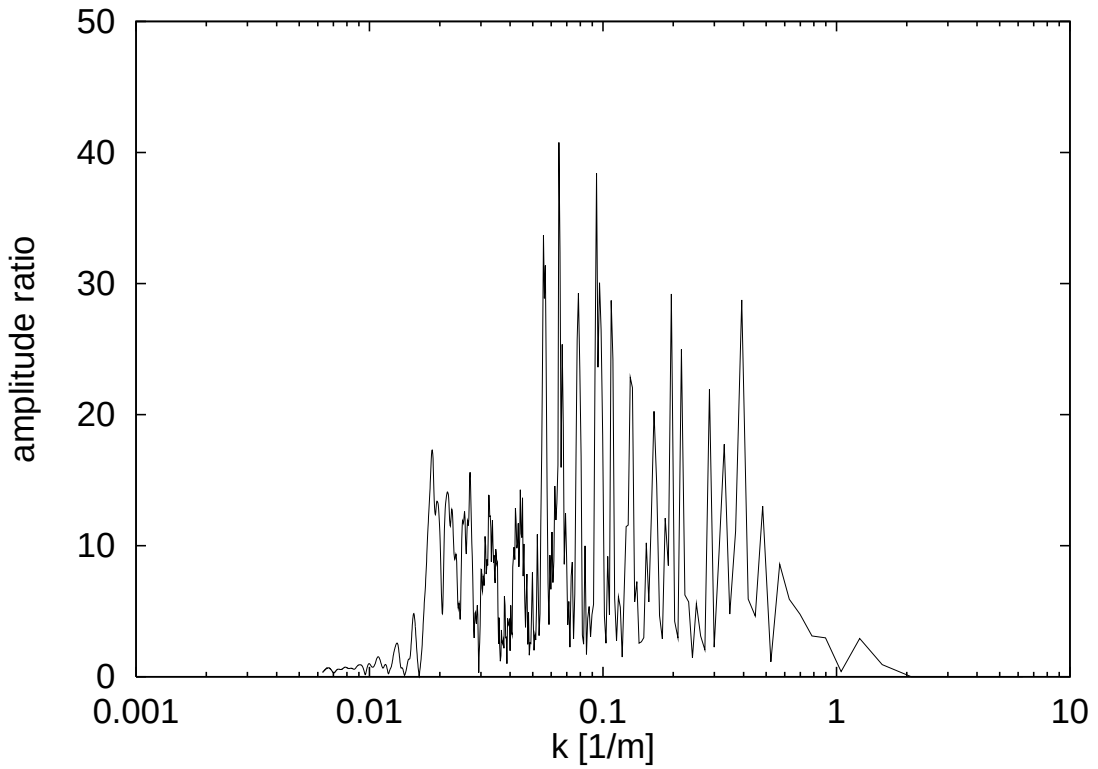

Figure 8.3: Lattice response function representing the ratio of beam jitter amplitudes after application of beam based feedback to the amplitude of the 2.5 Hz ground motion wave with wave number k travelling along the linac. Here only wavelengths being integer multiples of 1 m have been considered. For very short wavelengths the lattice response function is somehow periodic due to the undersampling effect. Therefore investigation of the response function for wavelengths below the minimum distance between quadrupoles in the lattice would not lead to additional information.

With the active stabilization system switched on, the resulting beam jitter is reduced by a factor of 3.4 in addition to the factor 3.2 resulting from the beam based correction.
In a further step, ground motion is modelled using the FFT-based algorithm with ground motion spectrum according to eqn. (2.42) and coherence according to eqn. (7.16). The wavelength is set to zero for all frequency components except 2.5 Hz. At this specific frequency the wavelength λ_c is again varied from 1 m to 1000 m. In this case the resonant behaviour of the machine optics nearly vanishes. This effect can be understood from figure 8.3, which shows very sharp resonance peaks. Since the additional random phase advance (see eqns. (7.13) and (7.20)) corresponds to a change in the wavelength λ_c between each two quadrupoles, the resonance condition is hardly fulfilled.
When the wavelengths are chosen according to eqn. (7.20) with λ_c being varied from 1 m to 1000 m in order to investigate its influence under more realistic conditions, the resonance behaviour of the lattice vanishes. Figure 8.4 shows the resulting rms beam jitter amplitudes with and without active stabilization as a function of the wave number k of the 2.5 Hz resonance.

The mean damping factor $\sigma_{y,\mathrm{ground}}/\sigma_{y,\mathrm{stab}}$ averaged over all wave numbers is 2.8. Compared to the beam size at the end of the linac, being 9.1 μm, the calculated rms beam jitter of

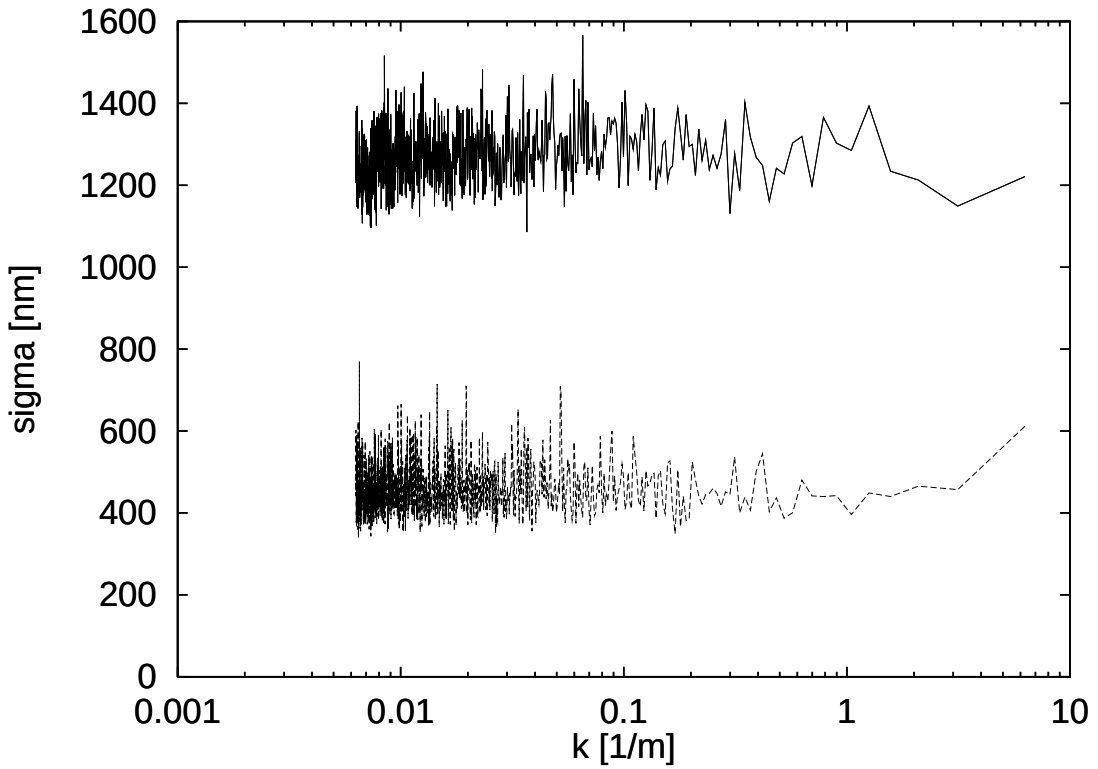

Figure 8.4: Remaining vertical rms beam jitter σ_y with the beam based feedback systsem switched on as function of the wave number of the upper earth's 2.5 Hz resonance. The solid upper curve shows the rms value without active stabilization, while the dashed lower line represents the rms beam jitter with the active stabilization system switched on. The average damping factor is 2.8.

$\sigma_y \approx 1.3\,\mu$m without active stabilization corresponds to a luminosity $\mathcal{L}$ as (see eqn. (1.13))

$$\mathcal{L} = \mathcal{L}_0 \cdot \exp\left(-2\frac{\sigma_y^2}{4\sigma_{\text{beam}}^2}\right) = 0.990 \cdot \mathcal{L}_0. \tag{8.10}$$

Here, $\mathcal{L}_0$ denotes the design luminosity with the two beams colliding head-on.
The corresponding value with active stabilization can be calculated using $\sigma_y = 0.45\,\mu$m as $\mathcal{L} = 0.999 \cdot \mathcal{L}_0$. Since the luminosity degradation even without active stabilization is only about 1 %, active stabilization of quadrupole jitter might not be necessary in the main linac of the 500 GeV machine (SBLC). On the other hand, a similar system can be used in the final focus system of this machine with its tighter tolerances.
Using equation (1.12) with $\sigma_q = 70$ nm, which is the measured rms value for frequencies higher than 2 Hz (see fig. 1.2), we get a rms beam jitter amplitude of 2.3 μm. As a comparison with the simulation result shows, it is appropriate to assume ground motion to be completely uncorrelated to obtain a rough estimate of its effect.
For a complete description, the phase space area occupied by a δ-function like beam under the influence of ground motion,

$$\epsilon = \gamma y^2 + 2\alpha y y' + \beta y'^2, \tag{8.11}$$

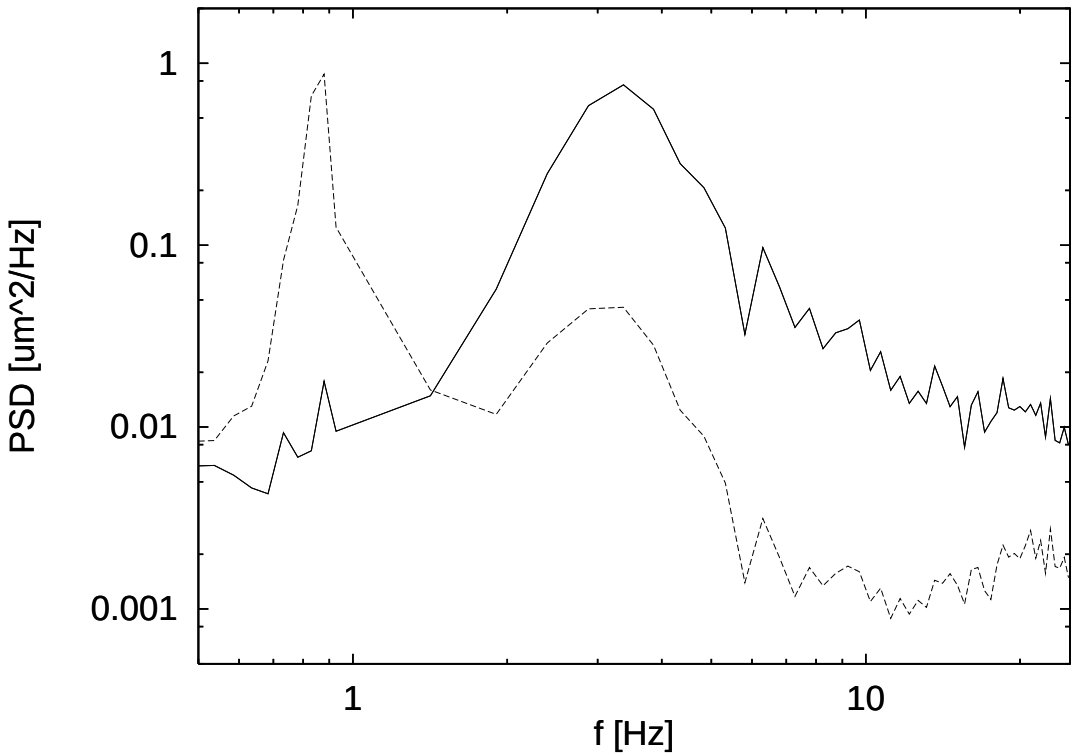

Figure 8.5: Power spectrum (PSD) of beam based stabilized beam motion with (dashed) and without active stabilization (solid line). The wavelength of the 2.5 Hz resonance was set to 200 m.

has to be considered. Here, α and γ are the Twiss parameters which can be calculated from the β-function and its derivative.
With active stabilization of quadrupole vibrations this emittance is $2.8 \cdot 10^{-15}$ m, while without active stabilization it is about a factor of 7 larger, namely $2.0 \cdot 10^{-14}$ m. Compared to the design vertical beam emittance at the end of the linac, $\epsilon_{\mathrm{end}} = 5 \cdot 10^{-13}$ m, the orbit emittance is about 4 % without and approximately 0.56 % with active stabilization, respectively.
The corresponding power spectra (or power spectrum densities, PSD) of beam motion after application of the beam based correction algorithm (eqn. (8.3)) are shown in figure 8.5. While both spectra vanish at very low frequencies due to beam based orbit correction, the damping effect of the active stabilization system is clearly visible for frequencies beyond approximately 1.5 Hz. Between 0.5 and 1.5 Hz beam jitter amplitudes are enhanced when the active stabilization system is working. As a comparison with figure 6.3 shows, this effect is caused by the enhanced quadrupole vibration amplitudes around 0.8 Hz. As already mentioned in Section 5, this effect occurs since the active stabilization system has to be operated close to its stability limit, which is determined by the sensor. To avoid this effect, broad-band seismometers may be considered in the active stabilization system, but these are usually more expensive.
Furthermore, the effect of ATL-like drifts was investigated using the filter-based model. While the parameter B was fixed at $B = 3 \cdot 10^{-2}\ \mu\mathrm{m}^2 \cdot \mathrm{Hz}^3$, A was varied from 10^{-8} to $6.7 \cdot 10^{-1}\ \mu\mathrm{m}^2/(\mathrm{m} \cdot \mathrm{sec})$. Varying A effectively changes the characteristic frequency where the coherence drops, i. e. the cutoff frequency of the highpass and lowpass filters. The resulting rms beam jitter am-

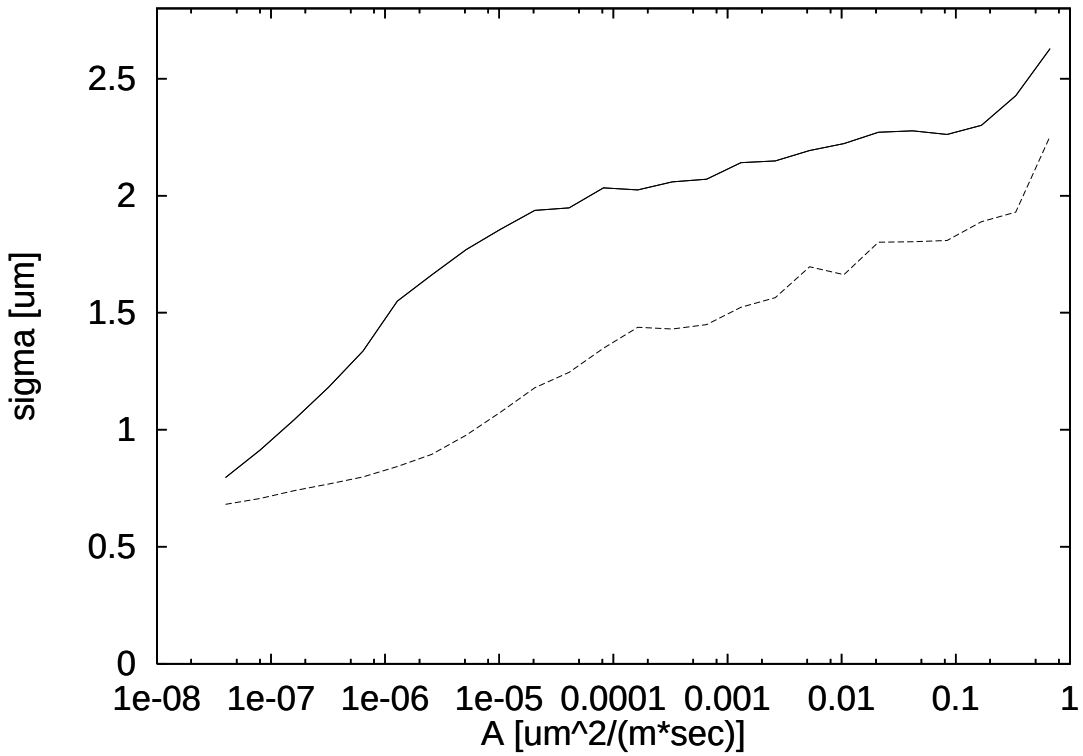

Figure 8.6: Resulting rms beam jitter as a function of the proportionality factor A in the ATL rule, with the beam based feedback system switched on. The parameter B of the spectrum was fixed at $3 \cdot 10^{-2}\,\mu\mathrm{m}^2 \cdot \mathrm{Hz}^3$. The solid line represents the rms jitter amplitude resulting from pure ground motion, while the dashed line shows the corresponding value with active stabilization.

plitudes after application of the beam-based feedback are shown in figure 8.6. As expected the resulting beam jitter amplitude increases with increasing A due to reduced coherence. Furthermore, the effect of active stabilization vanishes for very small A. This can be understood since vanishing A implies perfect correlation, so the whole accelerator moves as a whole, solid body. Very small values of A correspond to large cutoff frequencies ω_0, i. e. uncorrelated quadrupole motion dominates only for very high frequencies. Since the active stabilization system leads to an enhancement of magnet jitter amplitudes beyond 35 Hz, this uncorrelated motion is amplified, while the damping at lower frequencies, where magnet motion is well correlated, has only little effect on the beam motion. Therefore, active stabilization of mechanical quadrupole vibrations is useless in an environment where A is very small.
Compared to the results obtained using the FFT-based model, the effect of active stabilization of mechanical quadrupole vibrations is significantly smaller. Figure 8.7 shows the power spectra of remaining beam motion after application of the beam-based correction system for the model parameters set to $A = 4 \cdot 10^{-6}\,\mu\mathrm{m}^2/(\mathrm{m} \cdot \mathrm{sec})$ and $B = 3 \cdot 10^{-2}\,\mu\mathrm{m}^2 \cdot \mathrm{Hz}^3$.
As a comparison with figure 8.5 shows, the power spectrum density (PSD) of beam motion without active stabilization is significantly larger for frequencies beyond approximately 5 Hz than in the case of the FFT-based model, while around 3 Hz both spectra are quite similar. Between 1.5 and 2 Hz, beam motion amplitudes are slightly higher than those obtained using the FFT-based model. These enhanced amplitudes lead to increased rms beam jitter without

active stabilization of quadrupole motion.
With the active stabilization system switched on, beam motion amplitudes obtained using the filter-based ground motion model are enhanced with respect to those simulated with the FFT-based model in the same frequency bands as without active stabilization, but the effect of active stabilization is smaller there.
Since ground motion spectra used in both ground motion simulation algorithms are practically the same, this must be an effect of the different coherence (see figs. 7.3 and 7.2).
With the rms values of beam jitter for these parameters being $0.9\,\mu$m and $1.7\,\mu$m with and without active stabilization (see fig. 8.6), the corresponding luminosity degradation according to equation (1.13) is 0.5 % and 1.7 %, respectively.

The beam orbit emittance ϵ at the end of the SBLC main linac has been investigated for

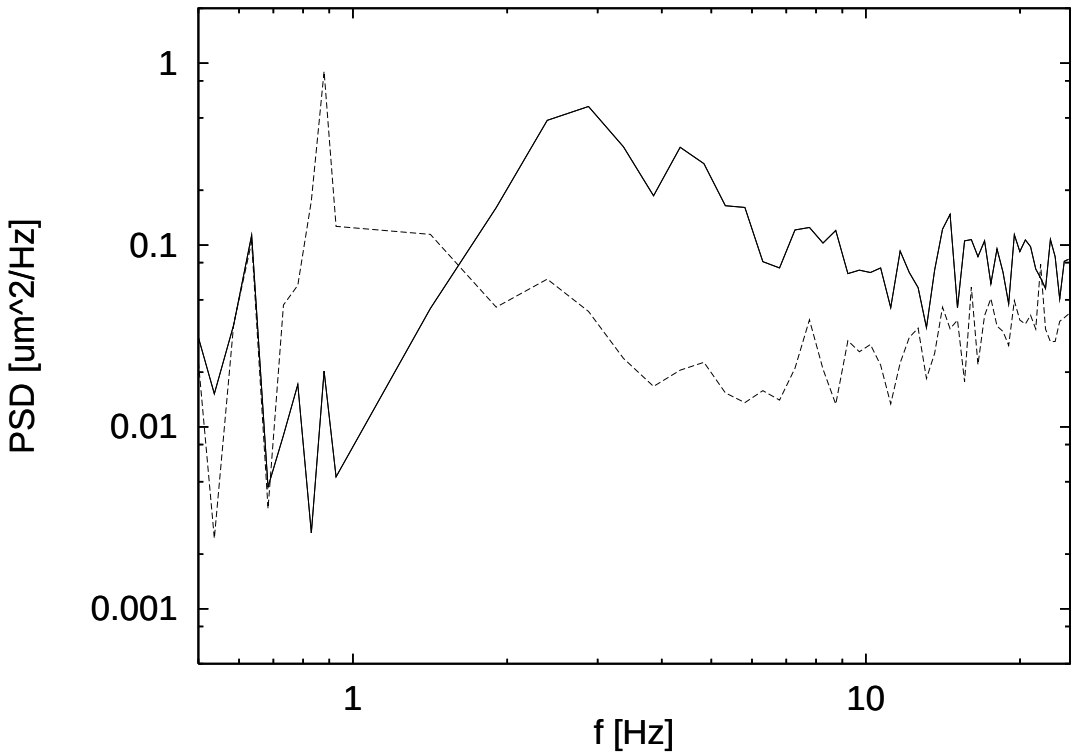

Figure 8.7: Power spectrum (PSD) of beam motion (with beam-based feedback) with (dashed) and without active stabilization (solid line), simulated using the filter-based ground motion model. The parameters were set to $A = 4 \cdot 10^{-6}\,\mu\text{m}^2/(\text{m} \cdot \text{sec})$ and $B = 3 \cdot 10^{-2}\,\mu\text{m}^2 \cdot \text{Hz}^3$. The corresponding rms beam jitter is $0.9\,\mu$m with and $1.7\,\mu$m without active stabilization, respectively.

the filter-based model (see fig. 8.8). The orbit emittance that remains after application of the beam-based feedback grows from approximately $\epsilon = 8 \cdot 10^{-15}$ m for $A = 4 \cdot 10^{-8}\,\mu\text{m}/(\text{m} \cdot \text{sec})$ to about $6.5 \cdot 10^{-14}$ m for $A = 6.7 \cdot 10^{-1}\,\mu\text{m}/(\text{m} \cdot \text{sec})$ when the active stabilization system is switched off. These values correspond to 1.6 % and 13 % of the nominal vertical beam emittance $\epsilon_{\text{end}} = 5 \cdot 10^{-13}$ m, respectively.
With active stabilization of quadrupole vibrations, the vertical orbit emittance due to ground

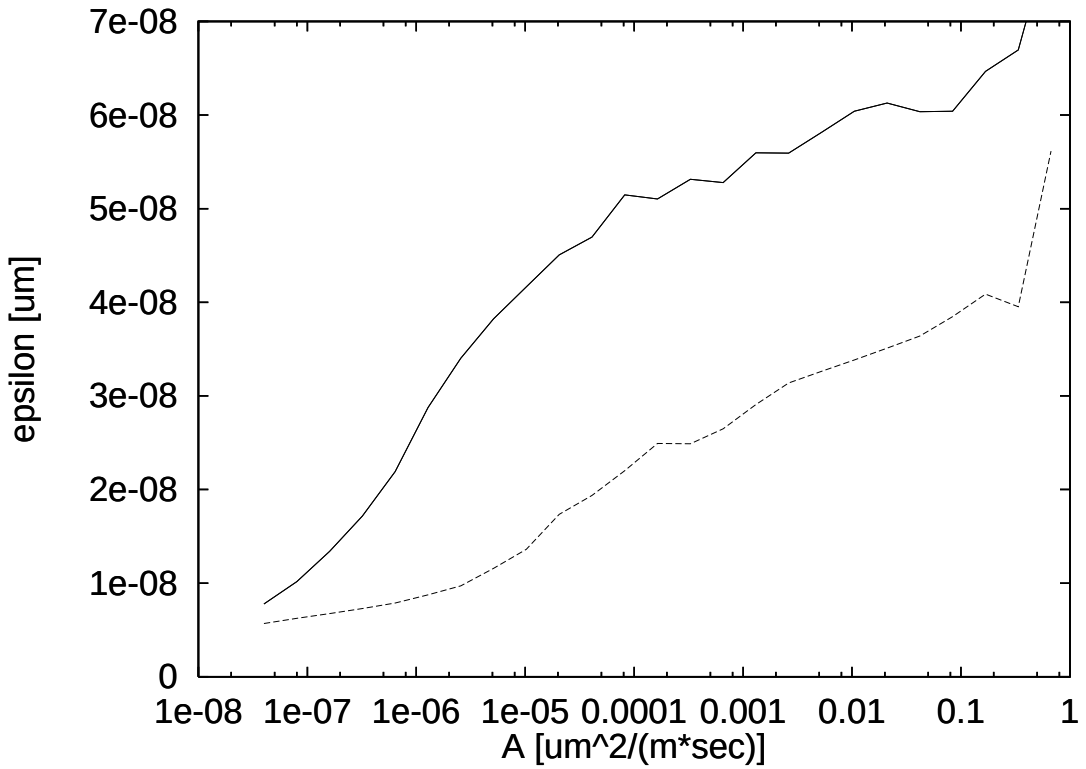

Figure 8.8: Beam orbit emittance $\epsilon = \gamma y^2 + 2\alpha y y' + \beta y'^2$ of vertical beam motion at the end of the main linac as a function of the ATL constant A, with (dashed) and without active stabilization of quadrupole vibrations (solid line).

motion is significantly smaller. In this case, it increases from about $6 \cdot 10^{-15}$ m for $A = 4 \cdot 10^{-8}\,\mu$m/(m $\cdot$ sec) to approximately $4.4 \cdot 10^{-14}$ m for $A = 6.7 \cdot 10^{-1}\,\mu$m/(m $\cdot$ sec), corresponding to 1.2 % and 8.8 % of the beam emittance ϵ_{end}, respectively.
The measured coherence spectra correspond to $A = 4 \cdot 10^{-6}\,\mu$m/m $\cdot$ sec (see Sections 2 and 7). The obtained orbit emittances in this case are $1.0 \cdot 10^{-14}$ m with and $3.5 \cdot 10^{-14}$ m without active stabilization of quadrupoles. These values correspond to about 2 % and 7 % of the vertical beam emittance ϵ_{end}, respectively. As a comparison with the corresponding values obtained by the FFT-based model shows, the orbit emittance calculated using the filter-based algorithm is about a factor of 2 larger than the result from the FFT-based algorithm when the active stabilization system is switched off. With active stabilization, it is decreased by a factor of 3.5 in the case of the filter-based model, while in the case of the FFT-based algorithm a factor of about 7 is achieved (see above).

9 Conclusion

In this thesis ground motion measurements at DESY have been presented. The influence of noise on the measured coherence has been investigated in detail. As has been demonstrated, any observed lack of coherence seems to be a real property of the ground, because the required additional noise level due to electric noise on the cables, air pressure variations or temperature fluctuations is judged to be too high.
The observed ground motion amplitudes are potentially harmful for linear colliders because of luminosity reduction due to beam jitter. Therefore an inexpensive active stabilization system for quadrupoles has been developed and tested. It has been experimentally demonstrated that active stabilization of mechanical quadrupole vibrations is possible down to 25 nm for vibration frequencies higher than 2 Hz even in quite noisy environments with ground motion amplitudes of 100 nm in the same frequency range. In less noisy places, an rms value of less than 10 nm is likely to be achieved due to the very low noise level of the motion sensors. Therefore the system presented in this paper may even be applicable in the final focus system of the S-band Linear Collider SBLC, provided that the final focus is located in a less noisy environment.
Since X-band machines like JLC and NLC require much tighter quadrupole jitter tolerances than the SBLC, this system will also be of interest for them.
At the present time a complete active stabilization system costs approximately DM 15000 per unit. This is expected to reduce significantly for a large number of systems.
If due to the choice of an extremely quiet environment the required tolerances will be achieved even without active stabilization, a retrofit of the machine with the system described in this thesis can be considered as a luminosity upgrade option.
Compared to any correction scheme based on dipole correctors to compensate magnet motion detected by a geophone, a mechanical system has two advantages. Firstly, inexpensive sensors with a large range in their phase shift can be used in the active stabilization system presented in this paper, while a system based on dipole correctors requires a phase shift close to 0°. Therefore more sophisticated motion sensors have to be used, usually being more expensive.
Secondly, the performance of the presented system can be monitored online by taking data from the geophones on top of each quadrupole, independent of beam observation and linac operation.
To investigate the effects of ground motion on the beam orbits in a linear collider, two complementary simulation models have been developed. Both models can be modified to simulate any ground motion data. Using the ground motion and coherence spectra measured at DESY, the expected beam jitter in the S-band Linear Collider SBLC has been studied. It has been demonstrated that the active stabilization system is capable of reducing beam motion at the end of the SBLC main linac significantly by a factor of up to 2.8. Thus, the luminosity degradation due to beam jitter can be kept below 1 %.

Acknowledgements

I would like to thank J. Rossbach for continuous support and encouragement and innumerable discussions. He provided many interesting ideas and has always been a great source of motivation.
I am also indebted to P. Schmüser for being second examiner.
Furthermore, I would like to thank R. Brinkmann, N. Holtkamp and G. A. Voss for many stimulating discussions.
Special thanks to V. Shiltsev for numerous introductory conversations concerning ground motion measurements. I would like to thank A. Sery for his explanations concerning analytical treatment of ground motion, and C. Guralp for his introduction to the technology of modern seismometers.
Particular gratitude is due to G. Weichert, G. Meyer and H. Kaiser for the excellent mechanical design of the quadrupole support.
The pleasant atmosphere provided by R. Assmann, D. Burke, R. Siemann, C. Salsberg and D. Plouffe during my visit to SLAC is deeply acknowledged.
I would like to thank several colleagues for helpful discussions, in particular I. Reyzl, R. D. Kohaupt and K. H. Mess.
Special thanks to Ch. Kloppenburg for his assistance concerning the Young's modulus of concrete.
I am indebted to J. Maidment, M. Lomperski and T. Limberg for careful reading of the manuscript.

A The Shannon theorem

Sampling a continuous signal x(t) with spectrum

$$S_c(f) = \frac{1}{\sqrt{2\pi}} \int_{-\infty}^{\infty} x(t) \exp(-i \cdot 2\pi f t)\, \mathrm{d}t \tag{A.1}$$

at equidistant intervals T leads to a sampled signal $x(nT)$ with the corresponding spectrum

$$S_s(f) = \sum_{n=-\infty}^{\infty} x(nT) \exp(-i \cdot 2\pi n T f). \tag{A.2}$$

Inserting the inverse Fourier transform

$$x(t) = \frac{1}{\sqrt{2\pi}} \int_{-\infty}^{\infty} S_c(f) \exp(i \cdot 2\pi t f)\, \mathrm{d}f \tag{A.3}$$

for $t = nT$ into eqn. (A.2) yields

$$\begin{aligned}
S_s(f) &= \sum_{n=-\infty}^{\infty} \left(\frac{1}{\sqrt{2\pi}} \int_{-\infty}^{\infty} S_c(\nu) \exp(i \cdot 2\pi n T \nu)\, \mathrm{d}\nu \right) \exp(-i \cdot 2\pi n T f) \\
&= \frac{1}{\sqrt{2\pi}} \int_{-\infty}^{\infty} S_c(\nu) \sum_{n=-\infty}^{\infty} \exp[-i \cdot 2\pi n T (f - \nu)]\, \mathrm{d}\nu \\
&= \frac{1}{\sqrt{2\pi}} \int_{-\infty}^{\infty} S_c(f - \mu) \sum_{n=-\infty}^{\infty} \exp[-i \cdot 2\pi n T \mu]\, \mathrm{d}\mu \\
&= \frac{1}{\sqrt{2\pi}} \int_{-\infty}^{\infty} S_c(f - \mu) \frac{1}{T} \sum_{n=-\infty}^{\infty} \delta\left(\mu - n \cdot \frac{1}{T}\right) \mathrm{d}\mu \\
&= \frac{1}{T} \sum_{n=-\infty}^{\infty} S_c\left(f - n \cdot \frac{1}{T}\right).
\end{aligned} \tag{A.4}$$

The term $S_c(f - n/T)$ corresponds to a shift of the spectrum $S_c(f)$ along the frequency axis, leading to a periodic spectrum.
In the case of a spectrum $S_c(f)$ of the continuous signal $x(t)$ being limited to the interval $[-f_g, f_g]$, the spectra $S_s(f)$ of the sampled signal will be overlapping when shifted as long as the sampling frequency $1/T$ is lower than twice the cutoff frequency f_g of the continuous spectrum. This effect leads to a distortion of the spectrum, called aliasing.
In other words, the sampling frequency $1/T$ has to be chosen at least twice as high as the highest frequency of the continuous signal,

$$\frac{1}{T} > 2 \cdot f_g. \tag{A.5}$$

This fact is well known as the Shannon theorem [Jer 77].

B Description of linear systems in the frequency domain

This section gives a short introduction to the description of linear, time-invariant systems in the frequency domain. The Laplace transformation describing systems in continuous time is as well introduced as the $\mathcal{Z}$ transformation used for the description of time discrete devices like digital filters and feedback circuits.

B.1 The Laplace transformation

A general linear system is described by its differential equation

$$\sum_{k=0}^{K} a_k(t) y^{(k)}(t) = \sum_{l=0}^{L} b_l(t) u^{(l)}(t), \tag{B.1}$$

with $u(t)$ and $y(t)$ being its input and output signal, respectively. Here, $y^{(k)}(t)$ denotes the kth time derivative of the input signal $y(t)$. In the time-invariant case this can be written as

$$\sum_{k=0}^{K} a_k y^{(k)}(t) = \sum_{l=0}^{L} b_l u^{(l)}(t). \tag{B.2}$$

Using the Laplace transformation

$$\mathcal{L}\{f(t)\} = \int_0^\infty e^{-st} f(t) dt =: F(s) \tag{B.3}$$

with the complex frequency $s = \sigma + i\omega$, and assuming the initial conditions to be zero, i. e. $y(0+) = \ldots = y^{(K)}(0+) = u(0+) = \ldots = u^{(L)}(0+) = 0$, equation (B.2) can be rewritten as

$$\sum_{k=0}^{K} a_k s^k Y(s) = \sum_{l=0}^{L} b_l s^l U(s) \tag{B.4}$$

$$\Leftrightarrow Y(s) \sum_{k=0}^{K} a_k s^k = U(s) \sum_{l=0}^{L} b_l s^l. \tag{B.5}$$

Division by $\sum a_k s^k$ yields:

$$\begin{aligned} Y(s) &= \frac{\sum_{l=0}^{L} b_l s^l}{\sum_{k=0}^{K} a_k s^k} U(s) \\ &=: G(s) U(s) \end{aligned} \tag{B.6}$$

with the transfer function $G(s)$ of the system. Some important properties of the Laplace transformation should be mentioned:

- The time derivation $\frac{d}{dt}$ corresponds to a multiplication by the complex factor s, while the integration $\int \ldots dt$ corresponds to a division by s. The first relation has already been used in equations (B.2) and (B.4).
- For $\sigma = 0$, the Laplace transform $F(s)$ of a function $f(t)$ with $f(t) \equiv 0$ for $t < 0$ is equivalent to its Fourier transform $F(\omega)$.

- The transfer function $G(s)$ of two systems with transfer functions $G_1(s)$ and $G_2(s)$ connected in series is $G(s) = G_1(s) \cdot G_2(s)$, while in the case of two devices connected in parallel it becomes the sum $G(s) = G_1(s) + G_2(s)$.
- A dead time T_d corresponds to a factor e^{-sT_d} in the Laplace transform.
- $\mathcal{L}\{\frac{t^{n-1}}{(n-1)!}e^{\alpha t}\} = \frac{1}{(s-\alpha)^n}$
- $\mathcal{L}\{a \cdot f(t) + b \cdot g(t)\} = a \cdot \mathcal{L}\{f(t)\} + b \cdot \mathcal{L}\{g(t)\}$ (linearity)

B.2 The $\mathcal{Z}$ transformation

For the description of a function $f(t)$ sampled at equidistant times $n \cdot T$ using the Laplace transformation we define

$$f_0(t) = f_n = f(n \cdot T) \quad \text{for} \quad n \cdot T \leq t < (n+1) \cdot T, \qquad n = 0, 1, \ldots \tag{B.7}$$

Since $f_0(t)$ is constant in each of these intervals, the Laplace transform can be calculated as

$$\begin{aligned} \mathcal{L}\{f_0(t)\} &= \sum_{n=0}^{\infty} \int_{n \cdot T}^{(n+1) \cdot T} e^{-st} f_n \, \mathrm{d}t \\ &= \sum_{n=0}^{\infty} f_n \frac{e^{-snT} - e^{-s(n+1)T}}{s} \\ &= \frac{1 - e^{-sT}}{s} \sum_{n=0}^{\infty} f_n e^{-snT} \\ &=: \frac{1 - e^{-sT}}{s} \mathcal{D}\{f_n\}. \end{aligned} \tag{B.8}$$

To get rid of the common factor $(1 - e^{-sT})/s$, we define $\mathcal{D}\{f_n\}$ as the discrete $\mathcal{L}$ transformation [Zyp 56].
This $\mathcal{D}$ transform can be interpreted as the Laplace transform of a distribution

$$\begin{aligned} f(t) \sum_{n=0}^{\infty} \delta(t - nT) &= \sum_{n=0}^{\infty} f(nT) \delta(t - nT) \\ &= f^*(t), \end{aligned} \tag{B.9}$$

where

$$\begin{aligned} \mathcal{L}\left\{ \sum_{n=0}^{\infty} f(nT) \delta(t - nT) \right\} &= \sum_{n=0}^{\infty} f(nT) \mathcal{L}\{\delta(t - nT)\} \\ &= \sum_{n=0}^{\infty} f(nT) e^{-snT} \\ &= \mathcal{D}\{f(nT)\}. \end{aligned} \tag{B.10}$$

Therefore,

$$\mathcal{D}\{f(nT)\} = \mathcal{L}\{f^*(t)\}. \tag{B.11}$$

For simplicity reasons, the factor e^{sT} is denoted as

$$e^{sT} = z, \tag{B.12}$$

leading to the $\mathcal{Z}$ transformation

$$\begin{aligned} \mathcal{Z}\{f_n\} &= \sum_{n=0}^{\infty} f_n z^{-n} \\ &= F(z). \end{aligned} \tag{B.13}$$

Application of the $\mathcal{Z}$ transformation to a linear difference equation with constant coefficients,

$$y(n) = \sum_{k=1}^{N} a_k y(n-k) + \sum_{l=0}^{M} b_l u(n-l), \tag{B.14}$$

leads to

$$\mathcal{Z}\{y(n)\} = \mathcal{Z}\left\{\sum_{k=1}^{N} a_k y(n-k)\right\} + \mathcal{Z}\left\{\sum_{l=0}^{M} b_l u(n-l)\right\} \tag{B.15}$$

and therefore, using the linearity of the $\mathcal{Z}$ transformation,

$$Y(z) = Y(z) \cdot \sum_{k=1}^{N} a_k z^{-k} + U(z) \cdot \sum_{l=0}^{M} b_l z^{-l}. \tag{B.16}$$

Thus,

$$Y(z) = \frac{\sum\limits_{l=0}^{M} b_l z^{-l}}{1 - \sum\limits_{k=1}^{N} a_k z^{-k}} \cdot U(z), \tag{B.17}$$

with

$$H(z) = \frac{\sum\limits_{l=0}^{M} b_l z^{-l}}{1 - \sum\limits_{k=1}^{N} a_k z^{-k}} \tag{B.18}$$

being the $\mathcal{Z}$ transfer function of the system described by eqn. (B.14).

C Feedback systems

The aim of a feedback system is to force the output $y(t)$ of a physical system to follow a certain nominal output function. For this purpose, the output signal $y(t)$ has to be compared to the control input signal $u(t)$, as shown schematically in figure C.1. As long as the difference or error signal $e(t) = u(t) - y(t)$ is not identically zero, the feedback system will react in order to suppress this deviation. Therefore the effect of noise signals will be minimized.

According to fig. C.1, the transfer function $H_g(s)$ describing the transfer of the noise signal

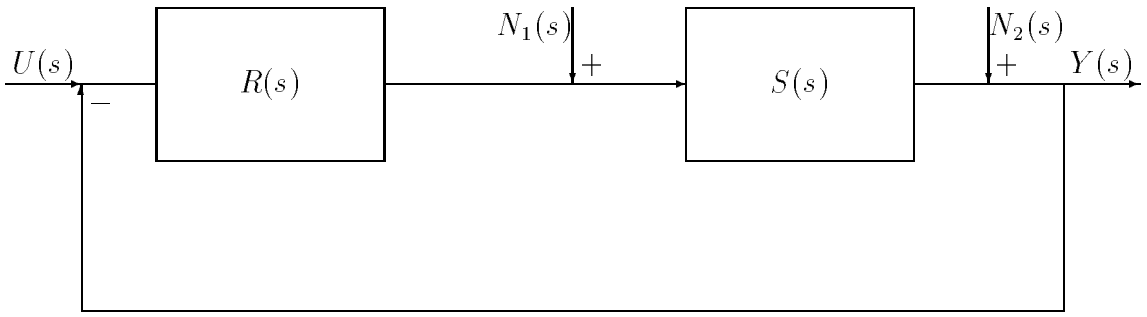

Figure C.1: Block diagram of a basic control system.

$N_1(s)$ through the closed linear feedback loop to the output $Y(s)$ can be derived as ($U(s) = N_2(s) = 0$)

$$Y(s) = S(s) \cdot N_1(s) - R(s)S(s) \cdot Y(s) \tag{C.1}$$

$$\Leftrightarrow \quad Y(s) = \frac{S(s)}{1 + R(s) \cdot S(s)} \cdot N_1(s) = H_g(s) \cdot N_1(s). \tag{C.2}$$

Here $N_1(s)$, $U(s)$ and $Y(s)$ are the Laplace transform of the noise signal $n_1(t)$, the input signal $u(t)$ and the output signal $y(t)$, respectively. $S(s)$ is the transfer function of the system under control, while $R(s)$ denotes the transfer function of the controller (or regulator).
Additionally, the transfer function $H_m(s)$ for a disturbance signal $N_2(s)$ added to the output $X(s)$ of the system to be controlled is computed as ($U(s) = N_1(s) = 0$)

$$Y(s) = N_2(s) - R(s)S(s) \cdot Y(s) \tag{C.3}$$

$$\Leftrightarrow \quad Y(s) = \frac{1}{1 + R(s) \cdot S(s)} \cdot N_2(s) = H_m(s) \cdot N_2(s). \tag{C.4}$$

Here, $N_2(s)$ is the Laplace transform of the noise signal $n_2(t)$.
In the case of the active stabilization system presented in Section 5, the noise signal $N_1(s)$ represents ground motion acting on the magnet through the support, while $N_2(S)$ disturbs the magnet directly, like air flow in the tunnel. Since the aim of this active stabilization system is to keep the magnet position at rest, the control input $U(s)$ is identically zero.

D Stability of feedback loops

One of the most important properties not only of control systems but of all time invariant components, for example digital filters, is stability. The most common definition of stability is the so-called BIBO stability (bounded input - bounded output), which means that the system's response to any bounded input signal never reaches infinity.
A graphical stability criterion can be derived as follows (see fig. D.1):
Breaking the closed loop of the system at an arbitrary location and feeding in a signal $x(t)$ with

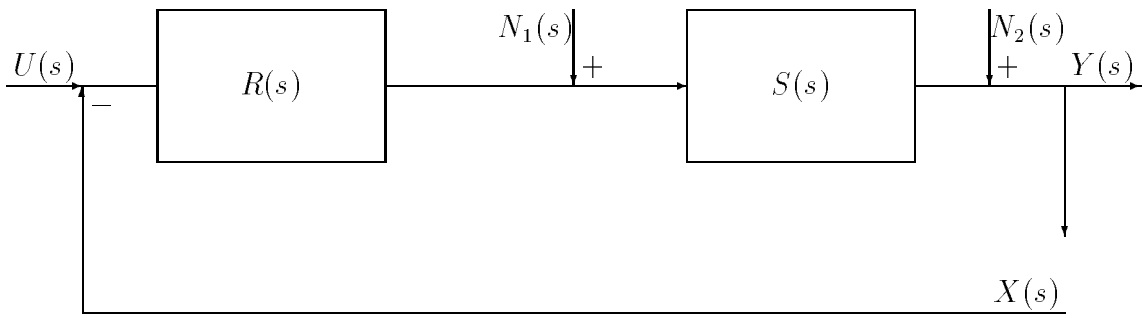

Figure D.1: Interrupted feedback loop. A signal $x(t)$ with corresponding Laplace transform $X(s)$ is fed in.

corresponding Laplace transform $X(s)$ leads to the output signal ($U(s) = N_1(s) = N_2(s) = 0$)

$$\begin{aligned} Y(s) &= -R(s) \cdot S(s) \cdot X(s) \\ &= F(s) \cdot X(s) \end{aligned} \tag{D.1}$$

at the break point.
For $-F(s_c) = -F(i\omega_c) = -a = a \cdot \exp[i \cdot (2k+1) \cdot \pi]$ at some frequency ω_c, this leads to

$$Y(s_c) = a \cdot X(s_c). \tag{D.2}$$

Therefore the output signal $Y(s_c)$ equals the input signal $X(s_c)$ times some (real) gain factor a. Only in the case $a < 1$ does the amplitude of this oscillation decrease after closing the system loop; otherwise it increases ($a > 1$) or remains unchanged ($a = 1$). Therefore the gain of the feedback system has to be less than one at those frequencies ω_c where the phase shift reaches an odd multiple of π.
To derive an algebraic stability criterion, the response of the system with the transfer function $G(s)$ to an unity step function $u(t) = \sigma(t)$ as input has to be calculated. With

$$U(s) = \mathcal{L}\{u(t)\} = \frac{1}{s}, \tag{D.3}$$

one gets the Laplace transform $Y(s)$ of the output signal $y(t)$:

$$\begin{aligned} Y(s) &= G(s) \cdot U(s) \\ &= G(s) \cdot \frac{1}{s}. \end{aligned} \tag{D.4}$$

Using the partial fraction form of $Y(s)$, the output function $y(t)$ in the time domain can be determined.
In the case of only single poles of $G(s)$ (and therefore of $Y(s)$), one gets:

$$Y(s) = \frac{c_0}{s} + \sum_{\nu=1}^{n} \frac{c_\nu}{s - \alpha_\nu}, \tag{D.5}$$

which, using the inverse Laplace transformation, leads to

$$y(t) = c_0 + \sum_{\nu=1}^{n} c_\nu \exp(\alpha_\nu t). \tag{D.6}$$

A pole $\alpha \neq 0$ of the order q leads to the sum of partial fractions

$$\frac{c_1}{s-\alpha} + \frac{c_2}{(s-\alpha)^2} + \cdots + \frac{c_q}{(s-\alpha)^q},\ c_q \neq 0, \tag{D.7}$$

which corresponds to the time-dependent function

$$c_1 \exp(\alpha t) + c_2 \frac{t}{1!} \exp(\alpha t) + \cdots + c_q \frac{t^{q-1}}{(q-1)!} \exp(\alpha t) = p(t) \exp(\alpha t), \tag{D.8}$$

with p(t) being a polynomial of $(q-1)$th order.
If $\alpha = 0$ is a pole of qth order of the transfer function $G(s)$, it leads to a pole of $(q+1)$th order of $Y(s)$ due to the factor $1/s$ introduced by the input step function. Its partial fraction sum

$$\frac{c_0}{s} + \cdots + \frac{c_q}{s^{q+1}},\ c_q \neq 0, \tag{D.9}$$

corresponds to the time dependent function

$$c_0 + c_1 \cdot \frac{t}{1!} + \cdots + c_q \cdot \frac{t^q}{q!}, \tag{D.10}$$

which is a polynomial of order q.
To summarize, the response function $y(t)$ of the system to an unity step function input can be written as

$$y(t) = p_0(t) + \sum_{\lambda=1}^{l} p_\lambda(t) \exp(\alpha_\lambda t). \tag{D.11}$$

In this equation, $\alpha_\lambda \neq 0$ are the different poles of $G(s)$, each of the order q_λ, and $p_\lambda(t)$ are polynomials of the order $q_\lambda - 1$.
If $s = 0$ is a pole of $G(s)$ of order q_0, $p_0(t)$ is a polynomial of order q_0, otherwise it is a constant.
From equation (D.11) an algebraic stability criterion can be derived. Each pole α of $G(s)$ corresponds to a finite number of terms

$$r t^k \exp(\alpha t),\ k = 0, 1, 2, \ldots \tag{D.12}$$

with r being constant and $\alpha = \delta + i\omega$.
The modulus of each term,

$$\left| r t^k \exp(\alpha t) \right| = |r|\, t^k \exp(\delta t), \tag{D.13}$$

is limited for large times t if and only if

$$\Re(\alpha) = \delta < 0. \tag{D.14}$$

This is the algebraic stability criterion for continuous time.
As

$$z = \exp(sT), \tag{D.15}$$

the corresponding criterion for time discrete systems becomes

$$|z_{s,i}| < 1,\ i = 1, \ldots, n, \tag{D.16}$$

where $z_{s,i}$ are the poles of the time discrete transfer function.
Since, for many applications, the influence of the regulator algorithm on the poles of the closed loop transfer function is not easy to investigate due to high order of the system, the graphical stability criterion is often more convenient. The algebraic stability criterion is more appropriate in the design of digital filters.

E Digital filters

Generally speaking, any digital system processing some input signal in order to get a certain output is called a digital filter. Typical examples of digital filters are lowpass, highpass and bandpass filters which can be derived from the corresponding analog filters, but additionally there is a large number of systems which can be realized only by digital systems. Commonly, the (analog) input signal is digitized at equidistant times $n \cdot T$, where T denotes the sampling time. Therefore these filters can be described by the $\mathcal{Z}$ transformation.
To derive the filter algorithm from the transfer function $H(s)$ of the corresponding analog filter, we calculate the transfer function $H(z)$ of a digital integrator. According to the trapezium rule, i. e. a linear interpolation between the kth and the $(k-1)$th time step, we get

$$\begin{aligned} y(k) &= y(k-1) + T \cdot \frac{x(k) + x(k-1)}{2} && \text{(E.1)} \\ \Leftrightarrow \quad (1 - z^{-1}) \cdot Y(z) &= \frac{T}{2} \cdot (1 + z^{-1}) \cdot X(z) && \text{(E.2)} \\ \Leftrightarrow \quad Y(z) &= \frac{T}{2} \cdot \frac{1 + z^{-1}}{1 - z^{-1}} \cdot X(z) && \text{(E.3)} \\ &= H(z) \cdot X(z). && \text{(E.4)} \end{aligned}$$

Comparing this result to the transfer function of an analog integrator,

$$H(s) = \frac{1}{s}, \tag{E.5}$$

we get the bilinear transformation

$$s = i\omega_a \approx \frac{2}{T} \frac{z-1}{z+1}. \tag{E.6}$$

with

$$z = e^{i\omega_d T}. \tag{E.7}$$

Here, ω_a is the frequency variable of the analog system, while ω_d corresponds to the digital filter.
As eqn. (E.6) indicates, these two different frequencies are connected via

$$\omega_a = \frac{2}{T} \tan \frac{\omega_d T}{2}, \tag{E.8}$$

leading to a periodicity of the $\mathcal{Z}$ transfer function with $\omega_d T = n\pi$.
The same result can also be obtained resolving $z = \exp(sT)$ for s and truncating the power expansion of the logarithm,

$$\begin{aligned} s &= \frac{1}{T} \ln(z) \\ &= \frac{2}{T} \left[\frac{z-1}{z+1} + \frac{(z-1)^3}{3(z+1)^3} + \cdots \right]. && \text{(E.9)} \end{aligned}$$

Therefore the transfer function of the digital filter can be calculated from that of the corresponding analog filter by substituting s according to the bilinear transformation (eqn. (E.6)).

This bilinear transformation projects the left half of the complex s plane where $\Re(s) < 0$ into the unit circle with $|z| < 1$; hence the stability is conserved (see Appendix D).
In the second step, the $\mathcal{Z}$ transfer function $H(z)$ has to be rewritten as a difference equation, which gives the filter equation directly.
Both the analog-to-digital conversion of the input signal and the corresponding inverse procedure at the output of the digital system cause special problems due to quantization effects. This means a representation of the analog, continuous input signal by a limited number of bits, resulting in limited accuracy of the digital representation. This effect corresponds to a round-off or truncation to a certain number of digits. Similar results of computation are truncated or rounded to fit into the given number format of the microprocessor. With x being either the analog signal amplitude or the exact result of a certain calculation and x_q denoting the digitized representation or the truncated or rounded result, respectively, this can be written as

$$x = x_q + \epsilon. \tag{E.10}$$

Here ϵ is the error occuring due to rounding or truncation.
As shown in figure E.1, the maximum error q, with q being the value represented by the least significant bit, of the truncation process is twice as large as that of the rounding process. Therefore, and since the error due to truncation can be described as a constant plus round-off error, only the effect of rounding will be analyzed. For the analysis of quantization effects, different methods have been developed. Here, we will concentrate on the stochastic analysis method [Wid 56].
Assuming $x(n)$ as a random variable taking successive sampled values of the input function x, the error sequence $\epsilon(n)$ will be equally distributed over its range of possible values, being the interval $[-q/2, q/2]$.
Therefore for the mean value μ and the variance σ^2 of ϵ we get

$$\mu = 0, \tag{E.11}$$

$$\sigma^2 = \frac{q^2}{12}. \tag{E.12}$$

Thus, a white noise model for $\epsilon(n)$ can be assumed as

$$\epsilon(n) = w(n) \tag{E.13}$$

with autocorrelation function

$$R_w(n) = \langle w(k)w(k+n)\rangle = \begin{cases} \frac{q^2}{12} & ,(n=0) \\ 0 & ,(n \neq 0) \end{cases} \tag{E.14}$$

and mean value $\mu = 0$.
The variance of the output y of a digital filter with transfer function $H(z)$ due to this noise can be computed as [Wid 56]

$$\sigma_y^2 = \frac{1}{2\pi i} \oint_{\partial D} H(z)H(z^{-1})\frac{q^2}{12}\frac{\mathrm{d}z}{z}, \tag{E.15}$$

with the integral being calculated on the unit circle.
Application of this formalism to an integrator,

$$y(n) = y(n-1) + T_0 \cdot x(n), \tag{E.16}$$

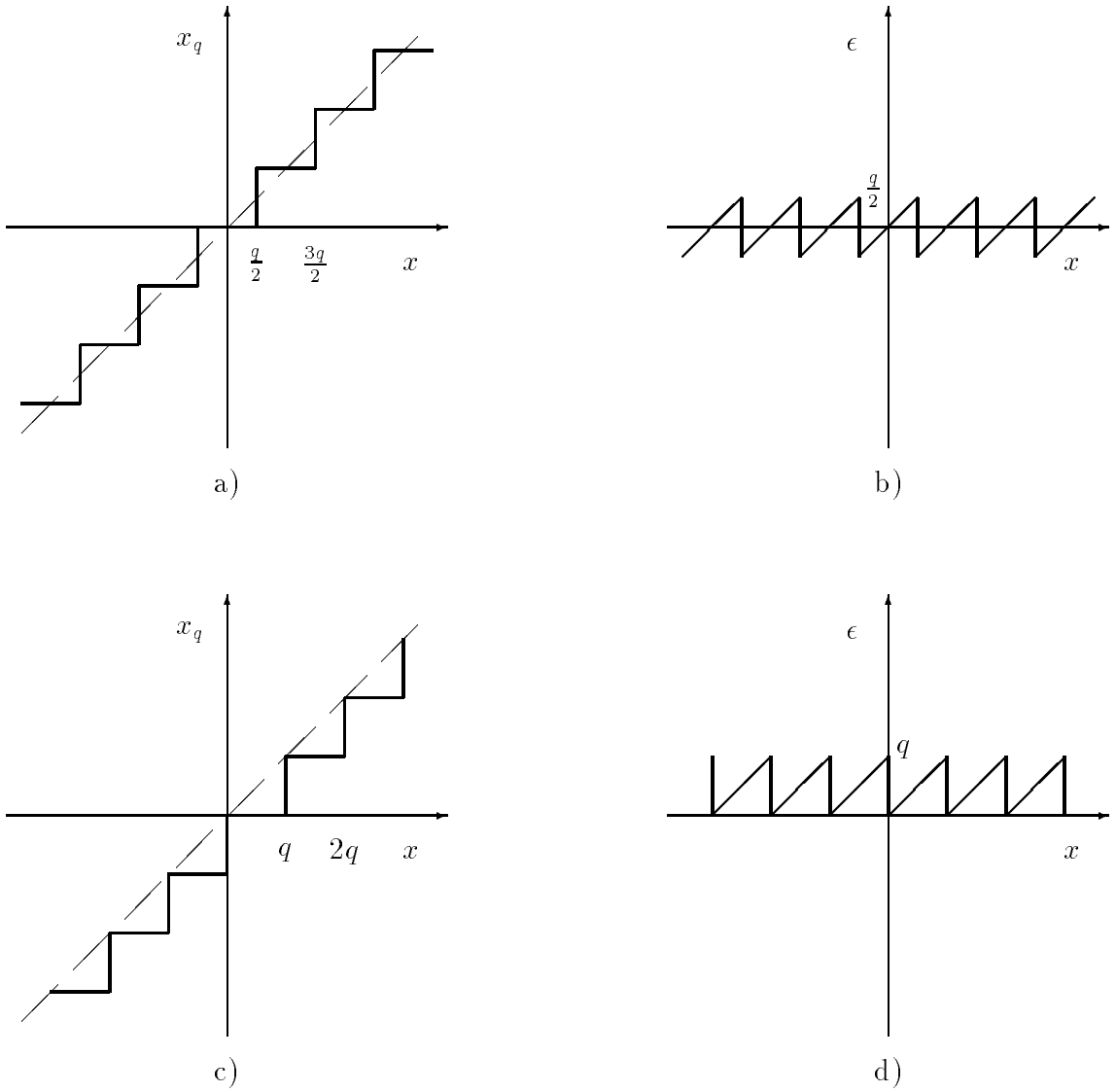

Figure E.1: Plotted effect of limited accuracy of digital systems due to quantization by analog-to-digital conversion and numerical calculations. a) Plot of rounded value x_q versus exact value x. b) Error ϵ due to round off versus exact value x. c) Plot of truncated value x_q versus exact value x. d) Error ϵ due to truncation versus exact value x.

with corresponding transfer function

$$H(z) = \frac{T_0}{1 - z^{-1}} \tag{E.17}$$

and sampling time T_0 leads to an rms value of the output signal being

$$\sigma_y^2 = \frac{T_0^2}{2\pi i} \oint_{\partial D} \frac{1}{(1 - z^{-1})(1 - z)} \frac{q^2}{12} \frac{\mathrm{d}z}{z}, \tag{E.18}$$

which is infinite.
Therefore the integration algorithm has to be modified as

$$y(n) = \frac{1}{\alpha} \cdot y(n-1) + T_0 \cdot x(n) \tag{E.19}$$

with $\alpha > 1$, resulting in the transfer function

$$\begin{aligned} H(z) &= \frac{T_0}{1 - \frac{1}{\alpha} z^{-1}} && \text{(E.20)} \\ &= \frac{\alpha T_0}{\alpha - z^{-1}}. && \text{(E.21)} \end{aligned}$$

Hence,

$$\begin{aligned} \sigma_y^2 &= \alpha^2 T_0^2 \frac{q^2}{12} \frac{1}{2\pi i} \oint\limits_{\partial D} \frac{1}{(\alpha - z^{-1})(\alpha - z)} \frac{\mathrm{d}z}{z} \\ &= -\frac{\alpha^2 T_0^2}{\alpha} \frac{q^2}{12} \frac{1}{2\pi i} \oint\limits_{\partial D} \underbrace{\frac{1}{(z - 1/\alpha)(z - \alpha)}}_{f(z)} \mathrm{d}z \\ &= -\frac{\alpha^2 T_0^2}{\alpha} \frac{q^2}{12} \mathrm{res}_{1/\alpha} f \\ &= \alpha^2 T_0^2 \frac{q^2}{12} \frac{1}{\alpha^2 - 1}, \end{aligned} \tag{E.22}$$

which is finite. Here, ∂D denotes the unit circle.
A second source of errors closely related to that described previously is the finite accuracy of filter coefficients, sometimes leading to instability due to rounding errors.
Assuming for example the realization of an analog first order highpass filter with cutoff frequency f_0 and transfer function

$$H(s) = \frac{s}{\omega_0 + s}, \quad \omega_0 = 2\pi f_0 \tag{E.23}$$

by a digital filter with sampling frequency f, we get the $\mathcal{Z}$ transfer function

$$H(z) = a \cdot \frac{1 - z^{-1}}{1 + b z^{-1}} \tag{E.24}$$

with

$$\begin{aligned} a &= \frac{1}{1 + \tan(\frac{\omega_0}{2f})} && \text{(E.25)} \\ b &= \frac{\tan \frac{\omega_0}{2f} - 1}{\tan \frac{\omega_0}{2f} + 1}. && \text{(E.26)} \end{aligned}$$

In the case $f \gg f_0$ we get $b \approx -1$, leading to a pole z_0 of the transfer function close to the unit circle representing the stability limit. Therefore, a rounding or truncation of b to $b = -1$ has to be carefully avoided, since this would lead to instability of the system.

F Magnet optics effect of a tilted quadrupole

A particle on the nominal orbit reaching a focussing quadrupole misaligned by Δx parallel to the nominal orbit can be described as a particle on a trajectory parallel to the nominal orbit approaching a perfectly aligned magnet, therefore having the initial phase space coordinate vector

$$X_{\mathrm{i}} = \begin{pmatrix} \Delta x \\ 0 \end{pmatrix}. \tag{F.1}$$

Multiplication with the matrix of a focussing quadrupole of length $2l$ and strength k yields

$$\begin{aligned} X_{\mathrm{f}} &= \begin{pmatrix} \cos(2l\sqrt{k}) & \frac{1}{\sqrt{k}}\sin(2l\sqrt{k}) \\ -\sqrt{k}\sin(2l\sqrt{k}) & \cos(2l\sqrt{k}) \end{pmatrix} \cdot \begin{pmatrix} \Delta x \\ 0 \end{pmatrix} \\ &= \begin{pmatrix} \Delta x \cos(2l\sqrt{k}) \\ -\Delta x\sqrt{k}\sin 2l\sqrt{k} \end{pmatrix} \end{aligned} \tag{F.2}$$

for the phase space vector of the particle after the magnet. Therefore, the trajectory is deflected by

$$\begin{aligned} \Delta x' &= -\Delta x\sqrt{k}\sin(2l\sqrt{k}) \\ &\approx \frac{-\Delta x}{l} \cdot \frac{(2l\sqrt{k})^2}{2} \end{aligned} \tag{F.3}$$

for $2l\sqrt{k} \ll 1$.
Assuming now a quadrupole of length $2l$ with its center on the nominal beam axis but tilted by an angle $\Delta x/l$, the incoming nominal particle can be described by the phase space vector

$$X_{\mathrm{i}} = \begin{pmatrix} \Delta x \\ -\frac{\Delta x}{l} \end{pmatrix}. \tag{F.4}$$

This vector transforms by multiplication with the quadrupole matrix into

$$X_{\mathrm{f}} = \begin{pmatrix} \Delta x \cos(2l\sqrt{k}) - \frac{\Delta x}{l\sqrt{k}}\sin(2l\sqrt{k}) \\ -\Delta x\sqrt{k}\sin(2l\sqrt{k}) - \frac{\Delta x}{l}\cos(2l\sqrt{k}) \end{pmatrix}. \tag{F.5}$$

In this case, the trajectory is deflected by

$$\begin{aligned} \Delta x' &= -\Delta x\sqrt{k}\sin(2l\sqrt{k}) - \frac{\Delta x}{l}(\cos(2l\sqrt{k}) - 1) \\ &\approx \frac{\Delta x}{l} \cdot \frac{(2l\sqrt{k})^4}{24} \end{aligned} \tag{F.6}$$

for $2l\sqrt{k} \ll 1$, i. e. as long as the focal length of the quadrupole is larger than the magnet itself. This shows that the magnet optics effect of a tilted quadrupole can be neglected compared to the distortion induced by a magnet misaligned in parallel to the beam axis by the corresponding amount.
Using the thin lens approximation for the quadrupole, this result is obvious since a particle passing the center of the lens does not experience any deflection.

References

[Ass 96] R. Assmann, C. Montag, C. Salsberg, Beamline Stability Measurements with a Stretched Wire System in the FFTB, Proc. LINAC 96

[Bak 91a] B. A. Baklakov, P. K. Lebedev, V. V. Parkhomchuk, A. A. Sery, A. I. Sleptsov, V. D. Shiltsev, Investigation of Correlation and Power Characteristics of Earth Surface Motion at the UNK Site, Preprint INP 91-15, Novosibirsk, 1991

[Bak 91b] B. A. Baklakov, P. K. Lebedev, V. V. Parkhomchuk, A. A. Sery, A. I. Sleptsov, V. D. Shiltsev, Investigation of Seismic Vibrations and Relative Displacement of Linear Collider VLEPP Elements, Proc. IEEE Part. Acc. Conf., San Francisco, 1991

[Bak 93] B. A. Baklakov, P. K. Lebedev, V. V. Parkhomchuk, A. A. Sery, A. I. Sleptsov, V. D. Shiltsev, Investigation of Seismic Vibrations for Linear Collider VLEPP, Sov. Phys. ZhTF., vol. 63, No. 10, 1993 (in Russian)

[Ber 61] C. Bernadini, U. Bizzarri, G. F. Corrazza, G. Ghigo, R. Querzoli, B. Touschek, A 250 MeV Electron-Positron Storage Ring: The AdA, Proc. of Int. Conf. on High Energy Acc., Brookhaven 1961

[Bri 94] R. Brinkmann, J. Rossbach, Observation of Closed Orbit Drift at HERA Covering 8 Decades of Frequency, Nucl. Instr. Meth. A 350 (1994)

[Car 73] G. C. Carter et al., Estimation of the Magnitude-Squared Coherence Function via Overlapped Fast Fourier Transform Processing, IEEE Trans. Au-21, No. 4, August 1973

[Cou 58] E. D. Courant, H. S. Snyder, Theory of the Alternating-Gradient Synchrotron, Ann. Phys. 3 (1958)

[Dec 90] W. Decking, K. Floettmann, J. Rossbach, Measurements of Slow Closed-Orbit Motion in HERA Electron Ring in Correlation with Ground Motion, DESY-M 90-02 and Proc. EPAC 90

[Fis 85] G. E. Fischer, Ground Motion and its Effects in Accelerator Design, SLAC-PUB 3392, 1985, and AIP Conference Series No. 153, Summer School on High Energy Particle Accelerators, Batavia 1984

[Fis 92] G. E. Fischer, Ground Motion, an Introduction for Accelerator Builders, Proc. CERN Accelerator School on Magnetic Measurement and Alignment, CERN 92-05, Geneva 1992

[Gur 93] CMG-3T operation manual, Guralp Systems Ltd., Aldermaston 1993

[Hau 63] R. A. Haubrich, W. H. Munk, F. E. Snodgrass, Comparative Spectra of Microseisms and Swell, Bulletin of the Seismological Society of America 53, 1963

[Hol 93] N. Holtkamp et al., Status of the S-Band Linear Collider Study, DESY M-93-05

[Huk 86] K. Huke, Correlation between the Movement of the Light Source Building and the Vibration of the Synchrotron Radiation Axis, KEK Preprint 86-48

[Jac 75] J. D. Jackson, Classical Electrodynamics, Wiley, New York, 1975

[Jer 77] A. J. Jerry, The Shannon Sampling Theorem - Its Various Extensions and Application: A Tutorial Review, Proc. IEEE 65 (1977) 1565-1596

[Jen 91] J. A. Jendrejczk, M. S. Wambsganass, Vibration Consideration on the Design of the Advanced Photon Source at Argonne National Laboratory, Proc. Symp. on Optical Science and Engineering, 1991

[Jou 93] V. Jouravlev, A. Sery, A. Sleptsov, W. Coosemans, G. Ramseier, I. Wilson, Investigation of Power and Spatial Correlation Characteristics of Seismic Vibrations in the CERN LEP Tunnel for Linear Collider Studies, CERN-SL 93-53

[Keb 94] Dr. Kebe Scientific Instruments GmbH, Schwingungsmesser SMK-1, manual, Halstenbek 1994

[Kei 81] E. Keil, The Large European e^+e^- Collider Project LEP, Proc. Particle Accelerator Conference, Washington 1981

[Ker 85] W. Kertz, Einführung in die Geophysik, B. I. Hochschultaschenbücher, Mannheim 1985

[Leb 92] V. A. Lebedev, P. K. Lebedev, V. V. Parkhomchuk, V. D. Shiltsev, Transverse Vibrations of Electron Beam and Ground Motion Measurements at VEPP-3 Storage Ring, Preprint INP 92-39, Novosibirsk, 1992

[Min 95] M. G. Minty, C. Adolphsen, L. J. Hendrickson, R. Sass, T. Slaton, M. Woodley, Feedback Performance at the Stanford Linear Collider, SLAC Preprint; see also M. Ross, SLC Linac Vibration Study, Sixth International Workshop on Linear Colliders LC 95, KEK Proceedings 95-5

[Mon 94] C. Montag, M. Lomperski, J. Rossbach, Studies of Measurement and Compensation Techniques of Magnet Motion for Linear Colliders, Proc. EPAC 94

[Mon 95] C. Montag, J. Rossbach, A Mechanical Feedback System for Linear Colliders to Compensate Fast Magnet Motion, Proc. PAC 95

[Nap 94] O. Napoly, CLIC Final Focus System: Upgraded Version with Increased Bandwidth and Error Analysis, CEA/DAPNIA/SEA 94 10

[Oga 92] Y. Ogava et al., Vibration Issues Regarding Linac Beam Characteristics, KEK Preprint 92-104

[Oid 89] K. Oide, Final Focus System for the JLC, KEK Preprint 89-190

[Par 93] V. V. Parkhomchuk, V. D. Shiltsev, H. J. Weaver, Measurements of Ground Motion and SSC Dipole Vibrations, SSCL Report SSCL-624, 1993

[Par 94] V. V. Parkhomchuk, V. D. Shiltsev, G. Stupakov, Part. Accel. 46 (1994) 241

[Pet] F. Peters, paper in preparation

[Pet 93] J. Peterson, USGS Open-File Report 93-322, Albuquerque, 1993

[Rau 91] T. O. Raubenheimer, The Generation and Acceleration of Low Emittance Flat Beams for Future Linear Colliders, SLAC report 387, 1991

[Ric 96] G. Richter, R. Weber, in: Schneider Bautabellen, 12th edition, Werner, 1996

[Ros 88] J. Rossbach, Closed-Orbit Distortions of Periodic FODO Lattices Due to Plane Ground Waves, Particle Accelerators 23 (1988) pp. 121-132

[Ros 93] J. Rossbach, Tolerance on Uncorrelated Motion of Quadrupoles for Linear Colliders, DESY M/VM 93-01

[Sch 86] H. Schopper, The LEP Project, Proc. Conf. on High Energy Accelerators, Novosibirsk 1986

[Sch 90] W. Schwarz, Wire Measurements for the Control of the FFTB Magnets, Proc. Second Int. Workshop on Accelerator Alignment, Hamburg 1990

[Ser 95] A. Sery, O. Napoly, Influence of Ground Motion on the Time Evolution of Beams in Linear Colliders, DAPNIA/SEA 95-04, Saclay 1995, and Phys. Rev. E 53 (1996) 5323-5337

[Shi 92] V. D. Shiltsev, Fractal Ground Motion Model, Proc. ECFA Workshop on Linear Colliders, Garmisch Partenkirchen 1992

[Shi 94] V. D. Shiltsev, Measurement of Ground motion and Magnets Vibration at the APS, Budker INP Preprint 94-45, Novosibirsk, 1994

[Shi 95] V. Shiltsev, B. Baklakov, P. Lebedev, C. Montag, J. Rossbach, Measurements of Ground Vibrations and Orbit Motion at HERA, DESY HERA 95-06

[Ste 75] S. D. Stearns, Digital Signal Analysis, Hayden, 1975

[Ste 79] S. D. Stearns, Applications of the Coherence Function in Comparing Seismometers, preprint, Albuquerque 1979

[Sug 92] R. Sugahara, K. Endo, S. Kuroda, T. Mimashi, Y. Ohsawa, Measurement of Seismic Motion and Displacement of the Floor at the TRISTAN Ring, and the Alignment Issues, KEK Preprint 92-200, 1993

[Tak 93] S. Takeda, A. Akiyama, K. Kudo, N. Nakanishi, N. Yamamoto, Slow Drift and Frequency Spectra on Ground Motion, KEK Preprint 93-61

[Tok 84] V. A. Tokmakov, V. I. Vlasov, "On the Development of the SM3 Seismometer and its Capabilities", in "Seismic probes. Instrumental investigation of seismic oscillations", issue 16, pp.3-7, Moscow, Nauka Publisher, 1984 (in Russian)

[Tra 77] N. A. Trapeznikov, "The SM3 Seismometer", in "Seismic probes. Instrumental investigation of seismic oscillations", issue 11, Moscow, Nauka Publisher, 1977 (in Russian)

[Tur 95a] J. L. Turner and R. Stege, Vibration of Linac Quadrupoles at 59 Hz, SLAC Collider Note 399

[Tur 95b] J. L. Turner, C. Adolphsen, G. B. Bowden, F. J. Decker, S. C. Hartman, S. Matsumoto, G. Mazaheri, D. McCormick, M. Ross, R. Stege, S. Virostek, M. Woodley, Vibration Studies of the Stanford Linear Accelerator, SLAC-PUB-95-6867

[Wid 56] B. Widrow, A Study of Rough Amplitude Quantization by Means of Nyquist Sampling Theory, IRE Trans. on Circuit Theory, CT-3, 4, 1956

[Zyp 56] J. S. Zypkin, Differenzengleichungen der Impuls- und Regeltechnik, Verlag Technik, Berlin 1956